Studying venus using polarimetry

With application to exoplanet characterization

Mahapatra, G.

DOI
10.4233/uuid:407591fe-6856-4c29-a320-204d2881e3fa

Publication date
2025

Document Version
Final published version

Citation (APA)
Mahapatra, G. (2025). *Studying venus using polarimetry: With application to exoplanet characterization*. [Dissertation (TU Delft), Delft University of Technology]. https://doi.org/10.4233/uuid:407591fe-6856-4c29-a320-204d2881e3fa

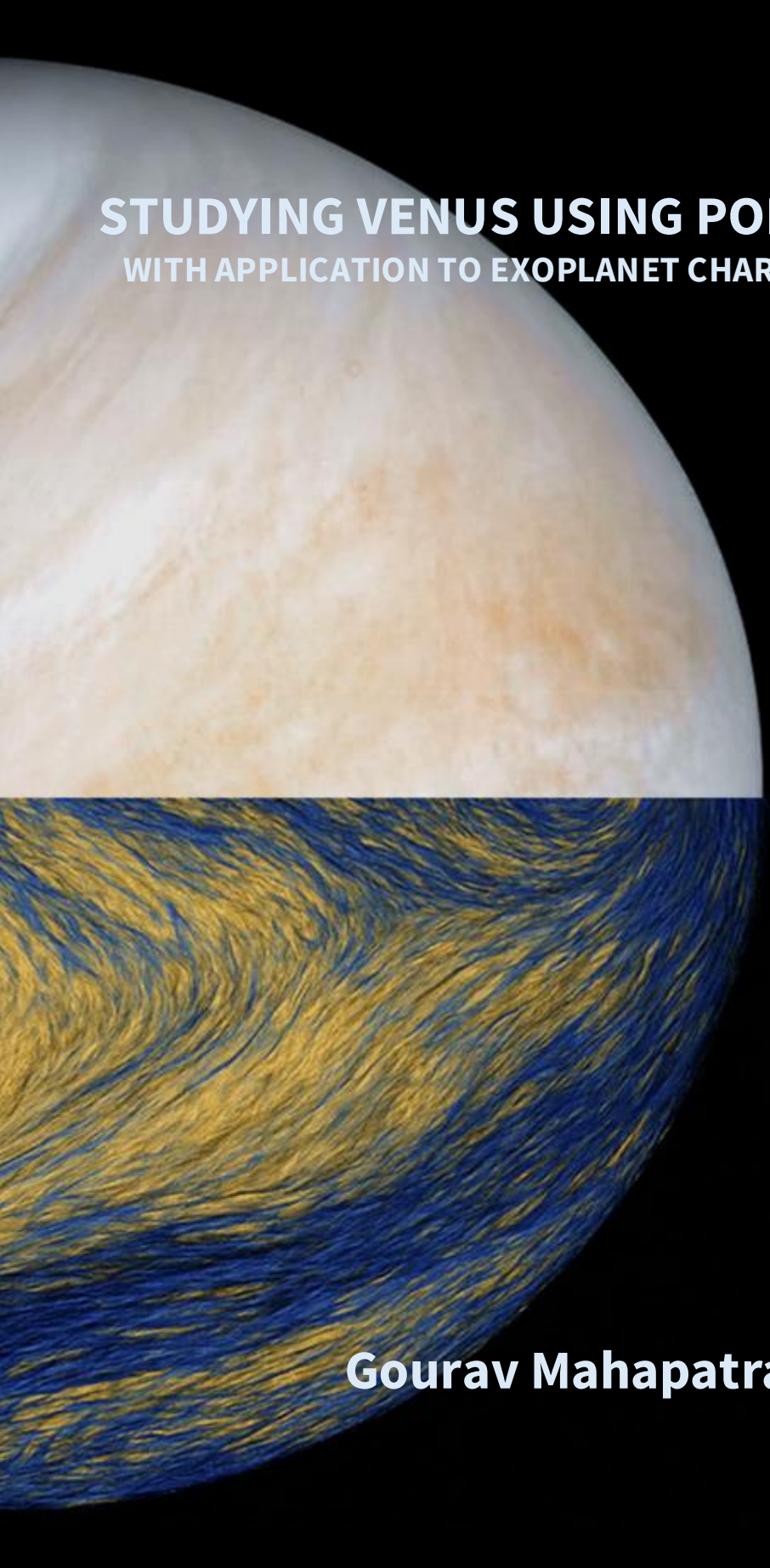

STUDYING VENUS USING POLARIMETRY

WITH APPLICATION TO EXOPLANET CHARACTERIZATION

Gourav Mahapatra

STUDYING VENUS USING POLARIMETRY

WITH APPLICATION TO EXOPLANET CHARACTERIZATION

STUDYING VENUS USING POLARIMETRY

WITH APPLICATION TO EXOPLANET CHARACTERIZATION

Proefschrift

ter verkrijging van de graad van doctor
aan de Technische Universiteit Delft,
op gezag van de Rector Magnificus Prof. dr. ir. T.H.J.J. van der Hagen,
voorzitter van het College voor Promoties,
in het openbaar te verdedigen op maandag 2 juni 2025 om 15:00 uur

door

Gourav MAHAPATRA

Ingenieur in luchtvaart- en ruimtevaarttechniek,
Technische Universiteit Delft, Delft, Nederland
geboren te Rourkela, India.

Dit proefschrift is goedgekeurd door de promotoren

Samenstelling promotiecommissie bestaat uit:

Rector Magnificus,	voorzitter
Prof. dr. L.L.A. Vermeersen,	Technische Universiteit Delft, promotor
Dr. D.M. Stam,	Technische Universiteit Delft, copromotor
Onafhankelijke leden:	
Prof. dr. A. P. Siebesma	Technische Universiteit Delft
Dr. S. Paardekooper	Technische Universiteit Delft
Dr. E. Marcq	UVSQ, Frankrijk
Dr. F. Vanhellemont	Royal Belgian Institute for Space Aeronomy, België
Prof. dr. ir. H.W.J. Russchenberg	Technische Universiteit Delft, reservelid
Overige leden:	
Dr. L. C. G. Rossi	Technische Universiteit Delft

This work was supported by the Netherlands Organisation for Scientific Research (NWO) through the User Support Programme Space Research, project number ALW GO 15-37.

Keywords: Venus, polarimetry, radiative transfer, clouds, exo-planet, atmospheres, gravity waves

Front & Back: The cover combines a Mariner 10 image of Venus (top) with a stylized version inspired by van Gogh's Starry Night (bottom), symbolizing the hidden atmospheric waves that shape Venus's dynamic cloud layers.

ISBN 978-94-6510-710-3

An electronic version of this dissertation is available at
http://repository.tudelft.nl/.

For instance, on the planet Earth, man had always assumed that he was more intelligent than dolphins because he had achieved so much—the wheel, New York, wars and so on—whilst all the dolphins had ever done was muck about in the water having a good time. But conversely, the dolphins had always believed that they were far more intelligent than man—for precisely the same reasons.

Douglas Adams, The Hitchhiker's Guide to the Galaxy

CONTENTS

SUMMARY

Venus presents a compelling case study of the greenhouse effect, resulting in the highest surface temperatures of any planet in our solar system. Despite its similarities to Earth in origin and size, Venus has a vastly different atmosphere, dominated by CO_2 and thick sulfuric acid clouds undergoing retrograde super-rotation. To better understand Venus' climate and characterise it, this thesis employs the technique of polarimetry to develop precise computational models of light scattering in its atmosphere. These models are compared with existing observations to investigate dynamic atmospheric phenomena, such as gravity waves and variations in cloud top altitude.

Planet-wide gravity waves were observed by the Japanese Akatsuki spacecraft in thermal infrared wavelengths on Venus. These waves were attributed to the underlying mountainous topography and are generated when wind flows over mountains and propagate to the middle and upper cloud layers. In chapter 2, we explore the possibility of whether orographic gravity waves of similar nature would be observable through polarimetry. As gravity waves propagate, they alter atmospheric density and aerosol distribution, making them observable through various imaging techniques. While direct and thermal imaging have primarily been used to detect these waves, those affecting higher altitudes cause much smaller changes in atmospheric density as compared to the cloud tops. Consequently, these high-altitude waves are challenging to observe with direct imaging and have been detected primarily through in-situ sensors or night-glow measurements. Unlike direct imaging, which captures both polarized and unpolarized light, polarimetry is more sensitive to density variations due to the high degree of polarization imparted by gas molecules, which also varies with solar and viewing geometry.

We use the Venus Mesoscale Model, a general circulation model that accurately reproduces the generation and propagation of gravity waves, to simulate the density changes caused by orographic gravity waves. Using a precise radiative transfer code capable of computing polarized fluxes, we calculate the total and polarized fluxes at three wavelengths: 300 nm, 600 nm, and 900 nm. Our numerical simulations reveal that the polarized flux F and degree of polarization P of sunlight reflected by Venus are sensitive to variations in atmospheric gas density above the clouds. This sensitivity is due to increased scattering by gas molecules as gas density rises. Conversely, F is more influenced by cloud properties. Wave-induced variations decrease with increasing wavelength as Rayleigh scattering diminishes. Therefore, polarimetric observations at shorter wavelengths, particularly around 300 nm, are better suited for detecting these waves.

Chapter 3 reports the serendipitous observation of planet-wide concentric wave-like rings in polarized fluxes across the sunlit side of Venus. These observations were conducted using the highly sensitive ExPo instrument, capable of detecting changes in polarization as small as 10^{-4}, mounted on the ground-based William Herschel Telescope (WHT) of the Isaac Newton Group (ING) of telescopes on La Palma, Canary Islands, Spain. Past missions, such as Pioneer Venus and Venus Express, have observed upper-

atmospheric gravity waves on Venus through in-situ measurements. Theoretically, these waves are believed to contribute to the driving mechanisms of the super-rotating zonal flow by transferring momentum from the cloud tops and depositing energy in the thermosphere. We hypothesize that the observed rings are atmospheric gravity waves propagating through Venus' upper atmosphere. To test this hypothesis, we developed a numerical model to account for density variations caused by these waves in the upper atmosphere and computed the reflected total and polarized fluxes. Our simulations indicate that both F and P across the disk are primarily determined by the cloud layer's characteristics. However, a 5% to 10% change in the carbon dioxide column gas density above the clouds can produce detectable changes in polarization within ExPo's sensitivity, without significantly affecting observations in Venus' brightness. These density waves could be triggered by the intense irradiation of the sub-solar region and spread across the planet following the known sub-solar to anti-solar flow. Follow-up polarimetric observations are required to validate this potential discovery.

In Chapter 4, we develop a radiative transfer model to examine the behavior of P in Venus' short-wave infrared absorption bands. This study aims to determine if this wavelength region is sensitive to variations in clouds and haze, potentially enabling us to measure their properties. Light reflected from a planet's atmosphere in the wavelength bands corresponding to gaseous absorption contains unique information compared to the continuum bands. For Venus, whose atmosphere is predominantly CO_2, scattered light in the absorption bands is more sensitive to gas or aerosol particles higher up in the atmosphere because of the absorption by gas at lower altitudes. Since P of light is highly sensitive to particle sizes and composition, measuring it in absorption bands can provide accurate information on the vertical distribution of aerosols in Venus's atmosphere. The SPICAV-IR spectrometer on the Venus Express spacecraft measured light in CO_2 absorption bands in short-wave infrared. Although not originally designed to measure polarization, partial polarization could be derived from its orthogonally polarized flux measurements.

We tested the sensitivity of reflected light within the 1.4 - 1.5 μm absorption bands to cloud top altitude, cloud scale height, and haze optical thickness. To expedite our otherwise time-consuming flux computations within the absorption bands, we employed the correlated-k method, a fast yet approximate technique. Our sensitivity analysis, utilizing radiative transfer numerical models with instrument response functions having spectral width of 1 nm, 5 nm, and that of SPICAV-IR instrument, indicates that relative measurements of both F and P are sensitive to changes in cloud top altitude. However, only P shows significant variations with changes in haze optical thickness. Both F and P do not exhibit significant variations with changes in cloud scale height, making it challenging to retrieve this parameter within the absorption band. Analysis of P data from selected orbits of SPICAV-IR with high signal-to-noise ratios within these CO_2 absorption bands shows that the data largely agrees with our Venus radiative transfer models. We find that the increase in $|P|$ within the absorption bands is to be expected, and its sign depends on the aerosols present in the atmosphere and the observation geometry. Near the Venus equator, scattering by cloud particles dominates due to the low haze optical thickness, as observed in SPICAV-IR data from equatorial and mid-latitude regions. Closer to the poles, sub-micron haze particles dominate the scattering, resulting in a strong positive

P. Our findings highlight the importance of incorporating polarization-sensitive instruments with high spectral resolution in future Venus missions to accurately derive atmospheric aerosol properties.

In Chapter 5, we investigate the total flux and polarization of starlight reflected by terrestrial exoplanets, focusing on the evolutionary stages of Venus as described by Bullock and Grinspoon (2001). Our goal is to identify characteristic signatures of exo-Venuses at various evolutionary stages to guide future telescope design. We calculate the disk-integrated total and polarized fluxes of light reflected between 0.3 and 2.5 μm for planets with atmospheric properties corresponding to four evolutionary stages from an Earth-like atmosphere with liquid water clouds to a present day Venus atmosphere with a CO_2 atmosphere and sulfuric acid clouds. These signals have been computed for both disk-resolved and disk-integrated planets as a function of the planet's phase angle α, considering model planets orbiting our neighboring solar-type star, Alpha Centauri A, within predicted stable orbits in its habitable zone. For the disk-integrated cases, we also computed the planet-star contrast C as a function of α and λ to determine the technical requirements for detecting planetary signals against the background starlight. The P of reflected starlight varies more with α and λ than F. In the visible spectrum, an Earth-like atmosphere with water clouds shows the highest polarization due to Rayleigh scattering and the rainbow feature near 40° phase angle. In the near-infrared, a Venus-like CO_2 atmosphere with thin water clouds exhibits prominent polarization due to Rayleigh-like scattering by small cloud droplets. We find that a planet orbiting Alpha Centauri A would cause temporal variations of about 10^{-13} W/m^2/m (defined per wavelength) in total F and 10^{-11} in total P, assuming a spatially unresolved star-planet system. The star-planet contrasts C are around 10^{-10}, proportional to planetary flux. Current polarimeters lack the sensitivity to distinguish between the evolutionary phases of unresolved terrestrial exoplanets, requiring a sensitivity of 10^{-10} to detect the planetary signal against unpolarized starlight. However, a telescope/instrument achieving planet-star contrasts below 10^{-9} could observe the significant polarization variations with α, distinguishing an exo-Earth from an exo-Venus based on their unique polarization signatures.

In conclusion, this thesis demonstrates that light reflected from Venus' atmosphere in short-wave infrared wavelengths provides unique insights into the vertical distribution of clouds and haze. The sign of polarization reveals whether the signal originates mainly from clouds or haze. Preliminary analysis of SPICAV-IR data is in agreement with our findings. These findings are crucial for the upcoming EnVision mission, which features the polarimetry capable VenSpec-H instrument. We also modelled the signals from hypothetical exo-Venus and exo-Earth around a star, and find that measuring P using a highly sensitive polarimeter, with a sensitivity of less than 10^{-10}, could enable us to derive cloud properties on exoplanets and detect potential false positives. Finally, we have shown in this thesis that gravity waves on Venus, excited by underlying orography, cause density changes in CO_2 that can be observed with instruments capable of measuring P in visible wavelengths. Polarization increases with decreasing wavelength, making it preferable to observe these gravity waves at shorter wavelengths, for example at 300 nm. Our numerical computations indicate that gas column density changes of 5 to 10% above the clouds are necessary to produce the planet-wide rings on Venus observed by the ground-based ExPo instrument. We hypothesize that these waves are

upper-atmospheric gravity waves caused by solar irradiation near the sub-solar point. To our knowledge, this is the first attempt to use polarimetry for detecting atmospheric gravity waves.

SAMENVATTING

Het broeikaseffect is goed te zien op Venus. Het is de reden dat Venus de hoogste oppervlaktetemperaturen heeft van alle planeten in ons zonnestelsel. Ondanks zijn overeenkomsten met de Aarde qua oorsprong en grootte, heeft Venus een sterk verschillende atmosfeer, gedomineerd door CO_2 en dikke zwavelzuurwolken die in retrograde superrotatie zijn. Om Venus' klimaat beter te begrijpen en te karakteriseren, maakt dit proefschrift gebruik van de techniek van polarimetrie om nauwkeurige computationele modellen van lichtverstrooiing in de atmosfeer te ontwikkelen. Deze modellen worden vergeleken met bestaande waarnemingen om dynamische atmosferische fenomenen te onderzoeken, zoals zwaartekrachtsgolven en variaties in de wolkentophoogte.

Wereldwijde zwaartekrachtsgolven werden waargenomen door het Japanse Akatsuki-ruimtevaartuig in thermische infrarode golflengten op Venus. Deze golven werden toegeschreven aan de onderliggende bergtopografie en ontstaan wanneer wind over bergen stroomt en zich voortplant naar de middelste en bovenste wolkenlagen. In hoofdstuk 2 van dit proefschrift onderzoeken we of zwaartekrachtsgolven van vergelijkbare aard waarneembaar zouden zijn door middel van polarimetrie. Wanneer zwaartekrachtsgolven zich voortplanten, veranderen ze de atmosferische dichtheid en aerosolverdeling, waardoor ze waarneembaar worden via verschillende beeldvormingstechnieken. Hoewel voornamelijk directe en thermische beeldvorming zijn gebruikt om deze golven te detecteren. Echter veroorzaken die op grotere hoogten veel kleinere veranderingen in de atmosferische dichtheid. Daarom zijn deze hooggelegen golven moeilijk te observeren met directe beeldvorming en zijn ze voornamelijk gedetecteerd via in-situ sensoren of nachtlichtmetingen. In tegenstelling tot directe beeldvorming, die zowel gepolariseerd als ongepolariseerd licht vastlegt, is polarimetrie gevoeliger voor dichtheidsvariaties vanwege de hoge mate van polarisatie veroorzaakt door gasmoleculen, die ook varieert met de zonne- en kijkgeometrie.

We gebruiken het Venus Mesoscale Model, een algemeen circulatiemodel dat nauwkeurig het ontstaan en de voortplanting van zwaartekrachtsgolven reproduceert, om de dichtheidsveranderingen veroorzaakt door orografische zwaartekrachtsgolven te simuleren. Met behulp van een nauwkeurige stralingsoverdrachtcode die gepolariseerde fluxen kan bepalen, berekenen we de totale en gepolariseerde fluxen bij drie golflengten: 300 nm, 600 nm en 900 nm. Onze numerieke simulaties laten zien dat de gepolariseerde flux F en de mate van polarisatie P van door Venus weerkaatst zonlicht gevoelig zijn voor variaties in de atmosferische gasdichtheid boven de wolken. Deze gevoeligheid is te danken aan de toename van verstrooiing door gasmoleculen naarmate de gasdichtheid toeneemt. Omgekeerd wordt F beïnvloed door de eigenschappen van de wolken. Door golven veroorzaakte variaties nemen af met toenemende golflengte naarmate Rayleigh-verstrooiing afneemt. Daarom zijn polarimetrische waarnemingen bij kortere golflengten, met name rond 300 nm, beter geschikt om deze golven te detecteren.

Hoofdstuk 3 rapporteert de toevallige waarneming van wereldwijde concentrische

ringachtige golven in gepolariseerde fluxen over de verlichte zijde van Venus. Deze waarnemingen werden uitgevoerd met het zeer gevoelige ExPo-instrument, dat veranderingen in polarisatie kan detecteren tot 10^{-4}. Het instrument is gemonteerd op de grondgebaseerde William Herschel Telescope (WHT) van de Isaac Newton Group (ING) of telescopes op La Palma, Canarische Eilanden, Spanje. Eerdere missies, zoals Pioneer Venus en Venus Express, hebben zwaartekrachtsgolven in de bovenste atmosfeer van Venus waargenomen via in-situ metingen. Theoretisch wordt aangenomen dat deze golven bijdragen aan de drijvende mechanismen van de superroterende zonale stroming door momentum van de wolkentoppen over te brengen en energie in de thermosfeer te deponeren. We veronderstellen dat de waargenomen ringen atmosferische zwaartekrachtsgolven zijn die zich voortplanten door de bovenste atmosfeer van Venus. Om deze hypothese te testen, hebben we een numeriek model ontwikkeld om rekening te houden met dichtheidsvariaties veroorzaakt door deze golven in de bovenste atmosfeer en de gereflecteerde totale en gepolariseerde fluxen berekend. Onze simulaties geven aan dat zowel F als P over de schijf voornamelijk worden bepaald door de kenmerken van de wolkenlaag. Een verandering van 5% tot 10% in de koolstofdioxide kolomdichtheid boven de wolken kan echter detecteerbare veranderingen in polarisatie produceren binnen de gevoeligheid van ExPo, zonder de helderheid van Venus aanzienlijk te beïnvloeden. Deze dichtheidsgolven kunnen worden veroorzaakt door de intense bestraling van de sub-solare regio en zich over de planeet verspreiden via de bekende sub-solaire naar anti-solaire stroming. Opvolgende polarimetrische waarnemingen zijn nodig om deze potentiële ontdekking te valideren.

In hoofdstuk 4 ontwikkelen we een stralingsoverdrachtmodel om het gedrag van P in de korte-golf infrarode absorptiebanden van Venus te onderzoeken. Deze studie heeft als de doel te bepalen of dit golflengtegebied gevoelig is voor variaties in wolken en nevel, waardoor we mogelijk hun eigenschappen kunnen meten. Licht dat wordt weerkaatst door de atmosfeer van een planeet in de golflengtebanden die overeenkomen met gasabsorptie, bevat unieke informatie in vergelijking met de continuümbanden. Voor Venus, waarvan de atmosfeer voornamelijk uit CO_2 bestaat, is verstrooid licht in de absorptiebanden gevoeliger voor gas- of aerosoldeeltjes hoger in de atmosfeer vanwege de absorptie van gas op lagere hoogten. Omdat P van licht zeer gevoelig is voor deeltjesgrootte en samenstelling, kan het meten ervan nauwkeurige informatie verschaffen over de verticale verdeling van aerosolen in de atmosfeer van Venus. De SPICAV-IR spectrometer op het Venus Express-ruimtevaartuig heeft licht gemeten in CO_2-absorptiebanden in het korte-golflengte infrarood. Hoewel oorspronkelijk niet ontworpen om polarisatie te meten, kon gedeeltelijke polarisatie worden afgeleid uit zijn orthogonaal gepolariseerde fluxmetingen.

We testten de gevoeligheid van gereflecteerd licht binnen de 1.400 - 1.500 nm absorptiebanden voor wolkentophoogte, schaalhoogte van de wolken en optische dikte van nevel. Om onze anders tijdrovende fluxberekeningen binnen de absorptiebanden te versnellen, gebruikten we de correlated-k methode voor een snelle benadering. Onze gevoeligheidsanalyse, met behulp van numerieke stralingsoverdrachtmodellen met instrumentresponsfuncties met een spectrale breedte van 1 nm, 5 nm en die van het SPICAV-IR-instrument, geeft aan dat relatieve metingen van zowel F als P gevoelig zijn voor veranderingen in wolkentophoogte. Echter vertoont P significante variaties bij veran-

deringen in de optische dikte van nevel. Zowel F als P vertonen geen significante variaties bij veranderingen in schaalhoogte van de wolken, wat het moeilijk maakt om deze parameter binnen de absorptieband te bepalen. Analyse van P-gegevens van geselecteerde banen van SPICAV-IR met hoge signaal-ruisverhoudingen binnen deze CO_2-absorptiebanden toont aan dat de gegevens grotendeels overeenkomen met onze stralingsoverdrachtmodellen voor Venus. We constateren dat de toename in $|P|$ binnen de absorptiebanden te verwachten is en dat het teken afhangt van de aanwezige aerosolen in de atmosfeer en de waarnemingsgeometrie. Nabij de evenaar van Venus domineert verstrooiing door wolkendeeltjes vanwege de lage optische dikte van nevel, zoals waargenomen in SPICAV-IR-gegevens uit de equatoriale en middelhoge breedtegraden. Dichter bij de polen domineren submicron neveldeeltjes de verstrooiing, wat resulteert in een sterk positieve P. Onze bevindingen benadrukken het belang van het opnemen van polarisatiegevoelige instrumenten met hoge spectrale resolutie in toekomstige Venus-missies om nauwkeurige atmosferische aerosolkenmerken af te leiden.

In hoofdstuk 5 onderzoeken we de totale flux en polarisatie van door aardachtige exoplaneten weerkaatst sterrenlicht, met de nadruk op de evolutionaire stadia van Venus zoals beschreven door Bullock and Grinspoon (2001). Ons doel is om karakteristieke kenmerken van exo-Venussen in verschillende evolutionaire stadia te identificeren om zo te helpen bij toekomstige telescoopontwerpen. We berekenen de totale en gepolariseerde schijf-geïntegreerde fluxen van licht dat wordt weerkaatst tussen 300 en 2.500 nm voor planeten met atmosferische eigenschappen die overeenkomen met vier evolutionaire stadia, van een aardachtige atmosfeer met vloeibare waterwolken tot een hedendaagse Venus-atmosfeer met een CO_2-atmosfeer en zwavelzuurwolken. Deze signalen zijn berekend voor zowel schijf-geresolveerde als schijf-geïntegreerde planeten als functie van de fasehoek α van de planeet, rekening houdend met modelplaneten die om onze naburige zonachtige ster, Alpha Centauri A, draaien binnen voorspelde stabiele banen in de bewoonbare zone. Voor de schijf-geïntegreerde gevallen hebben we ook het planeet-ster contrast C berekend als functie van α en λ om de technische vereisten voor het detecteren van planetaire signalen tegen het achtergrondsterrenlicht te bepalen. De P van weerkaatst sterrenlicht varieert meer met α en λ dan F. In het zichtbare spectrum vertoont een aardachtige atmosfeer met waterwolken de hoogste polarisatie door Rayleigh-verstrooiing en het regenboogkenmerk bij een fasehoek van ongeveer 40°. In het nabije infrarood vertoont een Venus-achtige CO_2-atmosfeer met dunne waterwolken prominente polarisatie door Rayleigh-achtige verstrooiing door kleine wolkendruppels. We constateren dat een planeet die om Alpha Centauri A draait, tijdelijke variaties van ongeveer 10^{-13} W/m^3 in totale F en 10^{-11} in totale P zou veroorzaken, uitgaande van een ruimtelijk onopgelost ster-planeet systeem. De planeet-ster contrasten C zijn ongeveer 10^{-10}, evenredig aan de planetaire flux. Huidige polarimeters missen de gevoeligheid om de evolutionaire stadia van onopgeloste aardse exoplaneten te onderscheiden, omdat een gevoeligheid van 10^{-10} vereist is om het planetaire signaal te detecteren tegen ongepolariseerd sterrenlicht. Een telescoop/instrument dat planeet-ster contrasten onder 10^{-9} kan meten, zou echter de significante polarisatievariaties met α kunnen waarnemen, waardoor op basis van hun unieke polarisatiekenmerken onderscheid gemaakt kan worden tussen een exo-Aarde en een exo-Venus.

Samenvattend laat dit proefschrift zien dat licht dat wordt gereflecteerd door de at-

mosfeer van Venus in golflengten van het kortegolf-infrarood unieke inzichten biedt in de verticale verdeling van wolken en nevel. De polarisatiegraad onthult of het signaal voornamelijk afkomstig is van wolken of nevel. Voorlopige analyse van SPICAV-IR-gegevens stemt overeen met onze bevindingen. Deze resultaten zijn van cruciaal belang voor de aankomende EnVision-missie, die is uitgerust met het VenSpec-H-instrument dat polarizatie bevat. We hebben ook de signalen van hypothetische exo-Venus en exo-Aarde rond een ster gemodelleerd en geconcludeerd dat het meten van P met een zeer gevoelige polarimeter, met een gevoeligheid van minder dan 10^{-10}, ons in staat kan stellen de wolkeneigenschappen op exoplaneten af te leiden en potentiële false positives te detecteren. Ten slotte hebben we in dit proefschrift aangetoond dat zwaartekrachtsgolven op Venus, veroorzaakt door onderliggende orografie, dichtheidsveranderingen in CO_2 veroorzaken die kunnen worden waargenomen met instrumenten die P in zichtbare golflengten kunnen meten. De polarisatie neemt toe met afnemende golflengte, waardoor deze zwaartekrachtsgolven het beste bij kortere golflengten kunnen worden waargenomen bijvoorbeeld bij 300 nm. Onze numerieke berekeningen geven aan dat veranderingen in de gasdichtheidskolom van 5 tot 10% boven de wolken nodig zijn om de planeetbrede ringen op Venus te produceren die zijn waargenomen door het grondgebaseerde ExPo-instrument. We veronderstellen dat deze golven zwaartekrachtsgolven in de bovenste atmosfeer zijn, veroorzaakt door zonnestraling nabij het sub-solaire punt. Voor zover wij weten, is dit de eerste poging om polarisatie te gebruiken voor het detecteren van atmosferische zwaartekrachtsgolven.

1

INTRODUCTION

What then, must Venus have no Sea, or do the Waters there reflect the Light more than ours do, or their Land less? or rather (which is most probable in my opinion) is not all that Light we see reflected from an Atmosphere surrounding Venus, which being thicker and more solid than that in Mars or Jupiter, hinders our seeing any thing of the Globe it self, and is at the same time capable of sending back the Rays that it receives from the Sun?

Christian Huygens in Cosmotheoros

1

Throughout human civilization, Venus has been a prominent planet, observed, studied, and even deified due to its brightness and visibility with the naked eye as the brightest object in the sky after the Sun and the Moon. Early texts, such as the ancient Hindu text Atharvaveda, refer to Venus as one of the nine planets or Navagraha. The astronomer Aryabhatta studied its motion and calculated its orbital period to an impressive accuracy of within five minutes in the 1st millennium CE (Burgess and Gangooly, 1989). Venus' name is derived from the ancient Roman goddess, and it is associated with beauty and love. The painting "Nascita di Venere" or "The Birth of Venus" by Boticelli is perhaps the most famous representation of the planet's personification. Venus' smooth and bright appearance has also shrouded it in mystery. The 17th-century Dutch astronomer Christiaan Huygens noted in his book "Cosmotheoros" that Venus appears uniform when observed from Earth, unlike other planets. He correctly conjectured that Venus must be covered with a thick atmosphere, which causes the light reflected from it to appear without irregularities when viewed through a telescope on Earth.

The composition of the clouds has been a mystery until the 1970s. Various ground based observation techniques including spectrometry proved to be challenging in deciphering the nature of these clouds as various chemical candidates could fit the observed light spectra. By studying the degree and direction of polarization of the reflected light using ground based instruments, astronomers could deduce that these cloud particles are primarily sulphuric acid droplets. Thus, polarimetry played a crucial role in confirming the nature of Venus' clouds. When light interacts with gas, dust, and cloud particles in a planet's atmosphere, it generally becomes polarized. Polarization refers to light in which the electric field oscillates in a specific plane and polarimetry is a field of study that involves measuring and analyzing the polarization properties of light.

This thesis employs the techniques of polarimetry to develop precise computational models of the scattering of light in Venus' atmosphere. The model simulations are compared with existing observations to investigate dynamic atmospheric phenomena, such as gravity waves, and variations in cloud top altitude. This chapter serves as an introduction to the planet Venus, its atmosphere, and cloud structure. Additionally, it provides an overview of how polarimetry can be utilized to deduce essential properties of Venus' clouds and atmospheric conditions.

1.1. VENUS AND ITS ATMOSPHERE

At first glance, Venus appears quite similar to Earth, with both planets sharing roughly the same size (approximately 0.95 times the radius of Earth) and mass, and formed from similar materials, probably with a comparable primary atmospheric inventory. However, upon closer examination, significant differences become apparent. Venus has a distinct retrograde rotation with a sidereal period of 243 days, meaning that it takes longer for Venus to complete one rotation around its axis than it takes to complete a revolution around the Sun. This unique characteristic results in an atmosphere dynamics that is markedly different from that of Earth.

The atmosphere of Venus is almost entirely composed of carbon dioxide and is thick enough to exert a surface pressure of approximately 93 bars. Because carbon dioxide absorbs radiation at infrared wavelengths, this atmosphere has led to a strong greenhouse effect, resulting in a mean surface temperature of 737 K, making Venus the hottest ter-

Characteristic	Earth	Venus
Diameter	12,742 km	12,104 km
Mass	5.97×10^{24} kg	4.87×10^{24} kg
Average Density	5.52 g/cm^3	5.24 g/cm^3
Surface Gravity	9.81 m/s^2	8.87 m/s^2
Orbital Period	365.25 days	225 Earth days
Rotation Period	23.93 hours	-243.02 Earth days (retrograde)
Surface Temperature	~15°C	~467°C
Atmosphere Composition	78% N_2, 21% O_2	96.5% CO_2, 3.5% N_2
Atmospheric Pressure	1 bar	~92 bar

Table 1.1: Comparison of basic characteristics of Earth and Venus

restrial planet in the solar system. Additionally, the atmosphere of Venus is in a state of super-rotation, it rotates faster than the planet itself at cloud level. The atmosphere rotates at a speed of approximately 4 Earth days, as deduced primarily through the observation of cloud propagation speeds (Read and Lebonnois, 2018). Although it was well known by the 18th century that Venus has an atmosphere, there was no consensus until the 1960s on whether the surface was hospitable due to its unbroken and thick cloud deck. This cloud deck, composed primarily of sulfuric acid droplets with a concentration greater than 70%, reflects 80% of solar radiation, in contrast to Earth's albedo of about 33%.

1.2. POLARIMETRY AS A TOOL TO STUDY THE ATMOSPHERE OF VENUS

Sunlight that is incident on a planet's atmosphere is scattered by the molecules and larger particles within the atmosphere (Hansen and Travis (1974)). Since light is electromagnetic radiation, it can be described by its intensity, wavelength and state of polarization. Light scattered by the constituents of an atmosphere goes through a change in its intensity and state of polarization. Various particles modify light's polarization state differently and thus understanding the nature of such changes can help us to identify the nature of the particles that caused it. The nature of scattered light depends upon the chemical composition of such particles and their shape and size. The degree of polarization is commonly defined as the ratio of the amount of polarized light to the total light received. Polarized flux encompasses both circular and linear states of polarization.

The nature and composition of the clouds of Venus was unknown until the beginning of 1970s. The clouds were primarily studied through the absorption spectra observed from the reflected light off the planet which allowed for many possible compositions. Some of them were: H_2O ice, solid CO_2, carbon suboxide C_3O_2, NaCl, formaldehyde CH_2O, hydro-carbons, hydrocarbon-amide polymers, polywater, ammonium nitride, calcium and magnesium carbonates, mercury and mercury compounds and aqueous solutions of hydrochloric acid HCl.nH$_2$O and sulphuric acid H_2SO_4.nH$_2$O (Hansen

and Hovenier, 1974).

Using ground based polarization measurements spanning multiple decades by several astronomers (Lyot, 1929; Coffeen and Gehrels, 1969; Dollfus and Coffeen, 1970; Veverka, 1971) and an accurate radiative transfer model (Hansen and Hovenier, 1971) that could take into account the multiple scattering effect of polarized light within the thick cloud layers of Venus, Hansen and Hovenier (1974) could derive the cloud particle refractive index, size and distribution and thus based on this information deduced the cloud composition to be sulphuric acid solution. By computing the planet's integrated degree of polarization as a function of the planet's phase angle (the angle between the star, the planet, and the observer) at several wavelengths in both the visible and the near-infrared, they could establish the cloud particles to be spherical with an effective cloud particle radius of ~1.05±0.1 μm and an effective variance of 0.07±0.02. Fig. 1.1 shows the observations at the visible wavelength λ = 0.55 μm and the best fit obtained by Hansen and Hovenier (1974) with cloud particles having effective radius of 1.05 μm and effective variance of 0.07 and the particle refractive index at λ = 0.55 μm to be 1.44. It is important to note that these set of observations were taken over multiple decades of ground-based observations and hence have a temporal variability aspect to them as well (see Del Genio and Rossow (1982), Knibbe et al. (1998), Marcq et al. (2013), Vandaele et al. (2017), Marcq et al. (2018)).

The Pioneer Venus mission launched to Venus in 1978, carried an Orbiter Cloud Photopolarimeter (OCPP) instrument capable of observing the intensity, degree of polarization and angle of polarization of light at 4 wavelengths: 270, 365, 550 and 935 nm (Kawabata et al., 1980). It confirmed the micron sized cloud particles predicted by Hansen and Hovenier (1974) using ground based polarimetric observations. More importantly, it also found an extended region with haze particles above the micron-sized clouds with effective radius of 0.23 ± 0.04 μm and effective variance of 0.18 ± 0.1 having significant spatial and temporal variability observed through the missions lifetime (Kawabata et al., 1980). The haze optical thickness varied spatially from 0.06 to 0.8 at λ = 365 nm and between the morning and evening terminators exhibiting diurnal variation. Sato et al. (1996) performed an analysis over a longer term of Pioneer Venus OCPP data covering the first 282 days to specifically study the temporal variation of the haze above clouds over the polar regions of the planet. They found that the particles effective radius, variance and the refractive index were more or less similar to previous results obtained by Kawabata et al. (1980) at both poles but there were significant changes observed temporally. They found that the haze optical thickness exhibited an oscillatory behavior possibly having a time period of 10^6-10^7 seconds which is similar to the meridional circulation time scales of Venus' atmosphere (Schubert et al., 1980; Del Genio and Rossow, 1990; Sato et al., 1996). A decline in haze optical thickness temporally was also observed by Sato et al. (1996) (Figs. 7a and 7b) and this trend was later confirmed by Knibbe et al. (1998) and Braak et al. (2002).

1.3. STRUCTURE OF VENUS' CLOUDS

The thick and ubiquitous cloud deck spans vertically between altitudes 48 and 80 km approximately. These clouds are quite acidic consisting of sulphuric acid droplets with concentration of approximately 75 %. They are opaque in most of UV, visible and in-

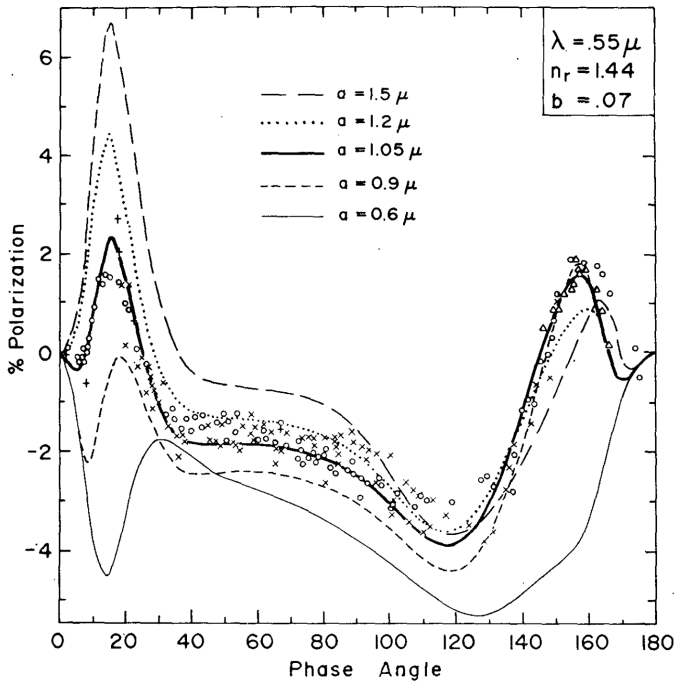

Figure 1.1: Theoretical computations made by Hansen and Hovenier (1974) for fitting polarization of sunlight observations at λ = 0.55 μm. The degree of polarization is defined here as the ratio of polarized light to the total light. It is positive when the electric field is perpendicular to the plane of scattering and negative when the electric field is parallel to the plane of scattering. The O's are wide-band visual observations by Lyot (1929) while the other observations are for an intermediate bandwidth filter centered at λ = 0.55 μm; the X's were obtained by Coffeen and Gehrels (1969), the +'s by Coffeen (cf. Dollfus and Coffeen (1970)), and the Δ's (which refer to the central part of the crescent) by Veverka (1971). The theoretical curves are all for a refractive index 1.44, the size distribution follows a two-parameter Gamma function with b=0.07, and a Rayleigh contribution f_R=0.045. The different curves show the degree of polarization as a function of the effective radius of particles.

frared wavelengths making it almost impossible to observe through them which made it very difficult to observe its surface, thus remaining shrouded in mystery for a long time. The formation of these thick clouds start with the volcanic out-gassing of SO_2 and H_2O. The presence of greenhouse gases like CO_2 and H_2O leads to the absorption of outgoing thermal radiation from surface, increasing the temperatures which leads to vaporization of liquid water which eventually leads to the loss of most of H_2O into space (Titov et al., 2018). The remaining H_2O reacts with SO_3, which has been oxidized from SO_2 through photochemistry (Yung and DeMore, 1982) to form H_2SO_4 where the local atmospheric conditions permit which for Venus is above 48 km.

Because of its thickness and high opacity, the vertical structure of Venus' atmosphere could only be understood thanks to the Venera, Pioneer Venus, and Vega descent probes that could conduct in-situ measurements (Esposito et al., 1983; Ragent et al., 1985). In particular, the Pioneer Venus LCPS experiment found three distinct cloud regions spanning 20 km vertically and with haze layers present both above and below the cloud decks on both sides vertically (Knollenberg and Hunten, 1979, 1980). Figure 1.2 shows the vertical cloud profiles shown as number densities and extinction coefficients found through this experiment. Three distinct particle modes (1, 2, 3) were identified based on the particles effective radius: 0.15-0.2 μm (mode 1), 1-1.25 μm (mode 2) and 3.5-4.0 μm (mode 3).

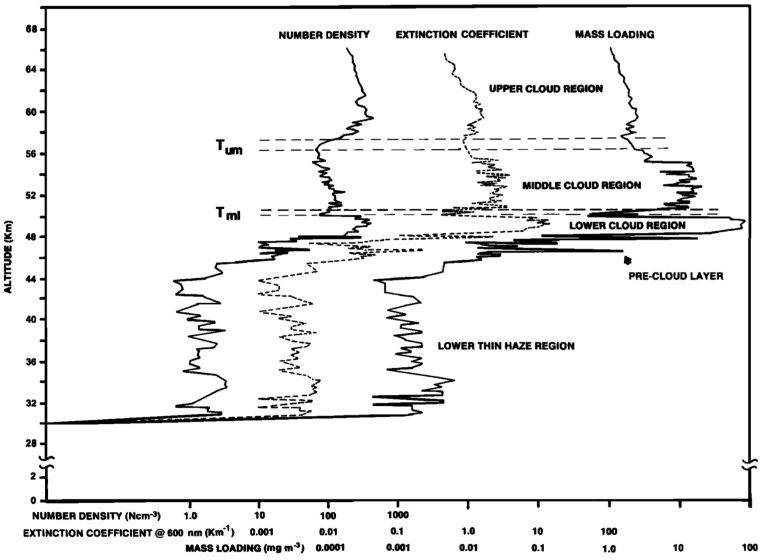

Figure 1.2: Vertical profiles of aerosol number density, extinction coefficient at 600 nm, and mass loading in Venus's atmosphere as measured by the Large Probe Cloud Particle Size (LCPS) experiment aboard the Pioneer Venus mission. The figure highlights distinct cloud layers—upper, middle, and lower—as well as the pre-cloud and lower thin haze regions. Adapted from Knollenberg and Hunten (1980).

The upper cloud region (57 - 70 km) is the region where sulphuric acid is produced from H_2O and SO_2. It is populated by sub-micron and micron-sized mode 1 and mode 2 particles. The middle and lower cloud decks are not very easily distinguishable except

for an increased particle number density and size in the lower cloud deck close to 50 km altitude (Titov et al., 2018, and references there in). Both these regions exhibit tri-modal particle size distribution.

European Space Agency's Venus Express (VEx) mission launched in November 2005 revealed a wealth of information regarding Venus' atmospheric properties (Titov et al., 2006; Drossart et al., 2007; Svedhem et al., 2007, 2009). The Spectroscopy for the investigation of the characteristics of the atmosphere of Venus (SPICAV) instrument on-board VEx had a suite of three spectrometers spanning the UV-IR wavelengths was designed to study of the atmosphere of Venus, from ground level to the outermost hydrogen corona at more than 40 000 km altitude (Bertaux et al., 2007; Korablev et al., 2012). Although it was originally not intended for spectro-polarimetric observations, its capability, through an Acousto-Optic Tunable Filter (AOTF), to record fluxes in two orthogonal orientations with respect to the spacecraft's reference axes meant that linear polarization component Stokes Q could be computed (Korablev et al., 2012). Rossi et al. (2015) by deriving the degree of polarization of reflected light from Venus at specific wavelength points between 650 nm and 1650 nm and neglecting absorption bands could derive key cloud and haze particle properties. Their results were in good agreement with previously obtained cloud properties by Knollenberg and Hunten (1979), Kawabata et al. (1980) and Knibbe et al. (1998). For lower latitudes they used the degree of polarization at λ = 1.101 and 1.274 μm and could deduce r_{eff} = 1.05 μm with a distribution of v_{eff} = 0.1 and n_r = 1.42. They found that degree of polarization increased dramatically towards the poles which could be attributed to the sub-micron sized particles. By using a r_{eff} of 0.25 μm and v_{eff} of 0.25 for a haze model particle distribution they could derive the upper limit on haze optical thickness at 1.101 μm and haze optical thickness of 0.17.

1.4. ATMOSPHERIC DYNAMICS

Despite the similarities in sizes and planetary compositions, Venus and Earth have taken very different paths when it comes to the planetary and atmospheric dynamics. The surface of Venus has a slow retrograde rotation period of about 243 Earth days while the upper cloud layer (~70 km) rotates 60 times faster with a period of 4 Earth days. Thus the upper atmosphere of Venus is in a state of "super-rotation" making the dynamics on Venus extremely interesting and unique to be closely studied. The dense atmosphere of Venus consists almost entirely of CO_2 and optically thick clouds of sulphuric acid extend between 30 and 80 km. Despite solar irradiance being 1.9 times that of Earth, approximately 80 % of the sunlight is reflected back. Clouds absorb a significant amount of this heat with a large variation of the radiative time constant from ~116 days (a Venusian solar day) at 40 km to ~0.5 days at 80 km which indicates a highly dynamic environment within these thick clouds (Sánchez-Lavega et al., 2017).

The wind fields on Venus have been measured through various in-situ and remote sensing means and have been shown to be more or less globally consistent vertically, with the speeds closer to the surface being weak ~2 m/s and increasing with altitude to ~100 m/s at 65 km (Schubert et al., 1980; Counselman et al., 1980; Limaye, 1985; CRISP et al., 1997). The zonal and meridional wind components at the upper cloud level show a strong dependence on local time that has been confirmed and verified through observations by long term Pioneer Venus OCPP instrument, Venus Express VMC and VIRTIS

instruments (Rossow et al., 1990; Limaye, 1988; Kouyama et al., 2013; Khatuntsev et al., 2013; Hueso et al., 2015). The zonal wind speeds increase by upto 5 - 15 m/s between 7h and 17h local time within the latitude bands 10° and 40°, accelerating towards the local afternoon. The meridional wind speeds increase by ~10 m/s between 14h - 16h in latitudes 40° - 50° that could be attributed to the combination of hadley cells and the thermal activity (Peralta et al., 2012; Sánchez-Lavega et al., 2017).

The upper atmosphere of Venus (> 90 km) exhibits a different regime of flow which is a combination of two different flow patterns: (1) a relatively stable subsolar-to-antisolar (SS-AS) circulation cell driven by solar (EUV-UV) and IR heating from the Sun, and (2) a retrograde superrotating zonal (RSZ) flow, which is in part a continuation of the RsZ flow at the cloud tops (Schubert et al. (2007)). This results in the divergence of the upwelling flow from sub-solar point to the evening terminator and also shifts the converging flow from further away from the morning terminator of the planet. The wind fields in this upper atmosphere of Venus is thus highly variable and complicated but various measurements have shown the zonal component to range from ~5 m/s to ~150 m/s and the SS-AS flow to range from ~40 m/s up to ~290 m/s (Limaye et al., 2013).

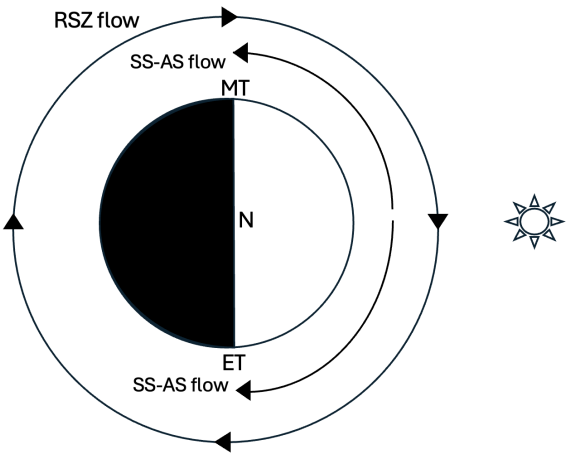

Figure 1.3: Circulation in the upper atmosphere (~90-200 km) of Venus. The diagram is oriented such that the viewer is looking down from above the planet's north pole, with the Sun's apparent motion proceeding counterclockwise. The north pole (N), morning terminator (MT), and evening terminator (ET) are labeled accordingly. The outermost circulation pattern depicted is the retrograde superrotating zonal (RSZ) flow, which moves in the clockwise direction. Superimposed on this is the subsolar-to-antisolar (SS–AS) flow, characterized by divergence near the subsolar point (dayside) and convergence near the antisolar point (nightside), driven by day-to-night thermal gradients (Schubert et al., 2007).

Waves play an important role in the atmospheric dynamics. Momentum transport from the waves is vital to the general circulation on Venus including the maintenance of super-rotation. A few types of commonly observed waves on Venus are gravity waves, Kelvin waves, Rossby waves and thermal tides with Kelvin waves and thermal tides being planetary scale waves and gravity waves being small scale waves. These waves have been observed through various methods both from ground and space. Gravity waves

ranging in wavelengths from 10 km to 300 km have been observed in visible, infrared and thermal images on Venus cloud tops (Markiewicz et al., 2007; Peralta et al., 2007a,b; Piccialli et al., 2014; Peralta et al., 2008; Fukuhara et al., 2017). These waves have been observed at various altitudes depending on the specific imaging technique and wavelength under consideration. Fluctuations in the vertical temperature profiles in the altitude range of 30 to 90 km derived using radio occultation techniques have been attributed to wave propagation (Jenkins et al., 1994; Hinson and Jenkins, 1995; Tellmann et al., 2012). Venus Express mission carried out an atmospheric drag experiment by measuring the acceleration/deceleration of the spacecraft through its thermosphere at an altitude between 130-140 km and detected thermospheric density waves with a quasi-5 day period (Müller-Wodarg et al., 2016).

Despite observations of various wave types through various means, several wave phenomena predicted in theory such as acoustic waves and Lamb waves remain unobserved (Petculescu and Lueptow, 2007). Numerical models predict gravity wave generation within the cloud layers because of the static instability close to 60 km altitude, which should grow in amplitude with altitude ultimately undergoing wave breaking resulting in non-linear wave interactions and generation of secondary waves. Such wave breaking has not been sufficiently observed yet (Sánchez-Lavega et al. (2017) and references therein). Momentum deposition by gravity wave activity is suspected to decelerate the SS-AS flow which would otherwise reach supersonic speeds (Seiff et al., 1980). Similarly dynamic modelling suggests that local time asymmetry because of the momentum deposition could explain the thermospheric super-rotation (Alexander, 1992; Zhang et al., 1996). Traditional imaging techniques might prove to be difficult to observe such waves because of the low density in upper cloud layers up to thermospheric altitudes and thus instrumentation capable of measuring sensitive fluctuations on Venus, such as polarimeters, might be needed to be able to observe and understand such wave activity (see Chapter 3).

1.5. VENUS AS AN EXOPLANET

With the discovery of Earth-sized planets orbiting other stars, there is a growing need to gain a deeper understanding of the planets in our own Solar System, particularly those that are similar to Earth and located in close proximity. While Venus is vastly different from Earth in terms of its potential to sustain life, Mars is considered an interesting target for habitability studies. However, when considering geological factors and the parameters commonly used in exoplanet studies, Venus emerges as the most Earth-like planet in our Solar System. One key indicator supporting this is Venus's elevated deuterium-to-hydrogen (D/H) ratio, which suggests the planet may have once harbored an ocean early in its evolutionary history (Donahue et al., 1982). Although early Mars may have had a favorable environment for life, its small size prevented it from sustaining such conditions. In contrast, Venus may have been capable of supporting a biosphere at some point in its past due to its similarities with Earth. Despite these similarities, Venus has not developed in the same way as Earth, prompting the question of why this is the case.

Exoplanet observation missions, like Transiting Exoplanet Survey Satellite (TESS) (Ricker et al., 2010), have identified several examples of terrestrial planets orbiting stars via the transit method. However, it remains unclear how many of these planets are sim-

ilar to Venus as opposed to being Earth-like. It is speculated that an atmospheric state akin to that of Venus is more stable and probable compared to Earth (Lincowski et al. 2018, and references therein). To distinguish between Earth and Venus-like planets, it is crucial to determine whether the planet is enveloped in clouds similar to those on Venus. Polarimetry holds promise as an effective tool to differentiate such planets as the degree of polarization of light reflected by the clouds on such planet is high. Polarimetry is a potent technique for characterizing exoplanets, owing to the fact that the variation in the degree of polarization with respect to the scattering angle is usually much more pronounced than that of the total flux (Hansen and Travis, 1974). This finding has been highlighted in various studies such as Seager et al. (2000); Stam et al. (2004); Stam (2008); Rossi et al. (2015), underscoring the significance of polarization measurements in providing insights into the nature and properties of exoplanetary atmospheres.

Although present day polarimetric instruments are not able to resolve Earth-like planets around other stars, measuring degree of polarization has some innate advantages. Since degree of polarization is a relative measure, it is well preserved irrespective of the planet-observer distance. This means that both the total and polarized fluxes experience equal attenuation before reaching an observer. Also since degree of polarization is a ratio, some of the instrument errors can be cancelled out. As shown by Stam (2008), degree of polarization shows strong variability over various surface and atmospheric conditions and can be crucial in distinguishing amongst clear, cloudy, vegetation or ocean covered planet. Recently, Trees and Stam (2022) have identified unique signatures (such as that caused by glint) in degree of polarization to identify oceans on Earth-like planets.

1.6. IMPORTANCE OF FUTURE VENUS MISSIONS

Given that Venus' evolutionary history is closely tied to that of Earth and given that it is likely for us to find Venus like uninhabitable planets around other stars, there has been a renewed interest in understanding Venus' evolutionary past in order to find unique markers to be able to identify false positives. Despite multiple missions to Venus in the past, we have barely started to understand this dynamic planet. Various observations including those obtained by the Magellan spacecraft indicate that Venus has been/currently is geologically active and has active volcanism (Wilson et al., 2022). The variability of SO_2 content in the clouds may indicate an active geological past on Venus (Esposito, 1984; Marcq et al., 2013). This could help us understand the mechanism behind the development and sustenance of the sulphuric acid clouds, the loss of water and the presence of other trace species in the atmosphere.

Venus has been assumed to have been Earth-like based on the approximate size and bulk density, but very little is known regarding its interior structure and dynamics. Evidence based on studying craters suggests that its surface is relatively young (within a billion years) but there could be regions that are older (Byrne and Krishnamoorthy, 2022). Reanalysis of Magellan data between two of its cycles has revealed that Venus is geologically active today (Herrick and Hensley, 2023). Despite this, we do not have sufficient evidence on whether such geological activity is episodic or is continuous in nature (Strom et al., 1994; Bjonnes et al., 2021; O'Rourke et al., 2014). This also ties back to the processes in the interior of Venus that would lead to such activity on a global scale. By studying the evolution of its surface and identifying and characterizing volcanic activity, several of

these questions that are important from an evolutionary aspect can be answered.

Several missions are set to explore Venus in the coming years to enable us answering these questions. ESA's EnVision will investigate Venus' geological and atmospheric mysteries with instruments like VenSAR, a synthetic aperture radar for detecting geological activity, and VenSpec, a suite of spectrometers to analyze the planet's composition and processes, including the monitoring of sulphured species and volcanic plumes (Ghail et al., 2017; Helbert et al., 2019; Lustrement et al., 2024; Neefs et al., 2024). NASA's VERITAS mission will map Venus' surface topography and composition using VISAR and VEM (Smrekar et al., 2022; Hensley et al., 2020; Helbert et al., 2022), while DAVINCI will study the planet's atmosphere and surface, with a probe making in-situ measurements during its descent in 2031 (Garvin et al., 2022). ISRO's Shukrayaan-1, will focus on Venus' atmosphere, surface, and mineral composition. Both EnVision and Shukrayaan-1 missions will be equipped with spectro-polarimeters—VenSpec-H and VASP, respectively—capable of measuring linearly polarized components. These instruments will enable precise characterization of Venus's clouds, haze, and trace gases, offering valuable insights into the dynamic processes shaping the planet's atmosphere.

1.7. OVERVIEW OF THIS THESIS

The objective of this research has been to understand the atmospheric properties of Venus' upper atmosphere by identifying unique polarization signatures associated with Venus' clouds using a polarized radiative transfer code capable of modeling the polarization properties of light reflected by Venus.

Chapter 2 of this thesis delves into two pivotal inquiries concerning Venus: can polarized light be utilized to observe atmospheric gravity waves on the planet? And what is the extent of gas density variation caused by these waves that can be detected by current spectro-polarimeters? Extensive research involving satellite missions and ground-based observations has established the presence of atmospheric gravity waves on Venus. These waves, responsible for transferring momentum from the lower to the upper atmosphere, play a vital role in Venus' dynamic atmospheric behavior. Detection methods employed thus far encompass visible and near-infrared imaging, as well as night-time airglow measurements and thermal imaging. In this study, particular emphasis is placed on investigating the sensitivity of atmospheric density fluctuations induced by gravity waves. To achieve this, an advanced atmospheric transport model is utilized to simulate the propagation of gravity waves originating from the Aphrodite Terra mountains on Venus.

Chapter 3 builds upon the findings presented in Chapter 2 while adopting a distinct approach. Ground-based observations of Venus have unveiled concentric rings in linear degree of polarization across the planet. We aim to investigate whether these polarized signals can be attributed to atmospheric gravity waves spanning the entire planet. Specifically, we explore whether density fluctuations in the upper atmosphere, potentially caused by gravity waves, can generate sufficient polarization in light to be detected by a ground-based imaging polarimeter mounted on a telescope. To achieve this, we employ a simplified forward model that assumes a proportional relationship between observed variations in polarized flux and density fluctuations. By approximating gas density profiles to the observed data, we estimate the approximate variation in the at-

mospheric gas density that could lead to the observed gravity wave variations.

Chapter 4 of this study aims to estimate the altitude of the cloud top on Venus utilizing measurements of polarized flux acquired by the SPICAV instrument on the Venus Express spacecraft (VEX) throughout its mission. In an atmosphere like that of Venus, where carbon dioxide (CO_2) is well-mixed, light scattered within the CO_2 absorption bands primarily originates from higher altitudes due to the increased gaseous absorption in the lower atmospheric layers. If a thick layer of clouds exists in the atmosphere, the scattered light becomes sensitive to their presence. Thus, by comparing the signal within the absorption bands to the continuum signal (which lacks absorption), valuable information regarding the height of the cloud deck can be extracted. Despite the SPICAV-IR instrument not being specifically calibrated for this purpose, we demonstrate that the degree of polarization obtained in CO_2 absorption bands can serve as a sensitive indicator of cloud presence. In this chapter, we make an initial effort to derive the altitude of the cloud top using these measurements, shedding light on the feasibility of this approach despite the instrument's original calibration and highlighting the importance of carrying polarization sensitive instruments for future Venus missions.

Chapter 5 focuses on the computation of both total and polarized fluxes reflected from a Venus-like planet, taking into account varying atmospheric conditions that could have evolved over time. The exploration for Earth-like exoplanets around distant stars may lead us to encounter Venus-like planets characterized by a dense cloud layer and a runaway greenhouse effect (Lustig-Yaeger et al., 2019b). Traditional methods relying on total reflected flux and transit spectroscopy face challenges in detecting cloud presence on such planets. Therefore, the utilization of polarimetry becomes crucial due to the significant degree of polarization imparted by spherical cloud droplets on Venus-like planets that could potentially be used to detect false-positives. This chapter aims to investigate the potential role of polarimetry in enhancing our ability to identify and characterize clouds on exoplanets, expanding our understanding of planetary atmospheres in diverse environments.

Chapter 6 presents a summary of the key findings from the previous chapters, along with concluding remarks. It also discusses the limitations of our findings and numerical models, offering suggestions for future improvements.

In summary, this thesis aims to develop a polarized radiative transfer code for modeling the polarization characteristics of light reflected by Venus. It investigates atmospheric gravity waves, their influence on polarization, and their potential significance for understanding Venus' atmospheric dynamics and detecting clouds on exoplanets.

2

POLARIMETRY AS A TOOL FOR OBSERVING OROGRAPHIC GRAVITY WAVES ON VENUS

GOURAV MAHAPATRA, MAXENCE LEFÈVRE, LOÏC ROSSI, AYMERIC SPIGA, DAPHNE M. STAM

Planet-wide stationary gravity waves have been observed with the thermal camera on the Akatsuki spacecraft. These waves have been attributed to the underlying surface topography and have successfully been reproduced using the Institut Pierre Simon Laplace (IPSL) Venus Mesoscale Model (VMM). Here, we use numerical radiative transfer computations of the total and polarized fluxes of the sunlight that is reflected by Venus under the conditions of these gravity waves to show that the waves could also be observed in polarimetric observations. To model the waves, we use the density perturbations computed by the IPSL VMM. We show the computed wave signatures in the polarization for nadir-viewing geometries observed by a spacecraft in orbit around Venus and as they could be observed using an Earth-based telescope. We find that the strength of the signatures of the atmospheric density waves in the degree of polarization of the reflected sunlight depends not only on the density variations themselves, but also on the wavelength and the cloud top altitude. Observations of such wave signatures on the dayside of the planet would give insight into the occurrence of the waves and possibly into the conditions that govern their onset and development. The computed change in degree of polarization due to these atmospheric density waves is about 1000 ppm at a wavelength of 300 nm. This signal is large enough for an accurate polarimeter to detect.

Parts of this chapter have been published in the Planetary Science Journal **2**, 3 (2021) Mahapatra et al. (2021).

2.1. INTRODUCTION

Gravity waves are thought to play a key role in the transfer of energy and momentum from the lower to the upper parts of Venus' atmosphere, and through that would influence the super-rotation in the atmosphere (Hou and Farrell, 1987; Peralta et al., 2008). Multiple and different types of observations have shown that the upper atmosphere of Venus carries various types of gravity waves (Kasprzak et al., 1988; Piccialli et al., 2014; Peralta et al., 2017). Some wave patterns were found in images of the clouds (Markiewicz et al., 2007; Peralta et al., 2008; Piccialli et al., 2014; Peralta et al., 2020), and others revealed their presence through the variations they leave in the local temperatures. In particular, JAXA's Akatsuki spacecraft's Longwave Infrared Camera (LIR) observed huge waves covering the planet almost from the southern to the northern poles (Fukuhara et al., 2017) on 7th December, 2015, just five hours after the spacecraft's orbital insertion. These waves and the associated local density variations are what we focus on in this paper.

First in-situ measurements of variations in the local temperatures and wind profiles that were attributed to atmospheric waves were done by the Pioneer Venus orbiter (Seiff et al., 1985). In particular, the Orbiter Neutral Mass Spectrometer (ONMS) measured variations in gas density in the upper atmosphere (Kasprzak et al., 1988) and during the aerodynamic drag experiments that were performed in the last orbits of ESA's Venus Express mission, wave-like perturbations were detected in the thermosphere (Müller-Wodarg et al., 2016).

Small-scale (< 100 km) waves in Venus' atmosphere have been studied with a turbulent-resolving numerical model that included a convective layer within the clouds (Lefèvre et al., 2018, 2017; Imamura et al., 2014). The formation of this planet-wide wave observed by the Akatsuki spacecraft was attributed to the underlying mountainous Aphrodite Terra region (Fukuhara et al., 2017; Kouyama et al., 2017; Lefèvre et al., 2020), see Fig. 2.1. Anomalies at the cloud tops that appeared to be associated with mountain waves were observed above the Beta Regio area with the IR2 instrument (2.02 μm wavelength, Satoh et al., 2017) and above Aphrodite Terra, Atla, and Beta Regio with the UV imager on the Akatsuki spacecraft (Kitahara et al., 2019). Indeed, stationary waves above the main topographical features on Venus' southern hemisphere were also detected by VIRTIS on the Venus Express mission (Peralta et al., 2017).

The mountain waves' dynamics was studied using limited-area mesoscale numerical modeling by Lefèvre et al. (2020). The modeling shows that these waves are generated by the interaction between the wind flow and the topography with a peak of activity in the late afternoon controlled by the atmospheric stability. The waves propagate vertically to the cloud tops. At the cloud tops, the waves can perturb the local cloud altitudes by as much as 600 m and the local temperatures by ±2 K. Temperature anomalies larger than 0.5 K can remain present for about 10 Earth days (Lefèvre et al., 2020; Kouyama et al., 2017). The waves transport upward heat and momentum that affect the circulation and even the length of the Venus day as was demonstrated by global climate modeling (Navarro et al., 2018). It is clear that observing and characterizing these waves is crucial for better understanding of Venus' current atmosphere as well as its evolution.

In this paper, we study the use of reflected sunlight and in particular polarimetry, i.e. the measurement of the state of polarization of light, for the detection and charac-

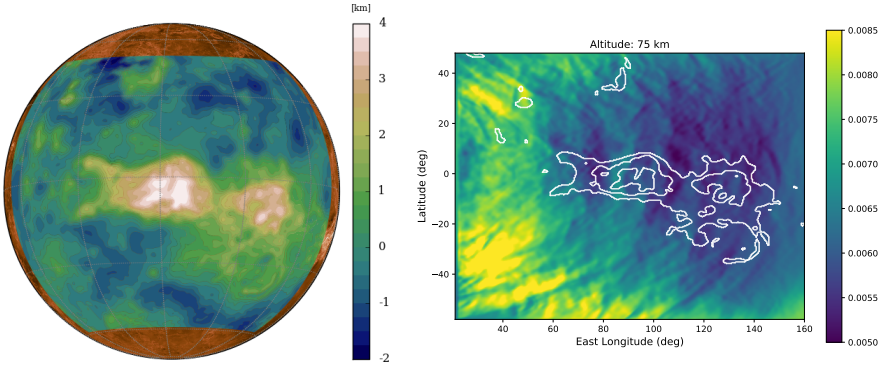

Figure 2.1: The elevation (in km) of the Aphrodite Terra region mapped on the Venus sphere (on the left), and the corresponding computed pressure map (in atm) at an altitude of 75 km, with Aphrodite Terra outlined in white (on the right). The pressure contours have been derived from isopotential temperature surface fields Lefèvre et al. (2020). The area covered (on the right) spans 108° in latitude and 144° in longitude. The orographic wave peaks above the Aphrodite Terra pressure map (on the right) at 80° East longitude.

terization of these gravity waves. Polarimetry has been successfully used to determine Venus' cloud particle refractive index, size distribution, cloud top altitude and the nature of overlying haze particles (Hansen and Hovenier, 1974; Kawabata et al., 1980; Knibbe et al., 1995; Braak et al., 2002; Rossi et al., 2015). The state of polarization of this light is sensitive to the optical properties of the particles that scatter the light, the scattering angle, and the number of times that the light is scattered. In particular, light that has been scattered by gaseous molecules can have a high degree of (linear) polarization (Hansen and Travis, 1974), depending on the scattering angle. Because the gravity waves such as the ones observed by the Akatsuki spacecraft (Fukuhara et al., 2017) are in essence density variations in the atmospheric gas (Lefèvre et al., 2020), these waves are expected to cause a variation in the state of polarization of the reflected light. We present results of computations of the total and polarized fluxes and the degree of polarization of the sunlight that is reflected by Venus in the presence of these gravity waves as computed with the Venus Mesoscale Model (VMM) (Lefèvre et al., 2020).

The outline of this paper is as follows. In Sect. 2.2, we describe our numerical method, including the properties of our model atmosphere and our use of the numerical results of the VMM, i.e. the local atmospheric density variations due to the gravity waves. In Sect. 4.3, we present and discuss our numerical results. Section 4.5, finally, contains a summary and our conclusions.

2.2. Description of the numerical method

2.2.1. DEFINITIONS OF FLUXES AND POLARIZATION

Our aim is to compute the total and linearly polarized fluxes of sunlight that is reflected by Venus when gravity waves travel through its atmosphere. We describe the total and polarized fluxes of light with the following Stokes (column) vector **F** (see Hansen and Travis, 1974)

$$\mathbf{F} = \left[F, Q, U, V\right], \tag{2.1}$$

with F the total flux, Q and U the linearly polarized fluxes, and V the circularly polarized flux. In general, the Stokes vector elements depend on the wavelength λ. Element V of sunlight that is reflected by Venus is very small, and varies within a few tens of ppm depending on the atmosphere and observation geometry (Kemp et al., 1971; Kawata, 1978; Rossi and Stam, 2018).

We assume that the sunlight that is incident on Venus is unidirectional and unpolarized (e.g. Kemp et al., 1987), such that $\mathbf{F}_0 = F_0[1,0,0,0] = F_0\mathbf{1}$, with πF_0 the total incident solar flux measured perpendicularly to the direction of propagation of the light. Thus the reflected fluxes shown here are normalized fluxes and the actual values can be obtained in a straightforward manner by scaling them to the actual value of incoming sunlight in W/m^2 on Venus.

The linearly polarized fluxes Q and U of the reflected sunlight are defined with respect to a reference plane. We perform our model calculations for local reflected light with a nadir viewing direction and a few solar zenith angles, as could be observed by a spacecraft orbiting Venus, and for a distant view as would be observable with an Earth-based telescope. In our computations of locally reflected light, the reference plane is the local meridian plane, i.e. the vertical plane containing the local zenith direction and the direction to the observer. In our computations of light reflected by Venus as a whole as observable with an Earth-based telescope, the reference plane is the planetary scattering plane, i.e. the plane containing the centers of the Sun, Venus, and the Earth.

The degree of (linear) polarization of the reflected light is, in general, defined as the ratio of (linearly) polarized fluxes to the total flux, as follows:

$$P = \sqrt{Q^2 + U^2}/F. \tag{2.2}$$

For the results with the local viewing geometry, however, the illumination and viewing geometries in combination with our choice of reference plane are such that the linearly polarized flux U is always zero. We therefore use a definition of the degree of polarization that includes information about the direction of polarization in this case:

$$P_S = -Q/F. \tag{2.3}$$

If $P_S > 0$ ($P_S < 0$), the light is polarized perpendicular (parallel) to the reference plane.

2.2.2. OPTICAL PROPERTIES OF THE MODEL ATMOSPHERE

The model atmosphere of Venus is composed of a stack of 71 horizontally homogeneous layers that contain gas and, optionally, cloud or haze particles. The optical properties

of each of the layers are described by the layer's optical thickness b, the single scattering albedo, and the single scattering matrix $\mathbf{S}$ of the particles in the layer. The atmosphere is bounded below by a horizontally homogeneous surface, which we assume to be black (because of the large optical thickness of the clouds, the actual value of the surface albedo is irrelevant).

The total optical thickness b of an atmospheric layer at wavelength λ is given by the sum of the layer's gaseous optical thickness, b^{m}, and the layer's aerosol (i.e. cloud or haze) optical thickness, b^{a}, as follows

$$b(\lambda) = b^{\mathrm{m}}(\lambda) + b^{\mathrm{a}}(\lambda). \tag{2.4}$$

The layers of our model atmosphere all contain pure carbon-dioxide (CO_2) gas. For our radiative transfer computations, we use wavelengths where CO_2 does not have any significant absorption; the single scattering albedo of the gas, is thus 1.0. The gas optical thickness, b^{m}, of an atmospheric layer is computed as

$$b^{\mathrm{m}}(\lambda) = N^{\mathrm{m}}\sigma^{\mathrm{m}}(\lambda), \tag{2.5}$$

with N^{m} the layer's gaseous column number density (in m^{-2}), and σ^{m} the scattering cross–section of the gas molecules (in m^2) which is given by (see e.g. Stam et al., 1999)

$$\sigma^{\mathrm{m}}(\lambda) = \frac{24\pi^3}{N_{\mathrm{L}}^2}\frac{1}{\lambda^4}\frac{(n^2(\lambda)-1)^2}{(n^2(\lambda)+2)^2}\frac{6+3\delta(\lambda)}{6-7\delta(\lambda)}, \tag{2.6}$$

with N_{L} Loschmidt's number, n the refractive index of CO_2 under standard conditions, and δ the depolarization factor of CO_2. For both n and δ, we use the wavelength dependent values of Sneep and Ubachs (2005). Assuming hydrostatic equilibrium, a layer's gas column number density N^{m} is computed according to

$$N^{\mathrm{m}} = N_{\mathrm{A}}\frac{p_{\mathrm{bot}} - p_{\mathrm{top}}}{mg}, \tag{2.7}$$

with N_{A} Avogadro's number, p_{bot} and p_{top} the pressures at the bottom and the top of the atmospheric layer, respectively, m the average molar mass of the gas, i.e. 44.01 g/mol for CO_2, g the acceleration of gravity, which we assume to be altitude independent and equal to 8.87 $\mathrm{m/s}^2$. Figure 2.3 shows the standard (i.e. unperturbed by a gravity wave) pressure and temperature profiles across our model atmosphere (Seiff et al., 1985) and the geometrical thickness of the atmospheric layers. Note that the total and polarized fluxes of the light that is reflected by Venus are virtually insensitive to the atmospheric composition and density below the main cloud deck, thus below 40-50 km.

The gravity waves cause variations in the local atmospheric pressure, and hence in the local gas density and the gas optical thickness b^{m} of the atmospheric layers through which the wave travels. We compute the local variations in b^{m} of the whole range (0 - 100 km) of the atmosphere using the local pressure variations resulting from the gravity wave model computations described by Lefèvre et al. (2020). They used the Institut Pierre Simon Laplace (IPSL) Venus Mesoscale Model (VMM) to simulate the orographic wave that was observed 15° west of Venus' Aphrodite Terra region by the Akatsuki spacecraft (Fukuhara et al., 2017; Kouyama et al., 2017).

In the VMM, the non-hydrostatic WRF dynamical core (Skamarock and Klemp, 2008) is coupled with the radiative transfer code of the IPSL Venus General Circulation Model (GCM) (Lebonnois et al., 2015) to compute the solar heating and the thermal radiation field of the atmosphere. Furthermore, the latitudinal varying cloud model of Haus et al. (2014, 2015) is implemented. The initial and horizontal boundary conditions are determined by the GCM (Garate-Lopez and Lebonnois, 2018), which is updated every 1/100 Venus day, thus about every 28 Earth hours. Lefèvre et al. (2020) computed the wave over Aphrodite Terre with a spatial resolution of 40 × 40 km^2 and 300 levels in the vertical direction.

Lefèvre et al. (2020) found that the isopotential temperature can be used as a tracer for the deformation of the cloud top by waves. Thus, by choosing one value for isopotential temperature, corresponding temperature and pressure maps can be reconstructed. We use the pressure values corresponding to isopotential temperature maps over Aphrodite Terra in the radiative transfer computations. Figure 2.1 illustrates the local pressure variations with isopotential temperature due to the wave over Aphrodite Terra region at an altitude of 75 km. Note that at low altitudes, the pressure variations follow the topography of the underlying Aphrodite Terra area and at higher altitudes, such as at 75 km, the variations are due to the orographic waves. Figure 2.2 shows the map of b^{m}, as perturbed due to the gravity wave over the Aphrodite Terra region (cf. Fig. 2.1) computed for the whole atmosphere and for the atmosphere above 75 km. In the latter, the density wave is clearly visible. The maximum change in pressure from the wave perturbation occurs at 80° longitude.

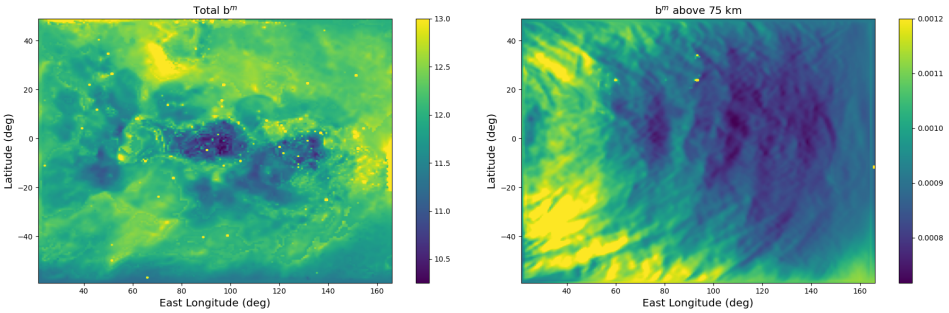

Figure 2.2: Left: The total gas optical thickness b^{m} of the Venus atmosphere. Right: The gas optical thickness of the atmosphere above 75 km. These optical thicknesses pertain to $\lambda = 600$ nm, and have been calculated for an afternoon pressure map of the Aphrodite Terra region (Lefèvre et al., 2020), as shown in Fig. 2.1.

In Fig. 2.4, our cloud and haze vertical profiles can be seen. The aerosol (i.e. cloud or haze) optical thickness b^{a} has been adapted from in-situ measurements by Knollenberg and Hunten (1980). For the cloud and haze b^{a} is 30 and 0.1, respectively. In principle, these optical thicknesses depend (somewhat) on the wavelength, but we keep them constant for this investigation. Both the cloud and haze particle densities decrease exponentially with altitude with a scale height of 4 km (see Fig. 2.4). We define the cloud top altitude as the altitude at which the cloud optical thickness equals 1.0 measured from the top of the atmosphere (ignoring the haze).

The cloud and haze particles are assumed to be spherical, with their sizes described by a log-normal size distribution (Hansen and Travis, 1974) with a modal radius r_g and a variance σ. Following Pollack et al. (1980) and Fedorova et al. (2016), we use $r_g = 1.05$ μm and $\sigma = 1.21$ for the cloud particles, and $r_g = 0.15$ μm and $\sigma = 1.91$ for the haze particles which is derived from the observations of cloud particle size-distribution by the LCPS instrument on-board the Pioneer Venus mission (Knollenberg and Hunten, 1980). For the refractive index of both the cloud and haze particles, we use values that are wavelength dependent and representative for 75% sulphuric acid solution (Palmer and Williams, 1975). We compute the optical properties of the cloud and haze particles, i.e. their scattering cross-section and single scattering matrix, using the Mie-algorithm as described by De Rooij and Van der Stap (1984). To account for the absorption by the cloud and haze particles at $\lambda = 300$ nm, we take a non-zero value for the imaginary part of the refractive index, $n_i = 0.0007$ which yields a planet spherical albedo of 0.4 (Pollack et al., 1980). The planet spherical albedo was accounted for using the similarity relation described in Hansen and Hovenier (1974) and which was also applied by Bailey et al. (2018) for their polarized flux computations of Venus. At $\lambda = 600$ nm and 900 nm, the imaginary part of the refractive index equals zero and the single scattering albedo of the cloud and haze particles is thus one. At 300 nm, the single scattering albedo of the cloud and haze particles is ~0.972. Figure 2.5 shows the phase function (i.e. the scattered flux) and degree of polarization of incident unpolarized light that is singly scattered by the cloud and haze particles at the wavelengths of our interest.

The single scattering matrix of the scatterers in the layer is computed using

$$\mathbf{S}(\lambda) = \frac{b^{\mathrm{m}}(\lambda)\mathbf{S}^{\mathrm{m}}(\lambda) + b^{\mathrm{a}}_{\mathrm{sca}}(\lambda)\mathbf{S}^{\mathrm{a}}(\lambda)}{b(\lambda)}, \tag{2.8}$$

with $\mathbf{S}^{\mathrm{m}}$ the single scattering matrix of the gas, for which we use the anisotropic Rayleigh scattering matrix as described by Hansen and Travis (1974), and $\mathbf{S}^{\mathrm{a}}$ the single scattering matrix of the aerosol, i.e. the cloud or haze particles. $b^{\mathrm{a}}_{\mathrm{sca}}(\lambda)$ is the wavelength dependent aerosol scattering optical thickness.

2.2.3. The radiative transfer algorithm

The reflected flux vector F (Eq. 3.1) depends strongly on the illumination and viewing geometries, apart from the optical properties of the model atmosphere. These geometries are defined with the following angles: θ_0, the angle between the local zenith and the direction to the Sun, θ, the angle between the local zenith and the direction to the observer, and ϕ, the azimuthal angle between the direction of propagation of the incident light and the direction towards the observer. Since our plane-parallel model atmosphere is rotationally symmetric around the local vertical, only the difference between the azimuthal directions of the incident and the reflected light ($\phi - \phi_0$) is relevant.

We use an efficient adding-doubling algorithm (de Haan et al., 1987) to compute the light that is reflected by Venus. The algorithm fully accounts for polarization in all orders of scattering. We used the PyMieDAP code (Rossi et al., 2018) which is an open-source version of the adding-doubling algorithm. For our computations of locally reflected light, we use a nadir-viewing geometry, thus with $\theta = 0°$, and vary θ_0 between 0° and 90° ($\phi - \phi_0$ is thus undefined and set equal to 0°). For our computations for Earth-

based Venus observations, we use the planetary phase angle α, measured between the Sun and the Earth from the center of Venus ($0^\circ \leq \alpha \leq 180^\circ$), to describe the illumination and viewing geometries of the planet. We use 80 Gaussian quadrature points for interpolating between sub-grid geometries in all of our computations.

2.3. RESULTS

2.3.1. SENSITIVITY OF F, Q, AND P_S TO THE TOTAL GAS OPTICAL THICKNESS

Before discussing the signatures of gas density variations due to gravity waves in reflected sunlight, we discuss how the total and polarized fluxes F and Q, and the degree of polarization P_S depend on the gas optical thickness b^m. The top row in Fig. 2.6 shows the dependence of F, Q, and P_S on b^m above a white, Lambertian reflecting surface. We use this surface instead of an aerosol layer to avoid introducing angular effects due to the scattering of light by the cloud and haze particles. These effects have been included in the bottom row of Fig. 2.6, where a thick cloud layer replaces the white surface. The solar zenith angle θ_0 ranges from 0° and 90°, and the viewing zenith angle θ is zero (nadir view, thus U equals zero). Note that b^m above 65 km in the unperturbed atmosphere is about 0.01 at $\lambda = 600$ nm.

From Fig. 2.6, it can be seen that with a white surface instead of a cloud, and for $\theta_0 \lessapprox 50°$, total flux F increases with increasing b^m because of the increase in scattering in the atmosphere in combination with the short path-length through the atmosphere and the white surface. For larger θ_0, F decreases with increasing b^m both because the incident flux decreases (measured parallel to the atmosphere) and because the contribution of the surface reflection decreases. When b^m is approximately larger than 10, F has reached its asymptotic value and is virtually constant for a given value of θ_0. Without a cloud, Q is negative for all θ_0 and b^m, because the only scatterers are gas molecules. For small b^m, Q is close to zero because of the unpolarized surface reflection. With increasing b^m, $|Q|$ increases due to the increased scattering by the gas, except for the smallest values of θ_0, where the single scattering P_S is very small (see Fig. 2.5). Like F, Q reaches an asymptotic value when $b^m \gtrapprox 10$. Degree of polarization P_S increases with b^m, except for the smallest θ_0, where $P \approx 0$, because $|Q| \approx 0$.

With a thick cloud instead of a white surface (the bottom row of Fig. 2.6), F, Q, and P_S are strongly influenced by scattering in the cloud, especially when b^m and θ_0 are small. In particular, for $0.1 \lessapprox b^m \lessapprox 1$ and $\theta_0 \gtrapprox 20°$, F, Q, and P_S appear to be insensitive to b^m because they are mostly determined by the scattering by the cloud particles. For larger values of b^m, F, Q, and P_S tend to their values with the white surface instead of the cloud underneath the atmosphere. When $\theta_0 \approx 15°$, F, Q, and P_S all show the glory. This feature is also prominent in the single scattering curves of the cloud particles (Fig. 2.5) and is thought to be due to interference of EM-waves that traveled across the surface of the spherical particles (for an in-depth discussion of this optical feature, see Laven, 2005). The detection of the glory has been well documented on Venus (see Lee et al., 2017; Satoh et al., 2015; Rossi et al., 2015; Petrova et al., 2015; García Muñoz et al., 2014; Hansen and Hovenier, 1974).

2.3.2. SENSITIVITY OF F, Q, AND P_S TO THE VERTICAL DISTRIBUTION OF THE GAS OPTICAL THICKNESS

The amplitude of a density perturbation caused by an atmospheric gravity wave increases exponentially with altitude (Fritts and Alexander, 2003). We have performed a sensitivity study into the influence of the altitude of a density variation on F, Q, and P_S,

by increasing the gas density, and hence the gas optical thickness, of single atmospheric layers by 1% in 2 km thick layers between 60 and 90 km (above 90 km, the gas density is too small to leave any effect) and by computing the resulting F, Q, and P_S of the reflected light. At 60 km (90 km), the unperturbed gas density is 0.47 kg/m^3 (0.00114 kg/m^3) and we thus increase it to 0.4747 kg/m^3 (0.00115 kg/m^3). The viewing angle θ is 0°, like before.

Figure 2.7 shows the relative differences in F, Q, and P_S due to the 1% gas density increases in single atmospheric layers for three different cloud top altitudes. It can be seen that a density increase in the lower atmospheric layers generally has a larger influence on F, Q, and P_S, when the cloud top is lower. The reason is that with a lower cloud top altitude, the upper atmospheric layers contain less cloud particles, and the contribution of scattering by gas molecules is larger. When $\theta_0 \lessapprox 40°$, increasing the density decreases F of the reflected light (at $\theta = 0°$), except when the cloud top is high and the density increase is in the lower atmospheric layers (the top row of Fig. 2.7). Polarized flux Q increases with increasing density when θ_0 is smaller than about 25° (except when $\theta_0 \approx 0°$, where Q is virtually zero), and Q decreases with increasing density when $\theta_0 \gtrapprox 25°$. Degree of polarization P_S decreases where Q increases. The change in P_S is largest for the largest values of θ_0.

2.3.3. F, Q, AND P_S ACROSS APHRODITE TERRA

Here we present F, Q, and P_S of the reflected sunlight as computed across Aphrodite Terra, using the density waves shown in Fig. 2.2. Figure 2.8 shows longitudinal cross–sections pertaining to the latitude 0° for $\theta_0 = 30°$ and 60°, respectively, and for cloud top altitudes of 75 km, 70 km, and 65 km. Viewing zenith angle θ is, as before, 0°. As can be seen, for a given cloud top altitude and θ_0, the patterns of F and Q, and P_S are not correlated with wave structure across the latitude. This is due to the altitude dependence of the sensitivity of F and Q to density variations (cf. Fig. 2.7). In particular, F shows smaller scale wave features than Q and P_S, which are caused by the horizontal altitude variations of the underlying surface (cf. Fig. 2.10). The pattern of P_S appears to be the inverse of that of Q which is a consequence of the negative sign introduced in Eq. 2.3. Recall that, positive P_S denotes polarization perpendicular to the reference plane. Changing the cloud top altitude changes F, but not the general pattern variation with longitude. The influence of the cloud top altitude is stronger on Q than on F: the overall shape of the curves changes significantly with changing cloud top altitude, and, while some peaks and dips appear to be relatively insensitive to the cloud top altitude, their strengths with respect to other features change. The anti-correlation between F and Q increases with decreasing cloud top altitude caused by the reflected light from density waves deeper in the atmosphere. The P_S curves behave similarly as those of Q.

In Fig. 2.9, the background continuum of the $\theta_0 = 60°$ curves in Fig. 2.8 has been removed to better view the variations. For each data point, the background continuum was computed by averaging the 12 surrounding data-points or equivalently across 4.2° of longitude. Apart from the curves for 300 nm, we have added those for wavelengths 600 nm and 900 nm. It can be seen that the variations in Q and P_S are largest at 300 nm, and smallest at 900 nm. This is due to the $1/\lambda^4$ dependence of the Rayleigh scattering cross–section, see Eq. 2.6 and Fig. 2.6: with increasing λ for a given gas density, $b^{\mathrm{m}}_{\mathrm{sca}}$

decreases, and hence $|Q|$ and P_S decrease. For F, the variations are largest at 600 nm, and smallest at 300 nm. This is due to an interplay between the scattering by gas (F decreases with increasing λ), clouds (F increases with increasing λ) and the observational geometry. Figure 2.9 also shows that the variations in Q and P_S increase with decreasing cloud top altitude (cf. Fig. 2.7). In particular, the variations in P_S are on the order of 100 ppm for the highest clouds shown here, and a few times larger for the lowest clouds. The variations in F appear to be independent of the cloud top altitude.

Figure 2.10 shows F, Q, and P_S across the Aphrodite Terra region for three values of θ_0. Here, $\lambda = 300$ nm, where the variations in Q and P_S are largest (cf. Fig. 2.9), and the cloud top is at 65 km. The maps of F for the different θ_0 show different patterns: in particular, with increasing θ_0, the surface features become less apparent as the scattering in the atmosphere increases. The patterns across the maps of Q show hardly any dependence on θ_0, apart from the absolute values: with increasing θ_0, the single scattering angle increases, and $|Q|$ of the light scattered by the gas molecules increases (see Fig. 2.5). The maps of Q also reveal the wave pattern clearer than F, while the underlying topography is indistinguishable, because Q originates from higher altitudes than F. The maps of P_S are similar to those of Q. As we have seen before in Fig. 2.9, the strength of the variations in Q and P_S increases with θ_0. Figure 2.11 shows P_S at $\theta_0 = 60^\circ$ from Fig. 2.10 with the background signal removed. We used two different Gaussian background removal filters: a high-pass filter and a low-pass filter. The high-pass filter has a $\sigma = 15$ and low-pass filter has $\sigma = 3$. The choice of filter affects the substructure in the wave pattern in P_S, but does not change the absolute change in P_S.

Figures 2.7-2.11 showed the reflected light signals for a local viewing geometry with the local viewing angle fixed to nadir view ($\theta = 0$) and a constant solar zenith angle. We use a constant viewing geometry across each map so as to determine the contribution of the signal due to the waves. Figure 2.12 shows the signals as they would be observable from Earth (e.g. from an Earth-orbiting telescope or from the ground) for three planetary phase angles α. Here, the local solar zenith and viewing angles thus depend on the location on the planetary disk. Please note that here we add the contribution of U (which is generally non-zero for the planet-wide view) in calculating our degree of polarization P and thus use the formula in Eq. 2.2. Figure 2.13 is similar to Fig. 2.12 except with the background removed with a Gaussian filter with $\sigma = 3$. Note that these computations do not include turbulence in the Earth's atmosphere, which would decrease the spatial resolution when observing the planet with a ground-based telescope.

In Fig. 2.12, hardly any wave-like patterns are visible. The main variations in F, Q, and P are smooth and due to the variation of the illumination and viewing angles across the disk. In Fig. 2.13, Q and especially P do show patterns due to the density variations of the gravity wave. The pattern strength increases with increasing α, as the average θ_0, across the planetary disk increases and the average single scattering angle thus decreases (cf. Fig. 2.10).

2.4. SUMMARY AND CONCLUSIONS

We have used pressure variations due to atmospheric gravity waves as computed by the Venus Mesoscale Model VMM (Lefèvre et al., 2020), which successfully simulated waves over Venus' Aphrodite Terra region as observed at IR wavelengths by JAXA's Akatsuki spacecraft (Fukuhara et al., 2017; Kouyama et al., 2017), to investigate the use of reflected sunlight observations for the detection of such waves. Waves in the upper, tenuous part of the Venus atmosphere (~70 km) will escape methods such as IR observations, that were successful in detecting waves in the lower, denser parts of Venus' atmosphere. Observations of reflected sunlight will also allow detecting the waves on Venus' day-side, which would help understanding the atmospheric conditions that trigger their appearance.

Our numerical simulations indicate that the (linearly) polarized flux and the degree of polarization P of sunlight that is reflected by Venus are indeed sensitive to variations in the gas density, and through that to variations of gas optical thickness b^{m} above the Venusian clouds, while the total flux F is more sensitive to the properties of the clouds themselves. The polarized flux increases with increasing atmospheric gas density above the clouds as more light is scattered by gas molecules, except for geometries where the light that has been singly scattered, has a very low degree of polarization, such as when the sun is overhead for a nadir looking instrument on a spacecraft orbiting or flying past Venus. The degree of polarization P of the reflected sunlight shows a similar behavior as the polarized flux: P increases with increasing gas optical thickness b^{m}, except in the back-scattering direction because there the single scattering P equals zero.

For a nadir viewing mode, the variations in F, Q (U equals zero in our geometries) and P_{S} increase with increasing solar zenith angle, as the gas density along the optical path increases. Varying the vertical location of the gas density variations, shows that F appears to be slightly more sensitive to waves in deeper atmospheric layers than Q and P_{S}.

The variations in F, Q, and P_{S} decrease with increasing wavelength. This is not surprising since the Rayleigh scattering cross–section of the gaseous molecules also decreases with increasing wavelength. At 300 nm, variations in F are in the order of a few 100 ppm, in $|Q|$ in the order of 50 ppm, and in P_{S} in the order of 500 ppm. The variations in Q and P_{S} at 300 nm are a factor of about 10 stronger than at 600 nm and a factor of about 100 stronger than at 900 nm. In F, the variations at 300 nm are about twice as strong as those at 600 nm, and about four times as strong as those at 900 nm. Observations at shorter wavelengths would thus be better suited for detecting these waves.

For our simulations, we assumed a constant cloud top altitude across each scene on the planet. In reality, the Venusian clouds show spatial variability (Sato et al., 2020; Fedorova et al., 2016): average cloud top altitudes decrease with increasing latitude, ranging between 75 to 65 km. Our results show that the strength of the wave variations in the polarized flux and degree of polarization increases with decreasing cloud top altitude (see Fig. 2.9). When the cloud top altitude would vary across an observed scene, the strength of the observed variations would thus also depend on the variations in the cloud top altitude. Distinguishing the variations due to gas density variations from those due to cloud top variations would be possible when the density wave moves with respect to the underlying clouds as the typical wind speeds range from 100 to 350 km/h near

the cloud tops (Sánchez-Lavega et al., 2017; Horinouchi et al., 2018; Garate-Lopez and Lebonnois, 2018).

We based our analysis of orographic gravity waves over the Aphrodite Terra region as observed by Akatsuki (Fukuhara et al., 2017; Kouyama et al., 2017) and modeled by Lefèvre et al. (2020). The scope of our analysis extends to gas density variations due to other types of atmospheric waves. For example, the Pioneer Venus ONMS instrument observed wave-like density fluctuations in Venus' thermosphere that were linked to the vertical propagation of inertial gravity waves (Kasprzak et al., 1988). Venus Express's Aerobreaking Drag Experiment registered local density perturbations (Müller-Wodarg et al., 2016) in Venus' uppermost atmosphere in an altitude region of 130 - 200 km. Although the density variations would be too small to yield measurable signal variations (see Fig. 2.7) at those high altitudes, polarimetry being sensitive to upper atmospheric variations, could possibly be a powerful tool to detect them in the future, and to provide more information about them.

Our computations of flux and polarization signals across the disk of Venus due to the waves at different planetary phase angles (Fig. 2.13) show variations in P on the order of 100 ppm at intermediate to large phase angles (60° - 80° in Fig. 2.13). Such variations are achievable with modern day polarimeters on Earth-based telescopes, despite the fact that Earth's atmosphere introduces some spatial blurring. One such example of a highly sensitive instrument is the experimental ExPo instrument that had a polarimetric signal sensitivity better than 100 ppm (Rodenhuis et al., 2008).

Of course, Venus is not the only planet with gravity waves traveling through its atmosphere. Many detections of such waves in the Earth's atmosphere have been reported (Gong et al., 2015; Chou et al., 2017), and high precision polarimetry from an Earth-orbiting satellite could help to further characterize such waves on the dayside.

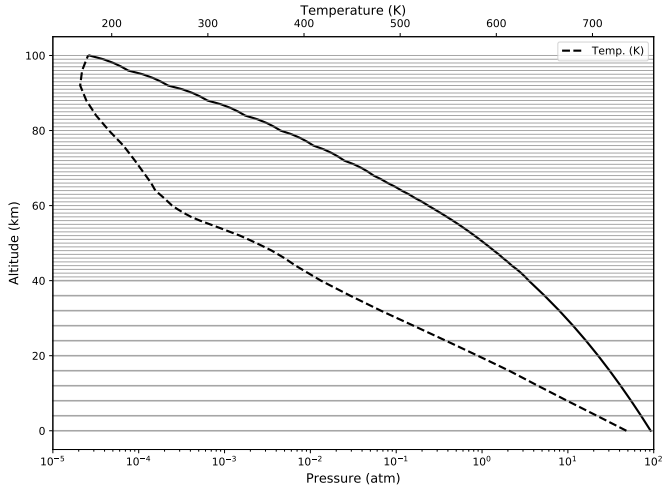

Figure 2.3: The vertical profiles of the pressure (solid line) and the temperature (dashed line) across our unperturbed Venus model atmosphere (Seiff et al., 1985), with the horizontal lines indicating the geometrical thicknesses of the layers, i.e. 4 km below and 1 km above 40 km altitude.

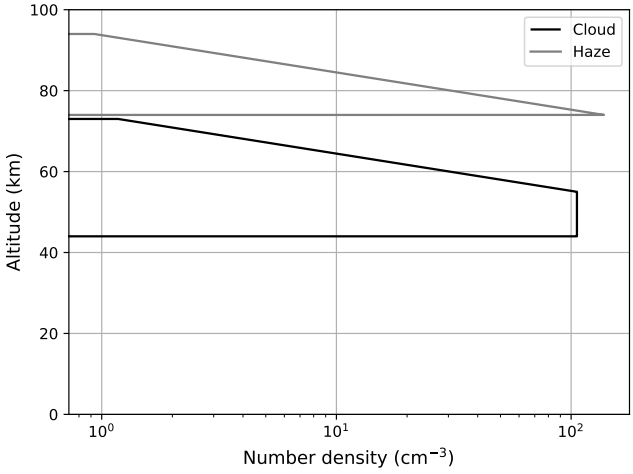

Figure 2.4: A sample vertical distribution of the cloud and haze particles. Both the cloud and the haze have a scale height H of 4 km. The (wavelength independent) optical thicknesses of the cloud and the haze are 30 and 0.1, respectively.

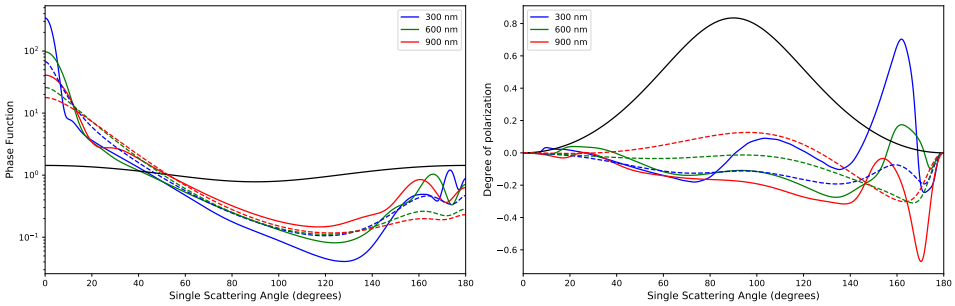

Figure 2.5: The phase function (left) and degree of polarization (right) of incident unpolarized light that is singly scattered by the cloud particles (solid, colored lines), haze particles (dashed, colored lines), and the gaseous molecules (solid black lines) at three wavelengths. Note that the wavelength dependence of the molecular scattering (through depolarization factor δ) is so small that we show only one line. All particles are distributed in size according to a log-normal distribution. The phase functions have been normalized such that averaged over all scattering directions they equal 1.0 (see Hansen and Travis, 1974).

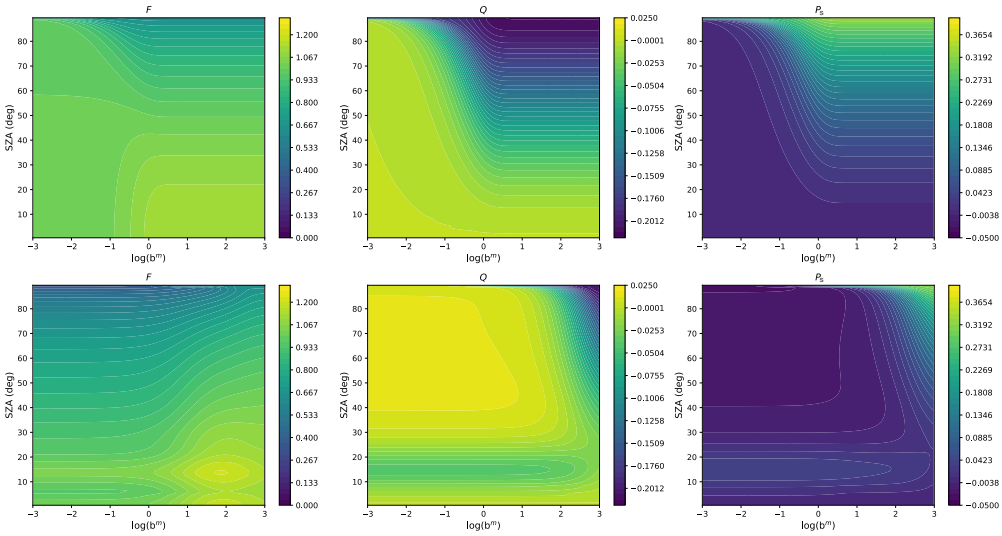

Figure 2.6: Total flux F (left column), linearly polarized flux Q (middle column) and degree of polarization P_S (right column) as functions of the atmospheric gas optical thickness b^m and the solar zenith angle θ_0. The viewing zenith angle θ is 0° (nadir view). In the top row, the atmosphere is cloud-free and the surface reflects Lambertian with an albedo of 1.0. In the bottom row, the atmosphere contains an additional, optically thick cloud with its top at 65 km.

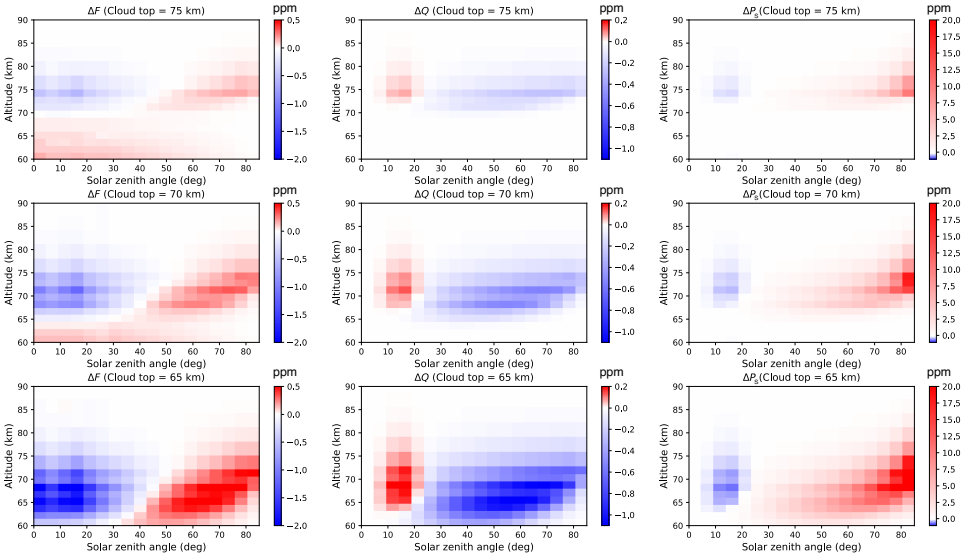

Figure 2.7: ΔF (left column), ΔQ (middle column), and ΔP_S (right column) (all in ppm) upon increasing the gas density or $b^{\mathrm{m}}_{\mathrm{sca}}$ in an atmospheric layer by 1 %, as functions of θ_0, for different cloud top altitudes: 75 km (top row), 70 km (middle row), and 65 km (bottom row). The cloud and haze scale heights are 4 km. The wavelength is 600 nm, viewing angle $\theta = 0°$. A positive/red (negative/blue) color indicates an increase (decrease) in F, Q, or P_S with an increase in b^{m}.

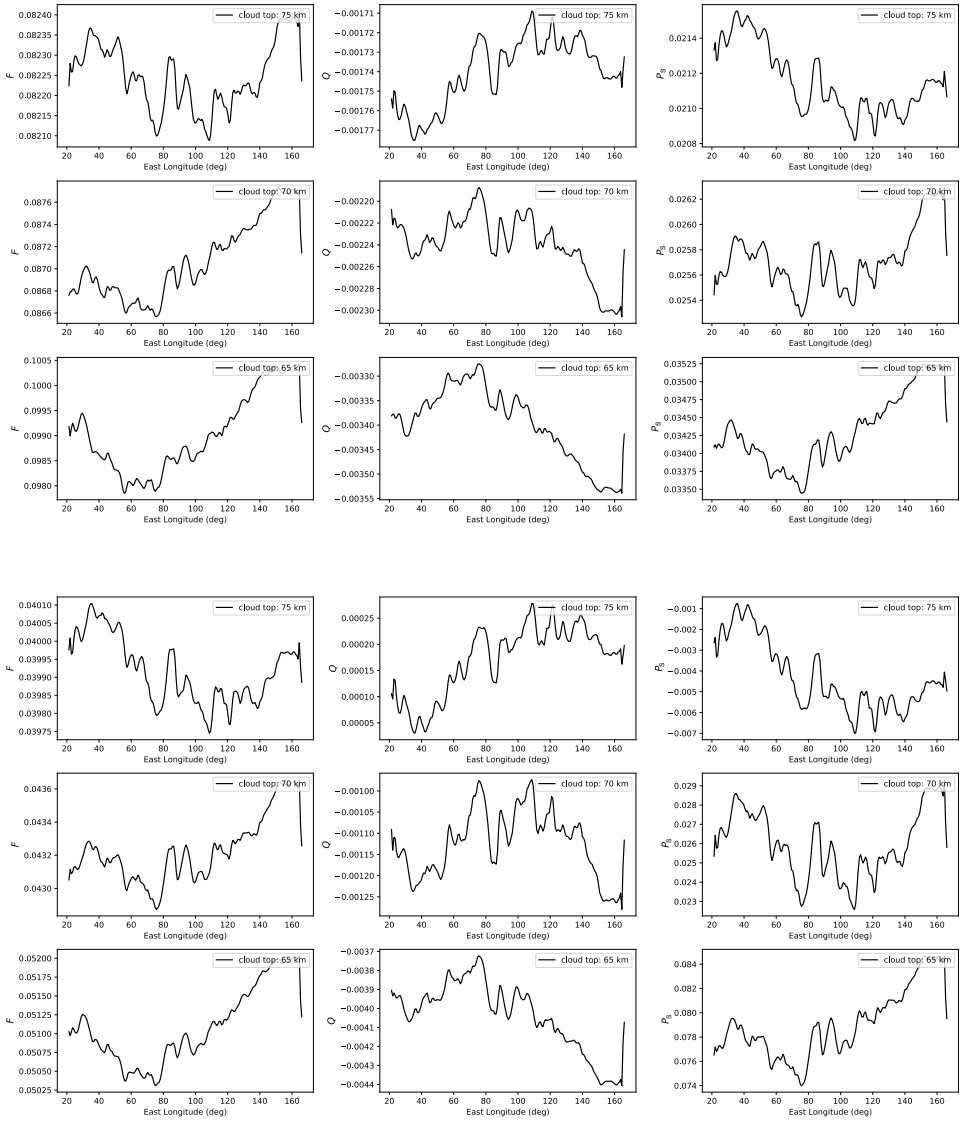

Figure 2.8: F (left column), Q (middle column), and P_S (right column) at $\lambda = 300$ nm across the afternoon pressure map of Aphrodite Terra at a latitude of 0°, for cloud top altitudes of 75 km (top row), 70 km (middle row), and 65 km (bottom row). The viewing zenith angle θ is 0° (nadir view). For the top three rows, solar zenith angle $\theta_0 = 30°$, and for the bottom three rows, solar zenith angle $\theta_0 = 60°$. The maximum intensity of the wave occurs around 80° longitude.

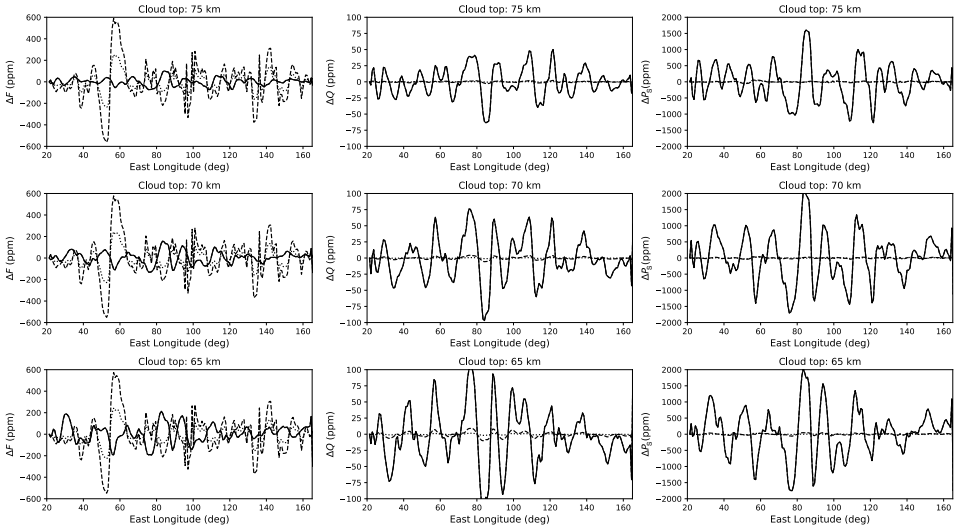

Figure 2.9: Similar to Fig. 2.8, except with the background subtracted (for each data-point, the background is the average of the 12 surrounding data-points), and for 300 nm (solid lines, see Fig. 2.8), 600 nm (dashed lines), and 900 nm (dotted lines). Solar zenith angle θ_0 is 60° and viewing angle $\theta = 0°$. The values are shown in ppm.

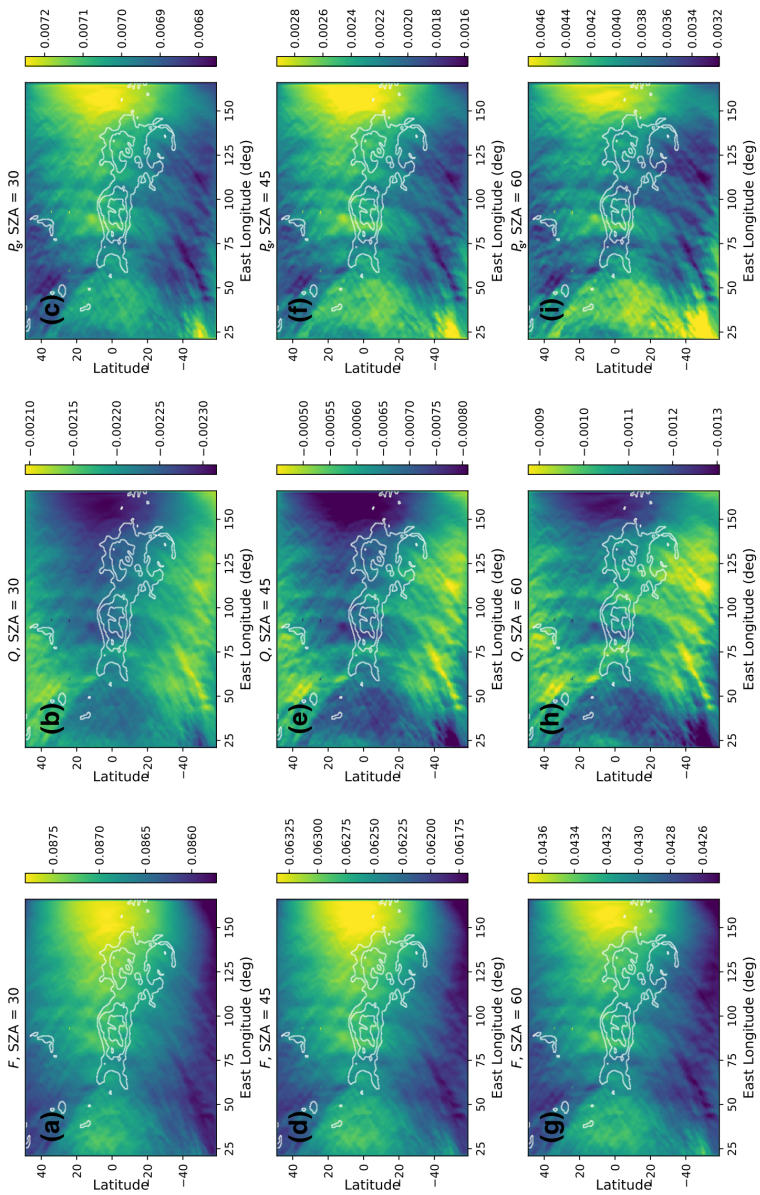

Figure 2.10: F (first column), Q (second column), and P_S (third column) (all in ppm) across Aphrodite Terra. The cloud top is at 65 km and wavelength λ is 300 nm. The local solar zenith angle θ_0 is 30° (top row), 45° (middle row), or 60° (bottom row), and the local viewing angle $\theta = 0°$.

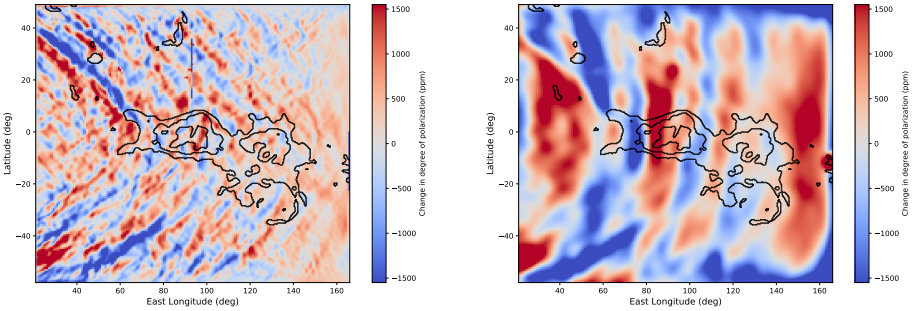

Figure 2.11: The map of the change in P_S from Fig. 2.10 for $\theta_0 = 60^\circ$ with two different filters applied to remove the background signal: a high-pass filter with $\sigma = 15$ (left) and a low-pass filter with $\sigma = 3$ (right). The values are shown in ppm. The maximum change in P_S in the low pass filter (right) is 2000 ppm at around 80° East-longitude.

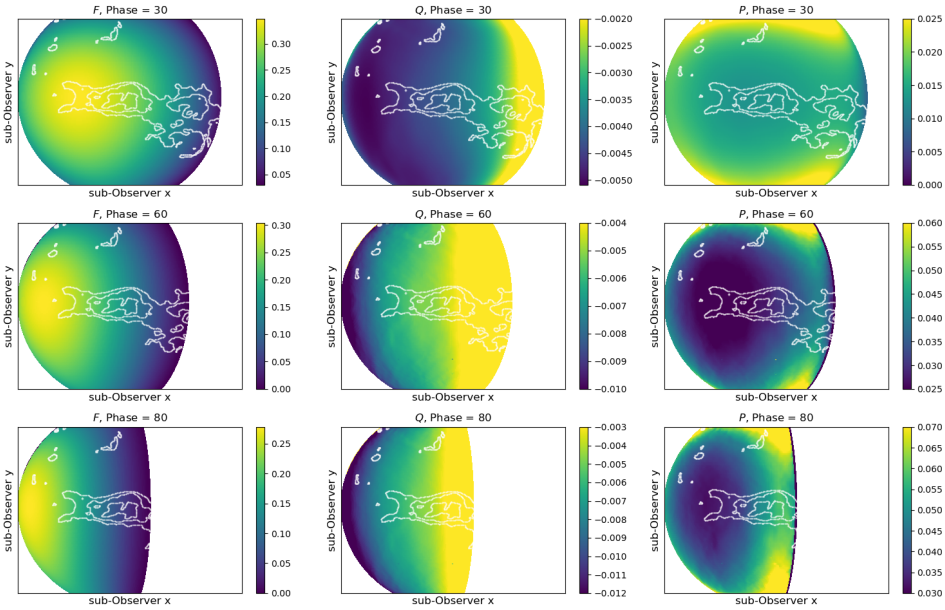

Figure 2.12: Similar to Fig. 2.10, except for an Earth-based observer line-of-sight, for three planetary phase angles α: 30° (top row), 60° (middle row), and 80° (bottom row). Only the illuminated and observable part of the planetary disk is shown.

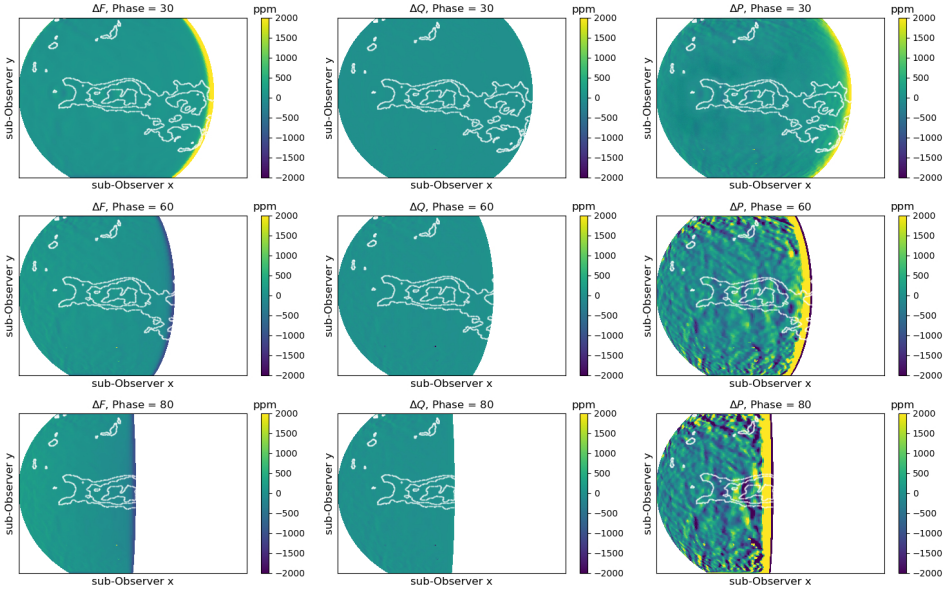

Figure 2.13: Similar to Fig. 2.12, except with the background removed using a Gaussian filter with $\sigma = 3$. The flux and polarization variations are shown in ppm.

3

PLANET–WIDE, CONCENTRIC DENSITY WAVES IN VENUS'S UPPER ATMOSPHERE REVEALED THROUGH POLARIMETRY

GOURAV MAHAPATRA, MICHIEL RODENHUIS, LOÏC ROSSI, DAPHNE STAM, FRANS SNIK, CHRISTOPH KELLER

Planet-wide concentric waves have been observed on Venus through a ground-based highly accurate polarimeter. These waves appear to be in the thin, gaseous atmosphere above Venus' upper cloud deck and the center of the waves lies slightly down–wind of the sub–solar region. The presence of the waves is derived from rings in high–precision linear polarization images of sunlight that is reflected by Venus that were obtained over a period of about 36 minutes with the Extreme polarimeter (ExPo)(Rodenhuis et al., 2012) on the William Herschel Telescope on La Palma. The waves do not show up in simultaneously obtained images of the brightness (total flux) across Venus' disk. Upper atmospheric density waves were already detected in in–situ measurements by the Pioneer Venus spacecraft, except necessarily only on a local, along–track scale, and were tentatively explained as gravity waves due to convective upwelling above Venus' clouds and hazes (Kasprzak et al., 1988). The atmosphere of Venus has been shown to harbor waves on various spatial and

temporal scales by other spacecraft too, such as the Mariner 10, several Venera missions, and Venus Express (Piccialli et al., 2014). Our numerical simulations show that both the flux and the degree of linear polarization across the disk are mostly determined by the characteristics of the cloud layer, but that changing the density of the carbon–dioxide gas above the clouds by 5% - 10% will give rise to a change of the polarization within ExPo's sensitivity, while there would be no detectable change in Venus' brightness. Such density waves could be triggered by the strong irradiation of the sub–solar region. Their spread across the planet seems to follow the known sub–solar to anti–solar flow. These unique, planet–wide waves as revealed by the highly sensitive polarimeter ExPo, might help to explain the driving mechanisms of the super–rotating zonal flow as they transfer momentum from the cloud tops and deposit energy in the thermosphere (Alexander, 1992; Bougher et al., 2006).

3.1. INTRODUCTION

There is ample evidence for gravity wave activity on Venus. Indeed, waves with various extensions have been observed through direct imaging (e.g. Venus Express and Akatsuki images) as well as through in-situ measurements (e.g. with the Pioneer Venus-ONMS instrument). The properties of gravity waves depend on the atmospheric structure and on the thermal and dynamical interactions within the atmosphere and there's strong evidence that gravity waves influence the local atmospheric density structure. A recent example is the bow-shaped planet-wide gravity wave detected by the Akatsuki Spacecraft just after it entered into the orbit around Venus. These waves were topographic gravity waves, generated by near-surface flows impinging on mountains and propagating upward. Since these waves possess momentum in the direction opposite to Venus' super-rotation, their dissipation at high altitudes exerts deceleration on the mean flow (Kitahara et al., 2019). Venus' middle and upper atmosphere has long been expected to support gravity waves with wavelengths ranging from 100 to 600 km (Kasprzak et al., 1988). It has been conjectured that wave drag and turbulence because of such internal gravity waves propagating in Venus' upper atmosphere is critical to understanding its super-rotation (Alexander, 1992; Alexander et al., 1993). Detecting and characterizing them both on Venus' day-side and night-side would improve our understanding of our still enigmatic neighboring planets dynamic atmosphere.

Gravity waves have been observed through various means such as direct imaging at various wavelengths (Piccialli et al., 2014; Peralta et al., 2017) and in-situ measurements (Kasprzak et al., 1988; Persson, 2015; Migliorini et al., 2011). The density variations in the thin atmosphere above the clouds will be quite small, and very challenging to detect with flux measurements of e.g. reflected sunlight, in particular because the bright, underlying clouds will completely dominate the signal. Polarimetry could facilitate the detection of subtle atmospheric density changes on the upper atmosphere of Venus because of its higher sensitivity through the process of Rayleigh scattering by the gas molecules.

This paper presents ground-based imaging polarimetry of the Venusian atmosphere at various wavelengths, utilizing both narrow and broad-band filters with the Extreme Polarimeter (ExPo) instrument. The study aims to explain the spurious rings observed in the data by employing a radiative transfer model specifically adapted for Venus's atmosphere. ExPo is an experimental instrument developed to provide high-contrast imaging polarimetry, with the primary objective of observing weak sources, such as exoplanets, in reflected (and thus linearly polarized) starlight at small angular separations from their host stars. The instrument is highly sensitive to linearly polarized light, capable of achieving a sensitivity of 10^{-4} provided sufficient photons are available.

Section 3.2 details the observations obtained using ExPo. Section 3.3 outlines the observational and numerical methods employed in this study, including definitions of polarized light observations (Sect. 3.3.1), a description of the instrument (Sect. 3.3.2), and the radiative transfer algorithm (Sect. 3.3.3). Section 3.4 provides a discussion of the observations, while Section 3.5 examines the observations in conjunction with the results of the radiative transfer model and their implications.

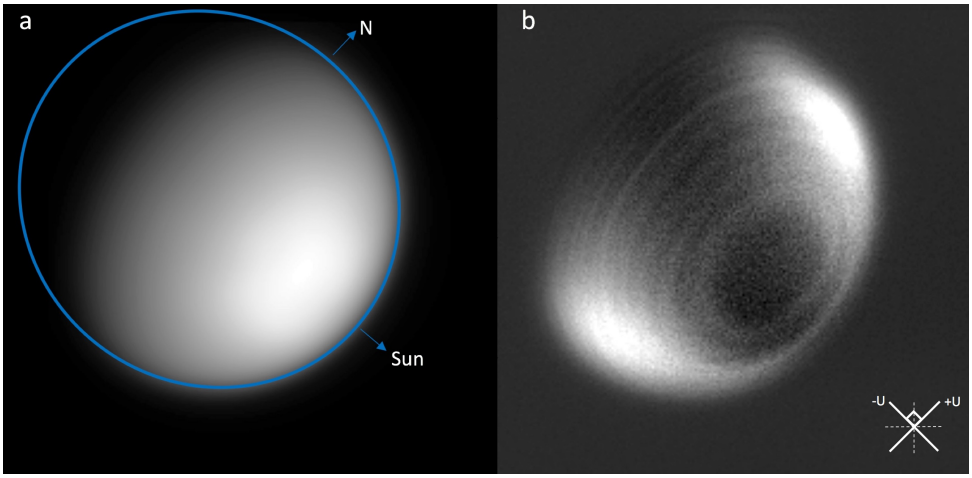

Figure 3.1: Venus in total flux (left) and polarized flux (right) using the H-alpha filter (Table 3.1). The polarized flux corresponds to the Stokes parameter U (Hansen and Travis, 1974), measured along the two orthogonal directions indicated below the image. Due to Venus' orientation, the planetary scattering plane forms an angle of almost 45° with the instrument's optical plane. The concentric rings originate near the sub-solar point and extend across the entire planet, wrapping around the polar regions. This is clearly visible in the Stokes parameter U. These rings are much less visible in the Stokes parameter Q, indicating that most of the planet's polarized flux is parallel to the planetary scattering plane, which coincides with the planet's equatorial plane. The spatial resolution is approximately 775 km on Venus' disk at the sub-observer point.

3.2. OBSERVATIONS

The Venus images we present here are truly serendipitous: they were captured with the Extreme Polarimeter (ExPo) as it was temporarily installed at the Nasmyth focus of the 4.2 m William Herschel Telescope (WHT) of the Isaac Newton Group (ING) of telescopes on La Palma, Canary Islands, Spain, during a period of about 36 minutes in which we were waiting for the end of the astronomical evening twilight on 24 May 2010. The images were taken through the six optical filters that happened to be available: H-alpha, H-alpha continuum, Na continuum, Sloan r, Sloan i, and Na. The filter specifications and the times at which they were used are listed in Table 3.1. ExPo is designed to capture images of faint, linearly polarized sources by suppressing the contributions of unpolarized light to a high degree (Rodenhuis et al., 2012). The seeing on the evening of the observations (May 24th, 2010), was excellent (0.8" or better), although the horizon where Venus was observed during the last observations just before setting, appeared to be hazy possibly leading to increased atmospheric seeing values. The absolute accuracy of these impromptu images (thus, the background polarization level) can only be calibrated to 1-2%. This, however, is no limitation for their interpretation because ExPo has been designed to reach very high polarimetric sensitivity of 10^{-4}.

Figure 3.1 shows Venus in total (left) and linearly polarized (right) fluxes as imaged through the H–alpha continuum filter (see Tab. 3.1). While the total flux image shows a homogeneous planet that is brightest near the sub–solar region, the polarization image shows relatively high polarized fluxes across the North and South polar regions, low

Table 3.1: The specifications of our Venus images, with the central wavelength λ_0 and width $\Delta\lambda$ of each filter, angle θ of the FLC, the time of observation, the elevation of Venus, the airmass, and the visibility of the rings. All images were captured with ExPo on the WHT, La Palma, Spain, on the evening of 24 May 2010. Venus' phase angle at the time was 48.7°, the planet's diameter 12.5" (outside the Earth's atmosphere), the North polar angle 1.4°, and the sub–observer latitude on the planet -2.21°, according to JPL's Horizons online ephemeris tool.

Filter	λ_0 [nm]	$\Delta\lambda$ [nm]	θ [°]	Time [UTC]	Elevation [°]	Airmass	Rings visible
H–alpha	656.3	1.0	45.0	20:28:18	24.06	2.438	yes
			67.5	20:31:03	23.43	2.499	yes
H–alpha cont.	647.1	1.0	0.0	20:33:45	22.80	2.541	yes
			22.5	20:39:14	21.75	2.678	yes
			45.0	20:41:33	21.34	2.727	yes
			67.5	20:43:59	20.71	2.778	yes
Na	589.4	5.0	45.0	20:51:38	19.05	3.003	yes
			67.5	20:54:01	18.63	3.097	yes
Na cont.	580.0	5.0	45.0	21:03:19	16.77	3.419	no
			67.5	21:06:30	16.16	3.542	no
Sloan r	623.1	137.3	45.0	21:23:30	12.68	4.449	no
			67.5	21:25:39	12.07	4.586	no
Sloan i	762.5	152.6	45.0	21:32:21	10.85	5.139	no
			67.5	21:34:31	10.45	5.322	no

polarization at lower latitudes, all overlaid with what appear to be narrow, higher polarization rings.[1] The high polarization across Venus' poles has been observed before, for example, by OCCP (Travis, 1979) on the Pioneer Venus spacecraft (Kawabata et al., 1980; Sato et al., 1996) and by SPICAV on Venus Express (Rossi et al., 2015). It is worth noting that the Pioneer Venus OCPP had a polarimetric sensitivity of approximately 10^{-3} (Hunten et al., 2022), which is a magnitude lower than that of ExPo. The SPICAV-IR instrument on Venus Express, while capable of deriving partial polarization from orthogonally polarized flux measurements, was not specifically calibrated for polarimetric observations. Consequently, the exact polarimetric sensitivity of SPICAV-IR remains unknown. The rings have, to the best of our knowledge, never been observed before. The rings appear concentric around a region slightly downwind of the sub-solar point, covering the entire illuminated and visible disk, including the polar regions. They are observable in all three narrow-band filters. The typical difference between the polarized flux inside and outside the brightest ring in the image in Fig. 3.1, is $5 \cdot 10^{-4}$.

As detailed in the Table 5.1, various other filters were used to observe Venus on the same day during this observation campaign. Fig. 3.2 shows our six observations of Venus in polarized intensity which is defined as $\sqrt{Q^2+U^2}$. In all images, Venus shows a similar background polarized flux that is small in the equatorial region and high towards the poles. Three of the images (obtained through the H-alpha, H-alpha cont. and Na filters) show concentric rings, and three (obtained through the Sloan r, Sloan i, and Na cont. filters) do not show the rings. The three images in Sloan r, Sloan i, and Na cont. filters were obtained last (see Table 3.1) when Venus was already very low on the horizon and the airmass was large (3.4-3.5 for the Na cont. filter, 4.4-4.6 for the Sloan r filter, and 5.1-5.3 for the Sloan i filter, respectively). It is important to note that ExPo did not have an oper-

[1] Although we do not know whether all arcs form full rings across the planet, we will refer to them as 'rings.'

ational Atmospheric Dispersion Corrector at the time of these observations, potentially resulting in some spectral smearing in broadband data.

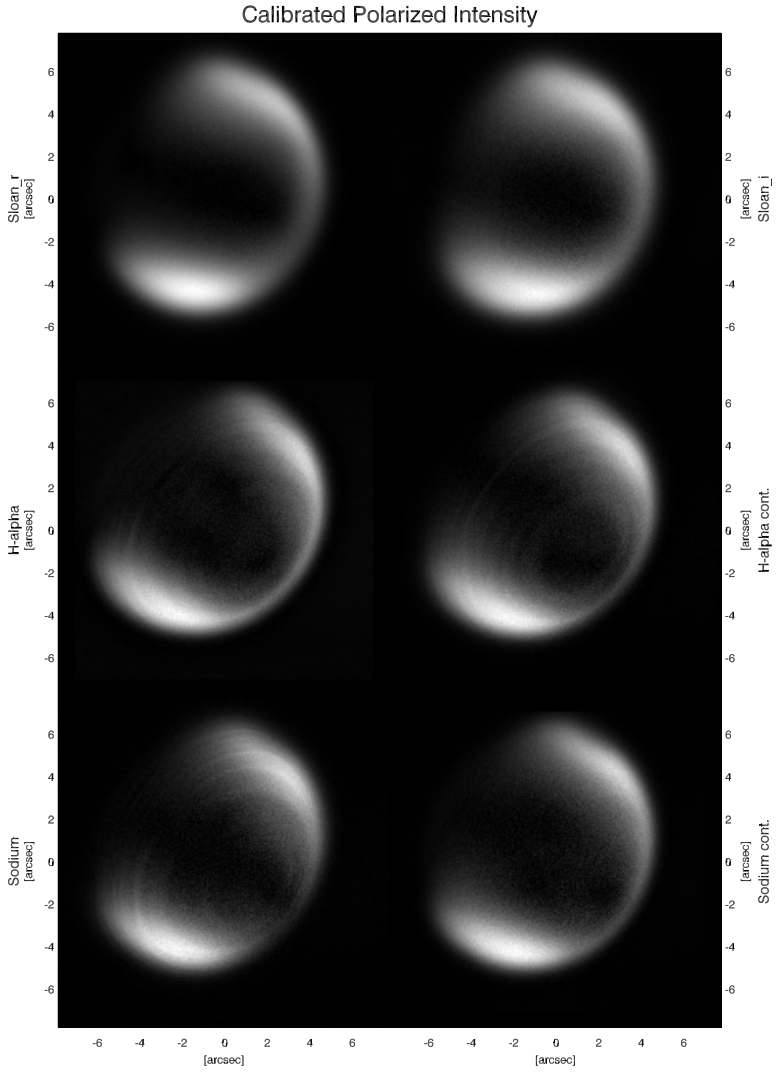

Figure 3.2: The measured polarized intensity (defined as $\sqrt{Q^2+U^2}$) in the six filters that were used in the observations. Top row: images taken through the Sloan r and Sloan i broadband filters. Middle row: images taken through the H–alpha and H–alpha cont. filters. Bottom row: images taken through the Na and Na cont. filters. The time sequence of the observations is from top left to bottom right: 5 - 6 - 1 - 2 - 3 - 4. The rings are visible in the first 3 observations in chronological order, and invisible in the last 3 observations.

Figure 3.3 shows the degree of polarization U/F for the six observations, except only for the latitudes between -30° and +30°, as functions of the longitude in the planet mea-

sured with respect to the sub-observer or sub-earth point. The blue line in each sub-figure shows the degree of polarization averaged between the latitudes -5° and +5°. The rings can be seen in the blue lines in the upper three sub-figures, that pertain to the observations that were taken first, and not in the lowest three sub-figures, that pertain to the observations that were taken last. The strength of the ring pattern can be seen to vary strongly from sub-figure to sub-figure. The theoretical wavelength dependence, as shown in Fig. 3.7, is not obvious from the observations. This is not surprising because already during the first observations (through the H-alpha filter), Venus had an elevation of only about 24° and thus low on the hazy horizon. Future, dedicated observations through well-chosen filters would help to properly investigate the wavelength dependence of the features.

The strong feature at longitudes of about -12° in the observations through the H–alpha filter, appears to also have been captured in the observations through the H–alpha cont. filter, except somewhat close towards the terminator. The time interval between these observations was about 10 minutes (see Table 3.1). It is tempting to derive a speed of a density wave, assuming it is indeed the same feature, but because of the lack of continuous observations and without any knowledge on the variability of the pattern in strength and location, one should indeed be careful using this for the characterization of the phenomenon.

Figure 3.4, finally, shows the direction of polarization as derived from the observations through the H-alpha cont. filter. The direction is mostly parallel to the planetary scattering plane, and thus to the equator of the planet. The direction does not show deviations related to the rings, which corresponds with the results of our numerical simulations (see Fig. 3.7), in which the polarization continuum is negative, hence parallel to the reference plane. An increased gas density above the clouds and hazes will force the degree of polarization closer towards zero, but P remains negative.

The direction of polarization across the disk in Fig. 3.1 is mostly parallel to the planetary scattering plane, i.e. the plane containing the Sun, Venus' equator, and the observer, without a significant change of the direction of polarization across the rings (see Fig. 3.4). The rings appear in the images taken in the H–alpha, H–alpha continuum, and the Sodium filters, which were taken first during the excellent seeing conditions. In the images taken in Na continuum, Sloan r, and Sloan i filters, the polarization across the poles is still high and that at low latitudes is still low, but there are no rings distinguishable within ExPo's sensitivity. We have no other images of Venus with rings, as we did not have other opportunities to observe Venus under such advantageous seeing conditions, and, due to the experimental nature of ExPo, the instrument has been taken apart and its optical components reused for other experiments. To the best of our knowledge, there are no other polarimeters available that combine imaging with ExPo's high polarimetric sensitivity.

As these rings have not been observed before, we first suspected them to be due to an instrumental effect, in particular because they appear to be concentric around the brightest region on Venus' disk. However, we have not been able to identify an instrumental effect that would leave rings in the images taken in the H–alpha, H–alpha continuum and Na–filters and not in the other filters. Also, they have not appeared in any high–precision polarization images of other objects taken with ExPo (Min et al., 2013; Jeffers

et al., 2012; Rodenhuis et al., 2012), nor in carefully executed measurements with ExPo in our optical laboratory, amongst others, simulating Venus using a white styrofoam ball. We also considered optical effects in the Earth's atmosphere, such as scattering by an optically thin layer of high–altitude ice particles, but failed to find an explanation for the shape and location of the pattern on Venus, for the stability of the pattern during the observations through the first three filters, and especially for the consistent direction of polarization across Venus' disk and the rings.

Indeed after ruling out all the possibilities related to instrumental artefacts, the only explanation for the pattern appears to be the scattering of sunlight within Venus' upper atmosphere. The high airmass during our observations in the last three filters (see Table 3.1), and thus the lower spatial resolution on Venus, appears to explain the lack of rings in those images. There are several explanations why such rings would not have been observed before. Firstly, while Venus has been observed with ground–based polarimeters before (Hansen and Hovenier, 1974), those observations did not have a spatial resolution high enough to resolve such narrow rings. Spatially resolved polarimetry of Venus was performed with the Pioneer Venus' Orbiter Cloud Photopolarimeter (OCPP) (Travis, 1979). The polarimetric accuracy of OCPP, however, was 10^{-3} in the 365 – 935 nm range (Travis, 1979), which would have been insufficient to detect the rings that we have observed. The SPICAV instrument on the European Space Agency's (ESA's) Venus Express (VEx) mission had polarimetric capabilities thanks to its opto-acoustic modulator (Korablev et al., 2012; Rossi et al., 2015), but it covered mostly near infrared wavelengths, at which, as we will show later, the rings would have been virtually invisible. Also, SPICAV's polarimetric accuracy was at most 10^{-3}. The Japanese Space Agency's (JAXA) Akatsuki mission that has been orbiting Venus since 2015, unfortunately lacks a polarimeter.

3.3. OBSERVING AND MODELLING THE RINGS IN POLARIZATION

3.3.1. FLUX AND POLARIZATION DEFINITIONS

We describe light with a Stokes (column) vector **F** as follows (Hansen and Travis, 1974)

$$\mathbf{F}(\lambda) = \left[F(\lambda), Q(\lambda), U(\lambda), V(\lambda)\right], \tag{3.1}$$

with F the total flux, Q and U the linearly polarized fluxes, and V the circularly polarized flux, all in units of W m^{-2}. These fluxes in principle all depend on the wavelength, but we will compute and present them per spectral filter. For sunlight that is reflected by a planet, the circularly polarized flux V is very small (Hansen and Travis, 1974; Rossi, L. and Stam, D. M., 2018) and it is not measured by ExPo. The linearly polarized fluxes Q and U are defined with respect to a reference plane, which in our numerical simulations is the planetary scattering plane, i.e. the plane containing the Sun, the equator of Venus, and the observer. The degree of linear polarization is defined as

$$P = \frac{\sqrt{Q^2 + U^2}}{F}, \tag{3.2}$$

with $\sqrt{Q^2 + U^2}$ the total linearly polarized flux. While the degree of linear polarization P is independent of the reference plane used for defining Stokes parameters Q and U, the

direction or angle of linear polarization, χ, is not. Angle χ can be derived from

$$\tan 2\chi = U/Q. \tag{3.3}$$

The value of χ is chosen in the interval $[0°, 180°\rangle$, and such that $\cos 2\chi$ has the same sign as Q (Hansen and Travis, 1974). In case parameter U equals zero, we can employ an alternative definition of the degree of linear polarization that includes information about the direction of polarization, namely

$$P = -Q/F, \tag{3.4}$$

If $P > 0$ the direction of polarization is perpendicular to the reference plane and if $P < 0$ it is parallel to the reference plane.

3.3.2. EXPO INSTRUMENT DESCRIPTION

Polarimetry is a differential measurement technique: in a simple polarimeter, a polarizing beam–splitter is used to split the light in its two orthogonally polarized components. Of each of these components, the flux is then measured. The difference of two such flux measurements yields the net linearly polarized flux of the incoming light along the orthogonal axes defined by the beam–splitter. ExPo (Rodenhuis et al., 2008; Canovas et al., 2011) has been designed to avoid measuring systematic or temporal errors by using a dual-beam exchange measurement approach: The light is passed through a polarising beamsplitter and the two orthogonal polarisation states are measured simultaneously. In front of the beamsplitter, a switchable half-wave plate can interchange the two polarisation states between the two beams. In the second state, the two polarisation states are measured again. This technique is depicted in Fig. 3.5. A FLC modulator switches between the two states synchronously with the camera's 35 Hz frame rate, thus canceling first–order systematic errors due to optical path differences and reducing noise due to variations in atmospheric seeing between consecutive frames.

Calling the two states A and B and denoting the two beams by L and R, the polarised flux is found through the double difference of the four measurements:

$$Q = A_L - A_R - B_L + B_R \tag{3.5}$$

Rotating the switchable half-wave plate by 22.5° makes the polarimeter sensitive to polarisation at 45° with respect to the first measurement, allowing the measurement of the U component of the Stokes vector. The polarised flux is again found through the double difference:

$$U = [A_L - A_R - B_L + B_R]^{45^\circ} \tag{3.6}$$

ExPo was a regular visitor to the William Herschel Telescope (WHT), part of the Isaac Newton Group of telescopes on the island of La Palma, Spain. The WHT has an experimental instrument station located at one of the Nasmyth ports, where a standard optical table is available on which such instruments can be mounted.

3.3.3. RADIATIVE TRANSFER ALGORITHM

Our radiative transfer computations to reproduce the rings are based on an adding–doubling algorithm (de Haan et al., 1987) that fully includes linear and circular polarization for all orders of scattering. The algorithm requires a model atmosphere to be

composed of a stack of horizontally homogeneous layers, and, for each of the layers, it requires the specification of the optical thickness b, the single scattering albedo ω, and the single scattering matrix $\mathbf{S}$ of the scattering particles in the layer. The atmosphere is bounded below by a horizontally homogeneous surface, which we assume to be black.

The optical thickness of an atmospheric layer at wavelength λ is given by

$$b(\lambda) = b^{\mathrm{m}}(\lambda) + b^{\mathrm{a}}(\lambda), \tag{3.7}$$

with b^{m} the layer's gaseous optical thickness and b^{a} the layer's aerosol optical thickness, which is due to the cloud or haze particles (in our model atmosphere, a layer that contains aerosol, contains either cloud or haze particles, not a mixture of both). The single scattering albedo in the layer is given by

$$\omega(\lambda) = \frac{\omega^{\mathrm{m}}(\lambda) b^{\mathrm{m}}(\lambda) + \omega^{\mathrm{a}}(\lambda) b^{\mathrm{a}}(\lambda)}{b^{\mathrm{m}}(\lambda) + b^{\mathrm{a}}(\lambda)}, \tag{3.8}$$

with ω^{m} the single scattering albedo of the gas molecules, and ω^{a} the single scattering albedo of the cloud or haze particles in the layer. The single scattering matrix of the particles in a layer is given by

$$\mathbf{S}(\lambda) = \frac{\omega^{\mathrm{m}}(\lambda) b^{\mathrm{m}}(\lambda) \mathbf{S}^{\mathrm{m}}(\lambda) + \omega^{\mathrm{a}}(\lambda) b^{\mathrm{a}}(\lambda) \mathbf{S}^{\mathrm{a}}(\lambda)}{\omega(\lambda) b(\lambda)}, \tag{3.9}$$

with $\mathbf{S}^{\mathrm{m}}$ the single scattering matrix of the gas and $\mathbf{S}^{\mathrm{a}}$ the single scattering matrix of the cloud or haze particles.

The single scattering matrix $\mathbf{S}^{\mathrm{m}}$ of anisotropic gaseous scattering is given by Hansen and Travis (1974)

$$\mathbf{S}^{\mathrm{m}}(\lambda, \Theta) = \Delta(\lambda) \begin{bmatrix} \frac{3}{4}(1+\cos^2\Theta) + \frac{1}{\Delta(\lambda)} - 1 & -\frac{3}{4}\sin^2\Theta & 0 & 0 \\ -\frac{3}{4}\sin^2\Theta & \frac{3}{4}(1+\cos^2\Theta) & 0 & 0 \\ 0 & 0 & \frac{3}{2}\cos\Theta & 0 \\ 0 & 0 & 0 & \Delta'(\lambda)\frac{3}{2}\cos\Theta \end{bmatrix}, \tag{3.10}$$

where

$$\Delta(\lambda) = \frac{1-\delta(\lambda)}{1+\delta(\lambda)/2} \quad \text{and} \quad \Delta'(\lambda) = \frac{1-2\delta(\lambda)}{1-\delta(\lambda)}. \tag{3.11}$$

The four layers of our model atmosphere all contain pure carbon-dioxide, i.e. CO_2, gas. In the filters that we used for our observations, CO_2 does not have any significant absorption bands. We thus neglect gaseous absorption in our computations, i.e. $\omega^{\mathrm{m}} = 1.0$. The gas optical thickness, b^{m}, at a given wavelength λ, of an atmospheric layer is then computed according to

$$b^{\mathrm{m}}(\lambda) = N^{\mathrm{m}} \sigma^{\mathrm{m}}(\lambda), \tag{3.12}$$

with N^{m} the gas column number density (in m^{-2}) in the layer, and σ^{m} the gaseous extinction cross–section (in m^2), which in our case equals the gaseous scattering cross–section, due to the lack of absorption. This cross–section is given by

$$\sigma^{\mathrm{m}}(\lambda) = \frac{24\pi^3}{N_{\mathrm{L}}^2} \frac{(n^2(\lambda)-1)^2}{(n^2(\lambda)+2)^2} \frac{(6+3\delta(\lambda))}{(6-7\delta(\lambda))} \frac{1}{\lambda^4}, \tag{3.13}$$

Table 3.2: The depolarization factor δ (Sneep and Ubachs, 2005) and the the refractive index nSneep and Ubachs (2005) of CO_2, and the molecular scattering optical thickness $b^{\mathrm{m}}_{\mathrm{tot}}$ of the standard model atmosphere as a whole at the central wavelength λ_0 of each filter (cf. Table 3.1). Of the molecular scattering optical thickness of the atmosphere, 98.92% pertains to layer 1 (the bottom layer), 1.022% to layer 2, 0.000484% to layer 3, and 0.0000538% to layer 4 (the top layer). Furthermore, $\sigma^{\mathrm{a}}_{\mathrm{cloud}}$ is the scattering cross–section of the cloud particles, $b^{\mathrm{a}}_{\mathrm{cloud}}$ the optical thickness of the cloud, $\sigma^{\mathrm{a}}_{\mathrm{haze}}$ the scattering cross-section of the haze particles, and $b^{\mathrm{a}}_{\mathrm{haze}}$ the optical thickness of the haze.

Filter	λ_0 [nm]	δ	n	$b^{\mathrm{m}}_{\mathrm{tot}}$	$\sigma^{\mathrm{a}}_{\mathrm{cloud}}$ [μm^2]	$b^{\mathrm{a}}_{\mathrm{cloud}}$	$\sigma^{\mathrm{a}}_{\mathrm{haze}}$ [μm^2]	$b^{\mathrm{a}}_{\mathrm{haze}}$
Na cont.	580.0	0.0784	1.0004262	13.43	6.635	30.00	0.154	0.020
Na	589.4	0.0783	1.0004260	12.57	6.634	29.99	0.151	0.020
Sloan r	623.1	0.0779	1.0004251	9.41	6.638	30.01	0.141	0.018
H-alpha cont.	647.1	0.0772	1.0004246	8.59	6.650	30.06	0.134	0.017
H-alpha	656.3	0.0776	1.0004244	8.11	6.657	30.10	0.131	0.017
Sloan i	762.5	0.0769	1.0004228	4.41	6.928	31.32	0.104	0.014

with N_{L} Loschmidt's number, n the refractive index of CO_2 under standard conditions, and δ the depolarization factor of pure CO_2. For n and δ of pure CO_2 gas, we assume the wavelength dependent relations presented by Sneep and Ubachs (2005).

Assuming that each atmospheric layer is in hydrostatic equilibrium, a layer's gas column number density N^{m} (in m^{-2}) is computed using

$$N^{\mathrm{m}} = N_{\mathrm{A}} \frac{p_{\mathrm{bot}} - p_{\mathrm{top}}}{mg}, \tag{3.14}$$

with N_{A} Avogadro's number, p_{bot} and p_{top} the pressures at the bottom and at the top of the atmospheric layer, respectively, m the average molar mass of the gas, for which we use the value for pure CO_2, i.e. 44.01 g/mol, g the acceleration of gravity, which we assume to be altitude independent across the region of Venus' atmosphere that we study and equal to 8.87 m/s^2. Table 3.3 shows the pressures at the bottom and the top of each of the four atmospheric layers that we use in our model, the computed gas column number density N_{m} and gaseous optical thickness b^{m} at 580 nm (the central wavelength of the Na cont. filter) for each of the atmospheric layers. We impose the variations in the gas column number density that give rise to the rings in Venus' polarized image on the highest atmospheric layer. We thus simply add an amount δN^{m} to the value of $N^{\mathrm{m}} = 5.0 \cdot 10^{27}$ m^{-2} (see Table 3.3).

The second and third layers of the model atmosphere contain, respectively, cloud and haze particles (see Table 3.3). These particles are assumed to be spherical and homogeneous. For both particle types, we assume a two parameter gamma size distribution (Hansen and Travis, 1974). The cloud particles have an effective radius r_{eff} of 1.05 μm and an effective variance v_{eff} of 0.07 (Hansen and Hovenier, 1974), and the haze particles, $r_{\mathrm{eff}} = 0.25$ μm and $v_{\mathrm{eff}} = 0.25$ (Sato et al., 1996). We assume that the cloud and haze particles consist of 75% sulfuric acid (Hansen and Hovenier, 1974), and adopt the following wavelength dependence for their refractive index n_{r}

$$\frac{n_{\mathrm{r}}^2(\lambda) - 1}{n_{\mathrm{r}}^2(\lambda) + 2} = \frac{-29.8034}{\lambda^{-2} + 116.3899}, \tag{3.15}$$

as derived from the values provided by Hansen & Hovenier (Hansen and Hovenier, 1974).

For each central filter wavelength λ_0 (Table 3.1), we compute the optical properties of the cloud and haze particles, i.e. their extinction cross–section σ^a, and their single scattering matrix $\mathbf{S}^a$, using a Mie–algorithm (de Rooij and van der Stap, 1984). Their single scattering albedo ω^a equals 1.0 due to the lack of absorption.

Figure 3.6 shows the total flux and degree of linear polarization of unpolarized incident light that is singly scattered by the cloud and haze particles for the central filter wavelengths λ_0. For comparison, we have also included the curves for the light that is scattered by the gaseous molecules. As can be seen, at a single scattering angle of 131.3°, which corresponds to Venus' phase angle of 48.7° at the time of the ExPo observations, the light scattered by the cloud and haze particles has a direction of polarization that is parallel to the reference plane (which would correspond to the planetary scattering plane, which also contains the planet's equator), while the direction of polarization of the light that is scattered by the gaseous molecules is perpendicular to this plane.

We choose the cloud and haze optical thickness, b^a, of atmospheric layers two and three according to previous Venus atmospheric models (Kawabata et al., 1980; Rossi et al., 2015). Table 3.3 lists the optical thickness b^a of each layer at 580 nm (which is the central wavelength λ_0 of the Na cont. filter). The cloud or haze optical thicknesses at other wavelengths are computed according to

$$b^a(\lambda) = b^a(580\text{ nm})\frac{\sigma^a(\lambda)}{\sigma^a(580\text{ nm})}. \tag{3.16}$$

The values of b^a of the cloud (b^a_{cloud}) and the haze (b^a_{haze}) at the central filter wavelengths can be found in Table 3.2.

We assume that the sunlight that is incident on the planet is unpolarized (Kemp et al., 1987), and it is thus described by the column vector $F_0[1,0,0,0]$, with F_0 equal to π. Matrix $\mathbf{R}$ depends on the composition and structure of the local atmosphere and surface, and given these properties as described above, we compute it using an efficient adding–doubling algorithm (de Haan et al., 1987) that fully includes linear and circular polarization for all orders of scattering.

To numerically simulate the observations, we represent Venus' disk with a grid of equally sized, square pixels. For each pixel, we compute the Stokes vector $\mathbf{F}$ (see Eq. 3.1)

Table 3.3: The parameters of our standard Venus model atmosphere, addressing the layers from top to bottom: p_{bot} and p_{top} are the standard pressures at the bottom and the top of each layer, N^m is the standard gas column number density based on the pressure range across each layer, b^m is the gaseous optical thickness of the layer at 580 nm, the central wavelength of the Na cont. filter (see Table 3.1), and b^a is the cloud or haze optical thickness of the layer, also at 580 nm. Layer 2 contains the cloud and layer 3 contains the haze (see Table 3.2 for the values at other wavelengths). The single scattering albedo's of the gaseous molecules, ω^m, and that of the cloud and haze particles equals 1.0 in each layer and at each wavelength. The variations in the gas column number density that give rise to the concentric rings in the polarization are imposed on the highest atmospheric layer, thus the layer with p_{bot} = 0.005 bars and p_{top} = 0.0 bars.

Layer	p_{bot} (bars)	p_{top} (bars)	N^m (m^{-2})	b^m(580 nm)	b^a(580 nm)
4	0.005	0.0	7.713e26	0.000794	0.0
3	0.05	0.005	6.942e27	0.00650	0.02
2	1.0	0.05	1.466e29	0.137	30.0
1	93.0	1.0	1.419e31	13.283	0.0

of the locally reflected sunlight with wavelength λ, according to

$$\mathbf{F}(\lambda,\theta,\theta_0,\phi-\phi_0) = \cos\theta_0\ \mathbf{R}(\lambda,\theta,\theta_0,\phi-\phi_0)\ \mathbf{F}_0(\lambda), \tag{3.17}$$

where θ_0 is the local solar zenith angle, θ the local zenith viewing angle, and $\phi-\phi_0$ the local azimuthal difference angle (de Haan et al., 1987). Vector $\mathbf{F}_0$ is the incident sunlight, and $\mathbf{R}$ is the local planetary reflection matrix. All angles are computed by projecting the center of each pixel onto a 3D–sphere that represents Venus. Note that while θ and ϕ depend on the position of the projected center of each pixel with respect to the sub–observer point on the sphere, θ_0 and ϕ_0 depend on the position of the projected center of each pixel with respect to the sub–solar point, the location of which depends on Venus' phase angle α, which equaled 48.7° at the time of our observations.

The reflected fluxes as computed using Eq. 3.17 do not need further scaling because the pixels all have the same size. The lack of absolute calibration of our observed total and polarized fluxes, precludes an attempt to absolutely fit the computed fluxes. The degree of polarization (Eq. 3.2) is a relative measure and as such it is in principle insensitive to e.g. changes in the airmass during the observational cycle. While the measurements by ExPo have a very high polarimetric sensitivity reaching 10^{-4} (Rodenhuis et al., 2012), the absolute calibration of the degree of polarization of our observations, however, is only 1 - 2% because of the lack of polarized standard stars at the time of our observations. In other words, the absolute off–set of the degree of polarization is on the order of 1 - 2% ($P_{\text{observed}} = P_{\text{Venus}} \pm 1-2\%$). As we will show below, this off–set does not limit our numerical simulations of the observations, as those are based on the spatial variability of P and not on its absolute value.

3.4. EXPLAINING THE RINGS OBSERVATION

The degree and direction of polarization of sunlight that is reflected by a region on a planet depends strongly on the optical properties of the scattering particles, on the illumination and viewing geometries, and on the ratio of singly to multiply scattered light (Hansen and Travis, 1974), as the former can be highly polarized while the latter usually has a low degree of polarization. Because of the large distances between Venus and the Sun and between Venus and Earth, and given the phase angle of 48.7°, the singly scattered photons that ExPo received from locations across Venus' disk have been scattered across an angle of 131.3°. If the rings were due to variations in the microphysical properties of the scattering haze and/or cloud particles in the atmosphere, such as their size or composition, these variations should appear in a similar, concentric planet–wide pattern and they should be small enough to virtually leave no trace in the total flux. This seems difficult to explain with our knowledge of the composition and structure of the clouds and hazes in Venus' atmosphere. The rings could also be due to variations in the local number densities of haze and/or cloud particles, as such variations would change the ratio of singly to multiple scattered light. However, the known, latitudinal variations in the cloud and haze properties (notably, cloud top altitude (Ignatiev et al., 2009) and haze optical thickness (Kawabata et al., 1980; Sato et al., 1996; Rossi et al., 2015)) seem to preclude the appearance of the observed, concentric, planet–wide patterns.

The regularity of the polarization pattern and the fact that it seems to overlay the high polarization polar regions, indicates an origin in Venus' upper atmosphere, and

the most straightforward explanation appears to be density variations of the gas in that region of the atmosphere. Such planet–wide density variations could result from atmospheric waves emanating from the region close to the sub–solar point, as we will discuss later. Small, local density variations in the gas above the hazes and clouds will yield small variations in the amount of locally reflected sunlight, particularly in the amount of light that has been singly scattered by gas molecules, which has a relatively high degree of polarization at a scattering angle of 131.3° (see Fig. 3.6 for a detailed explanation), with a direction perpendicular to the scattering plane, i.e. opposite to that of the clouds.

3.4.1. NUMERICALLY REPRODUCING THE RINGS

Figure 3.7 shows numerical simulations of the flux and degree of polarization along Venus' equator at a planetary phase angle of 48.7°. For the computations, we varied N^{m}, the gas column number density (in m^{-2}) in the highest atmospheric layer. The dashed lines in Fig. 3.7 represent the flux and polarization of the reflected sunlight without gaseous density variations. A negative degree of polarization P indicates a polarization direction parallel to the scattering plane. The reflected flux appears to be virtually insensitive to variations in N^{m}, just like we observed. However, increasing N^{m} decreases P (the light becomes more unpolarized), while decreasing N^{m} increases P (the light becomes more, negatively, polarized). Indeed, the computed variations in P are within ExPo's sensitivity and, even though the direction of polarization of the light scattered by the molecules is perpendicular to the reference plane and thus counteracts the polarization direction of the clouds and hazes, the direction of polarization across the variations remains parallel to the reference plane, like in the observations.

The variations in P are independent of the precise vertical location of the density variations, except that they should be in the upper region of the atmosphere, where the scattering is dominated by the gas. The decrease of the scattering–cross section of the gas molecules with wavelength (see Hansen and Travis (1974) and Sec. 3.3) causes the decrease of the sensitivity of P to the density variations. This sensitivity decrease could explain the lack of rings in the longer wavelength filters, such as the Sloan i filter, in addition to the larger airmass and worse seeing conditions during those observations (see Table 3.1). We did not optimize the clouds and hazes in our model atmosphere to fit the background flux and polarization in the ExPo observations, because, as mentioned earlier, the absolute accuracy of the polarization observations is limited to 1-2 %. This, however, poses no problem for our interpretation, because the absolute change in P due to a small change in N^{m} appears to be insensitive to the background polarized flux as it adds mostly singly scattered light, which does change the reflected polarized flux, but hardly changes the total flux.

Figure 3.8 shows numerical simulations of the total flux, degree and direction of polarization across Venus' disk in the H-alpha filter with the density variations chosen to be concentric around the region close to the sub–solar point. For these simulations, the planet was assumed to be horizontally homogeneous except for the gas column number density in the upper atmospheric layer (the cloud and haze macro and micro-physical properties are thus the same everywhere). A sinusoidal variation in the gas column number density was spatially introduced to model the effect of a density wave travelling through the upper atmosphere of Venus. The amplitude of this variation was 10 %

of the computed column gas density pertaining to this top most atmospheric layer. This spatial plot of Venus clearly conveys the points made above that the variation in density just on the upper atmospheric layer by 10 % produces a significant variation in P but not F.

3.5. DISCUSSION AND CONCLUSION

We have shown that we can numerically simulate the concentric rings across Venus' disk that appear in our high–accuracy, spatially resolved ExPo observations of the degree of polarization of reflected sunlight by assuming density variations in the atmospheric gas above the clouds and hazes. Similar to the observations, the density variations do not leave a significant signal in the reflected total flux. The density variations required to reproduce our observations are ± 5% - 10%, above the cloud and haze layers (i.e. above 0.036 bars). Such density variations in the gas above the clouds and hazes could be due to so far unknown planet–wide atmospheric waves that would be excited in the cloud tops about 20° (2100 km) downwind from the sub-solar point (corresponding to a local time of roughly 13:00 h).

This displacement with respect to the sub-solar point could be the result of a combination of a time lag in the maximum heating of the cloud layer (Belton et al., 1976) and the large equatorial wind velocities, on the order of 100 m/s (Counselman et al., 1980; Limaye and Suomi, 1981; Newman et al., 1984; Moissl et al., 2009) that move the clouds away from the sub-solar point. The waves could be propagating across the planet in the direction of the anti-solar point, possibly within the known sub-solar to anti-solar flow (Goldstein et al., 1991; Bougher et al., 1997). According to the spatial resolution of the observations, the horizontal wavelength of the waves would be between 100 km and 1000 km, decreasing with distance from the excitation region.

In-situ measurements taken over 600 orbits, between about 160 and 200 km altitude by the ONMS instrument on Pioneer Venus orbiter revealed waves (variations in gas density) in various regions on the planet (Kasprzak et al., 1988). These waves, with wavelengths of 100–600 km were tentatively identified as gravity waves (Mayr et al., 1988). Interestingly, the Pioneer Venus measurements showed little wave activity towards the sub-solar region and increasing wave activity towards the morning and evening terminators, which agrees well with our ground-based observations. A planet-wide propagation was suspected for these waves (Mayr et al., 1988), although this could not be confirmed from Pioneer Venus' along-track data available at the time.

Because this is our only set of Venus observations with ExPo, we don't know how often these waves occur. But if these are indeed the same waves as the upper atmospheric density waves observed by Pioneer, they might be a regularly occurring phenomenon. More observations, with ground-based telescopes and/or from a future orbiter outfitted with highly sensitive polarimeters, should be performed to get insight into their appearance and variations therein.

Our numerical simulations show (cf. Fig. 3.7) that there would be no need for high–spectral resolution polarimetry to observe the rings. The absence of the rings in ExPo's broadband observations could be explained by the decreased spatial resolution due to the large airmass at the time. Fig. 3.9 illustrates the effect of introducing atmospheric effects to the measured polarized fluxes. We have used an atmospheric phase screen that

is able to accurately model the effects of the atmosphere (Buscher, 2016; Mortimer, 2023) at various viewing geometries which is parametrised through the variable S and referred to as the atmospheric seeing. S determines the extent of the signal attenuation as a function of the atmospheric turbulence and viewing geometry. Thus, the atmospheric seeing S can be understood as the effect of the atmospheric turbulence affecting the light arriving at the ground based telescope specified at a wavelength of 500 nm. The incoming orthogonally polarized flux signals is propagated through the phase screen for different values of S and the individual Stokes fluxes F and Q are computed by combining the orthogonal polarized flux values. We compute P as $-Q/F$. Since phase screens are random in nature, we generated a phase screen for each seeing condition with the telescope azimuth angle fixed at 45° and the telescope diameter and focal length corresponding to that of Isaac Newton Telescope with the values being 2.54 m and 8.36 m respectively. The first column in Fig. 3.9 shows the planet with no atmosphere, hence $S = 0$ and the density wave rings are clearly visible in Q. The second column has a $S = 0.5$ with the rings getting fainter as a result and the rings fully disappear at $S = 1.5$. Fig. 3.10 clearly shows this effect of the atmosphere leading to the attenuation of the density waves completely because of the increased airmass or seeing. While modelling the blurring due to low atmospheric seeing accurately is out of the scope of this work, these computations demonstrate the possibility of the density waves not being visible in a high airmass scenario when Venus was getting low in the horizon.

Our simulations also show that the rings should be easiest to observe at phase angles around 90° (our observations pertain to 48.7°), because there the difference between the degree of polarization of light singly scattered by gaseous molecules and the background polarization is largest (see the Additional materials section). To confirm the ring–like shape of the pattern, observations at either smaller phase angles than ours (where the strength of the pattern would, however, be smaller), or of Venus' morning hemisphere (our observations mostly cover the afternoon-evening hemisphere) are required. With more observations, combined with a suitable numerical model for Venus' tenuous upper atmosphere, would undoubtedly provide insight into the physical characteristics of the waves and their environment, and into their role in the various dynamical processes in the atmosphere of Venus.

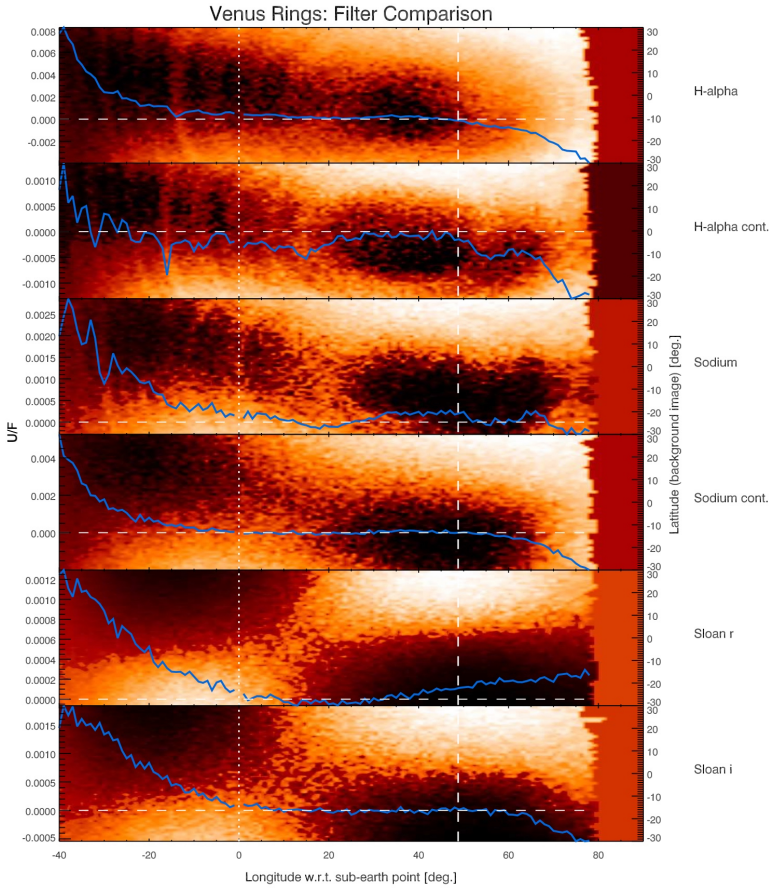

Figure 3.3: The background (red-orange colors) shows the degree of polarization as a function of longitude with respect to the sub–observer point (horizontal axis) and the latitude from -30° to +30° on Venus (vertical axis) as measured in the various filters, with the time of observation increasing from top to bottom (see Table 3.1). The blue line shows the degree of polarization averaged over the latitudes between -5° and +5° as a function of longitude with respect to the sub–observer point (scale on the left). The degree of polarization shown equals U/F, with U defined with respect to the instrumental optical plane. Because the orientation of the planet with respect to this plane is almost equal to 45°, Stokes parameter U in the instrumental optical plane corresponds almost to Stokes parameter Q in the planetary scattering plane. The difference between the planetary scattering plane and the instrumental optical plane is 3-5°. The rings are much less visible in Stokes parameter Q defined with respect to the instrumental optical plane (and, hence, they are much less visible in Stokes parameter U as defined with respect to the planetary scattering plane), indicating that the direction of polarization of the background signal and the rings is mostly parallel to the planetary scattering plane (see Fig. 3.4). The vertical dotted line indicates the sub-observer or sub-earth longitude, and the vertical dashed line the sub-solar longitude. The horizontal long-dashed line indicates the zero polarization level for the blue lines. Note that because of the lack of accurate absolute calibration, this blue line and the zero level have an uncertainty of 1-2%. The shape of the continuum polarization is also influenced by the difference between the planetary scattering plane and the instrumental optical plane.

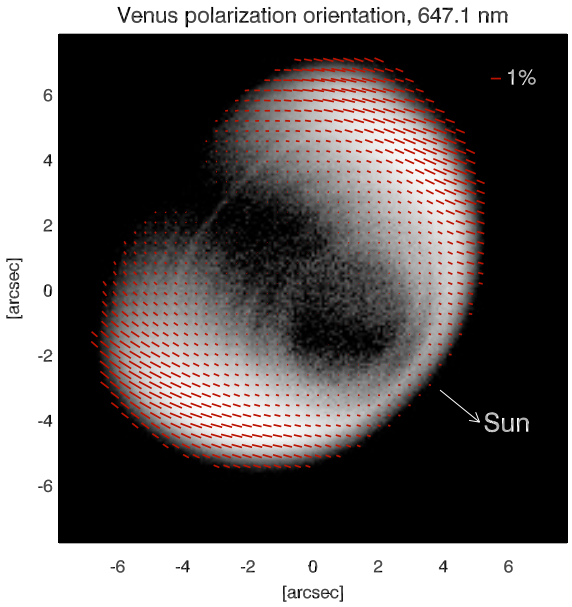

Figure 3.4: The direction of polarization as measured using the H-alpha cont. filter (λ_0 = 647.1 nm). The orientation of the red lines indicates the polarization direction (note that the direction is not shown for every pixel to avoid cluttering), and the line length indicates the local degree of polarization, which is predominantly determined by the polarization signal of the lower atmospheric layers that contain the hazes and clouds.

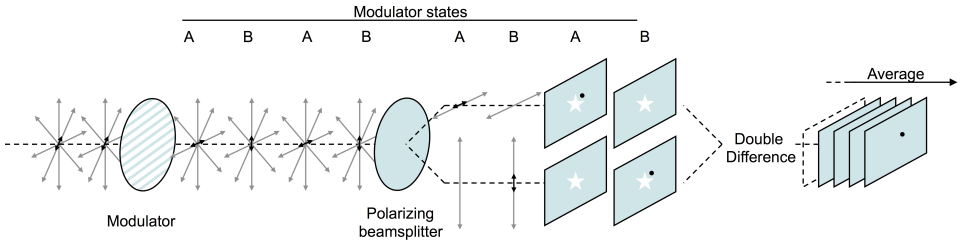

Figure 3.5: ExPo's dual-beam exchange polarimetry technique.

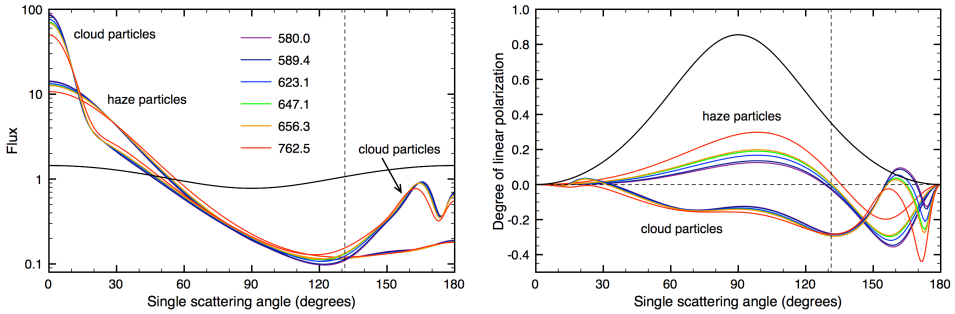

Figure 3.6: The flux (left) and degree of linear polarization P (right) of incident unpolarized light that is singly scattered by the cloud particles, haze particles, and gaseous molecules (solid black line) at the central wavelengths of the filters. Note that the wavelength dependence of the molecular scattering (through the depolarization factor, see Eq. 3.10) is so small that we show only one line. All flux curves are normalized such that averaged over all scattering directions equals 1.0. A positive P indicates a direction of polarization perpendicular to the scattering plane (the plane containing the incident and scattered light beams) and a negative P, a direction parallel to the scattering plane. The black, dashed vertical lines indicate the single scattering angle that corresponds with the phase angle of Venus at the time of our observations, and the black, dashed horizontal line in the polarization plot, $P = 0$.

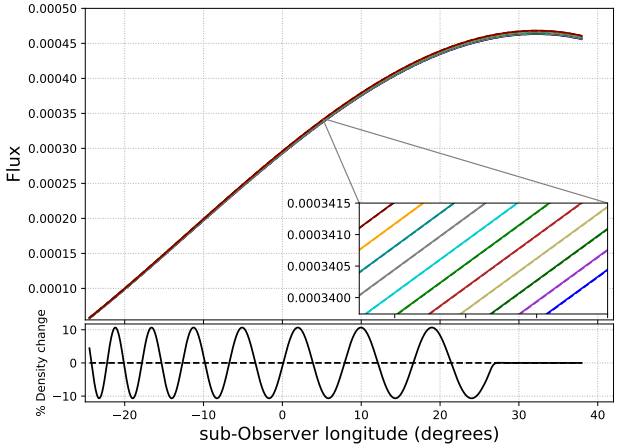

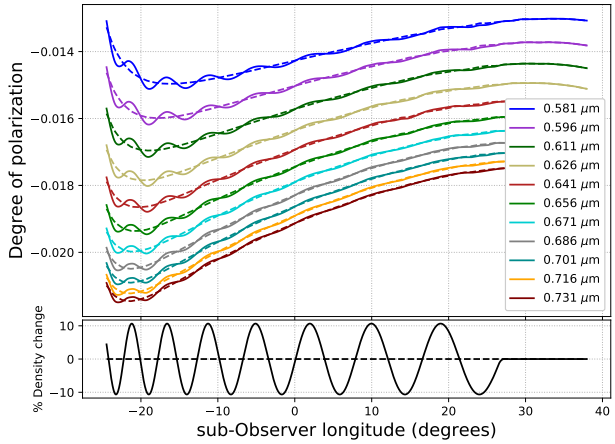

Figure 3.7: The total flux (left) (normalized such that at a phase angle of 0°, the disk–integrated flux equals the planet's geometric albedo) and degree of linear polarization (right) along Venus' equator in response to a change in the gas column number density N^{m} of the upper atmospheric layer for wavelengths covered by the filters (see Table 3.1). The composition and structure of the lower atmospheric layers (with cloud and haze particles) are the same at every longitude. The dashed lines pertain to the baseline value of N^{m}, i.e. 5.0×10^{27} molecules m^{-2} (for the atmosphere up from 70 km or down to 0.036 bars). The negative sign of the degree of polarization indicates a direction parallel to the planetary scattering plane (and the equator).

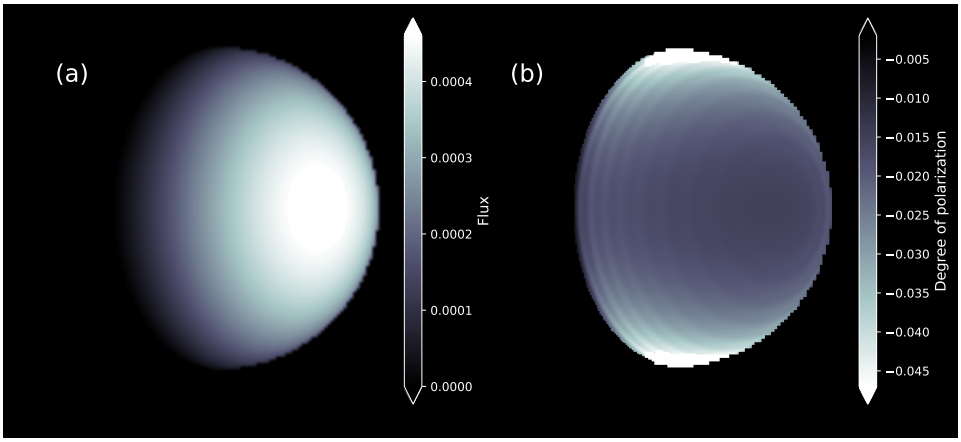

Figure 3.8: Numerical computations of our Venus observations in the H–alpha filter (λ_0 = 656 nm), for the total flux (left) and the polarized flux (right). The background polarization signal has been subtracted from the latter. The decrease in spatial resolution due to the Earth's atmosphere is not included. The planetary atmosphere is assumed to be horizontally homogeneous except for the gas density variations.

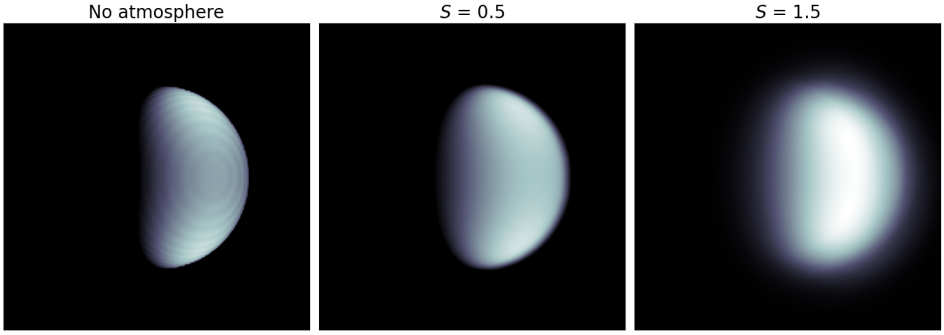

Figure 3.9: Numerical computations of the polarized flux Q because of the introduction of atmospheric seeing S in our Venus model computations in the H–alpha filter (λ_0 = 656 nm). The planetary atmosphere is assumed to be horizontally homogeneous except for the gas density variations. Atmospheric blurring is applied to fluxes in orthogonally polarized states and then recombined to get F and Q. P is computed as per eqn. 3.4. Columns 2 and 3 show blurred planets with the seeing parameter increasing such as S=0.5 and S=1.5 respectively. Telescope's zenith angle is fixed at 45° and the telescope diameter and focal length's are corresponding to that of Isaac Newton Telescope with the values being 2.54 m and 8.36 m respectively.

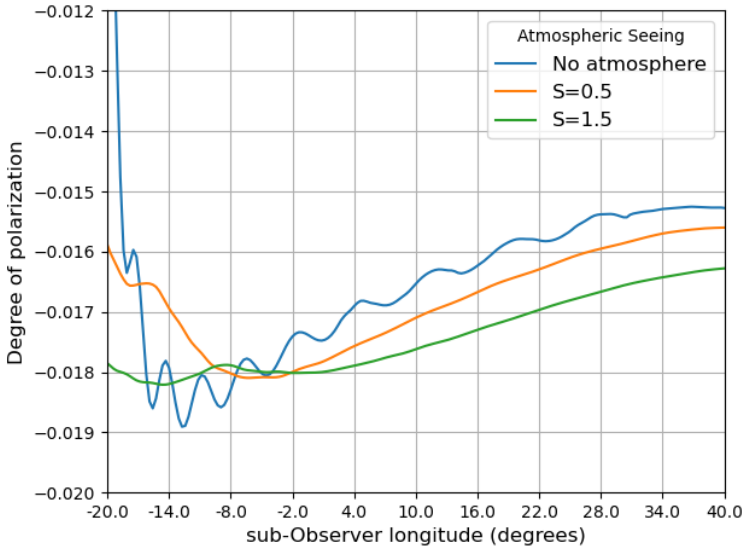

Figure 3.10: 1D Numerical computations of introducing atmospheric seeing S effect in our Venus model computations in the H–alpha filter (λ_0 = 656 nm), for the degree of polarization P. The planetary atmosphere is assumed to be horizontally homogeneous except for the gas density variations. The decrease in the wave amplitude and attenuation is clearly visible with increasing S.

4

FLUXES AND POLARIZATION OF SUNLIGHT REFLECTED BY VENUS ACROSS CO_2 ABSORPTION BANDS

GOURAV MAHAPATRA, LOÏC ROSSI, DAPHNE M. STAM

We present computed total and polarized fluxes of sunlight reflected by Venus in the wavelength region between 1.4 and 1.5 μm, which contains absorption bands by CO_2, and for various cloud and haze vertical profiles. This forward modelling is done to determine if the degree of polarization derived from SPICAV-IR instrument on-board the Venus Express mission contains useful information about the clouds and/or hazes in the CO_2 absorption bands. We specifically test whether parameters such as cloud top altitude, cloud scale height and haze optical thickness can be retrieved from this data. We also perform this study to find if prospective future missions to Venus should observe in this wavelength region. We use the fast but approximate correlated-k distribution method and also show errors that arise due to this approximation for various scenarios. Through a sensitivity analysis, we show that the polarized flux with different strength of absorption, is sensitive to the atmospheric aerosol structure and width of the instrument response, which is due to the decrease of multiple scattering in the presence of absorption and the vertical variation of the single scattering properties from cloud/haze particles. Finally we perform a qualitative analysis of degree of polarization data from SPICAV-IR instrument and show that the signal despite being noisy, is in good agreement with past findings of cloud top altitude and haze optical thickness.

4.1. INTRODUCTION

The SPICAV (SPectroscopy for Investigation of Characteristics of the Atmosphere of Venus) instrument onboard ESA's Venus Express mission (Korablev et al., 2012) has provided a wealth of information on Venus' atmosphere (Wilquet et al., 2009; Marcq et al., 2011; Belyaev et al., 2012; Luginin et al., 2016; Rossi et al., 2015; Fedorova et al., 2016). SPICAV had three spectral channels covering, respectively, ultra-violet, near-infrared, and infrared wavelengths to study the atmosphere of Venus from the lowest altitudes to the highest (Korablev et al., 2012). The NIR-channel (referred to as SPICAV-IR) covered wavelengths from 650 to 1700 nm and used an acousto-optic tunable filter (AOTF) in which a bi-refringent crystal splits the incoming light into two orthogonally polarized beams. The UV and IR channels used a grating spectrometer and an echelle-spectrometer respectively.

Light reflected from a planetary atmosphere in the gaseous absorption bands, contain unique altitude dependent aerosol information provided the atmospheric constitu-

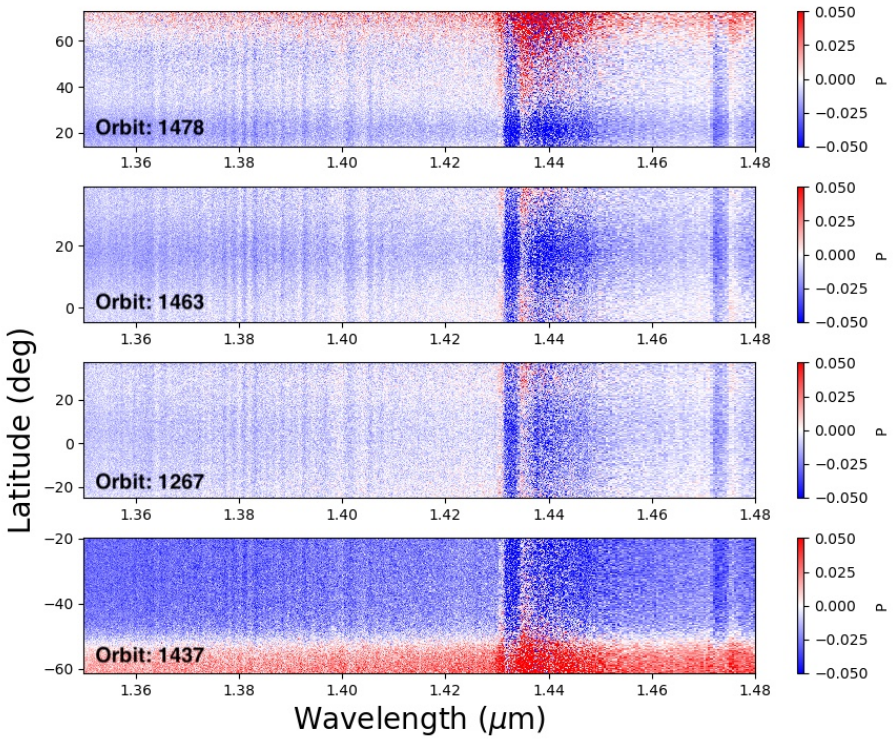

Figure 4.1: Degree of polarization P of light reflected by Venus derived from the two orthogonally polarized channels of SPICAV-IR, as functions of the wavelength, and as functions of the latitude. The four panels pertain to four sample orbits as follows: 1478, 1463, 1267, 1437. Positive (red) polarization refers to a polarization direction perpendicular to the scattering plane, while negative (blue) polarization refers to a direction parallel to this plane. The vertical streak-like patterns in the plots correspond to numerous absorption lines.

tion itself is vertically inhomogeneous and the mixing ratio of the gas is homogeneous (which is the case with Venus). Theoretical simulations for sunlight that is scattered and reflected by the Earth's atmosphere (Stam et al., 1999; Boesche et al., 2009) predict deviation of degree of polarization P across the absorption bands as compared to the continuum. Two effects that play a role have been identified: 1. in the presence of absorption, less multiple scattered light, with usually a relatively low degree of polarization, emerges from the top of the atmosphere, and 2. if the optical properties of atmospheric particles vary with the altitude, the light observed inside the absorption band is scattered by different types of particles than the light observed at continuum wavelengths. High-spectral resolution P measurements contain information on the aerosol characteristics, depending on the absorption line strength. Such fine lines have been previously observed on Venus with a very high resolution ground-based Fourier spectropolarimetry instrument (Forbes and Fymat, 1974) , albeit as a function of angular fluxes.

SPICAV-IR was not designed to perform polarimetry of Venus, but the orthogonally polarized beams enabled the derivation of Stokes components F and Q (Stokes U and V are not accessible to SPICAV-IR). Rossi et al. (2015) used the continuum polarization measured by SPICAV-IR to derive cloud microphysical properties (particle refractive index, and the effective radius and effective variance of the particle size distribution) and found a good agreement with values derived from ground-based and satellite-based observations (Hansen and Hovenier, 1974; Travis et al., 1979; Kawabata et al., 1980). They also found that the optical thickness of hazes required to explain the derived high degree of polarization, was greater towards the poles than at the equator, which was in good agreement with polarimetric measurements carried out by the Pioneer Venus mission (Kawabata et al., 1980).

Figure 4.1 shows the degree of polarization as derived from SPICAV-IR's data along four orbits, between 1350 and 1480 nm, a wavelength region with a relatively strong CO_2 absorption bands around 1.44 μm. The orbits cover latitudes ranging from about -60° to +60°, and were thus chosen because of their relatively large latitudinal coverage. From the figure, it is clear that the absolute value of P is mostly larger inside the absorption bands than in the adjacent continuum. Another notable feature is that P changes sign from negative to positive towards the poles (latitudes > 60° and <-50°) in the continuum and in the strongest band (see orbits 1478 and 1437). Because SPICAV-IR was not designed to measure polarization, it was, unfortunately, not well-calibrated for polarimetry, and consequently the signal to noise ratio is low (SNR ~50) at the long wavelength (1.3 - 1.5 μm) region (Korablev et al., 2012).

Our aim with this paper is to investigate how these effects influence variations of P across CO_2 absorption bands in sunlight that is reflected by Venus. In order to be able to extract useful information contained in the observations and minimise the effect of noise, we make use of the relative measures (difference) in the value of P at the continuum and at a region of strong absorption. This also eliminates the need for absolute calibration of P in the observations. Radiative transfer computations including polarization for all orders of scattering and across gaseous absorption bands can be extremely time consuming when using the so-called line-by-line method (lbl-method), in which the spectral resolution of the computations is high enough to resolve individual absorption lines. Instead, we use the approximate correlated-k distribution method (ck-

method) (Fu and Liou, 1992; Lacis and Oinas, 1991). The ck-method has been used for radiative transfer computations of reflected or thermally emitted fluxes across various wavelength regions for Venus (Bullock and Grinspoon, 1996; Koukouli et al., 2005; Irwin et al., 2008; Tsang et al., 2008; McGouldrick and Toon, 2008; Barstow et al., 2012). The errors due to the ck-method's approximations in the polarization are however different than those in the total fluxes, as shown for the Earth atmosphere and the oxygen A-band by Stam et al. (2000). We will therefore also evaluate the accuracy of the ck-method for the polarization computations across Venus' CO_2 absorption bands.

The outline of this paper is as follows. In Sect. 4.2, we describe our numerical algorithm to compute reflected total and polarized fluxes across CO_2 absorption bands, including the model Venus atmosphere. Section 4.3 contains the computed reflected fluxes and polarization. In Sect. 4.4, we present a retrieval of Venus' cloud and haze properties as derived from SPICAV-IR polarization data. Section 4.5 contains our conclusions.

4.2. Description of our numerical algorithm

4.2.1. Definitions of fluxes and polarization

We use Stokes (column) vectors to describe the incident and reflected sunlight (Hansen and Travis, 1974) as follows

$$\mathbf{F}(\lambda) = [F(\lambda), Q(\lambda), U(\lambda), V(\lambda)], \tag{4.1}$$

with F the total flux, Q and U the linearly polarized fluxes, and V the circularly polarized flux, all with dimension W/m^2 and dependent on wavelength λ. We assume the sunlight that is incident on Venus to be unidirectional and unpolarized (Kemp et al., 1987, e.g.). The linearly polarized fluxes Q and U of the reflected sunlight are defined with respect to the local meridian plane, which contains the directions towards the local zenith and the observer. Because our model atmosphere is locally horizontally homogeneous (see Sect. 4.2.2), U and V of the reflected light are both zero. In our radiative transfer computations, we ignore V, because this significantly speeds up the computations while it hardly influences the accuracy of the computed total and linearly polarized fluxes (Stam and Hovenier, 2005). Because U of the reflected light is zero, we define the degree of polarization P of the reflected light as

$$P(\lambda) = -\frac{Q(\lambda)}{F(\lambda)}. \tag{4.2}$$

When $P > 0$ ($P < 0$), the direction of polarization is perpendicular (parallel) to the local meridian plane. The local direction of reflection, i.e. the light that is received by the observer (e.g. an instrument onboard an orbiter), is described by θ which is the angle between the direction to the observer and the local vertical, and ϕ, the azimuthal angle of the reflected light. Because our model atmosphere is rotationally symmetric around the local vertical (see Sect. 4.2.2), only the azimuthal angle difference $\phi - \phi_0$ is important. We define it such that $\phi - \phi_0 = 0^\circ$ (180°) when the propagation directions of the incident sunlight and the reflected light are in the same (opposite) half of the local vertical plane.

4.2.2. THE OPTICAL PROPERTIES OF THE MODEL ATMOSPHERE

The model atmosphere is composed of a stack of horizontally homogeneous layers containing CO_2 gas, and, optionally, cloud or haze particles. It is bounded below by a black surface (because of the thickness of the atmosphere, our results are virtually insensitive to the surface reflection). Our adding-doubling radiative transfer algorithm (de Haan et al., 1987) requires for each atmospheric layer: the single scattering matrix, the single scattering albedo, and the total optical thickness. The total optical thickness b of a layer is the sum of the scattering and absorption optical thicknesses as follows

$$b(\lambda) = b_{\rm sca}(\lambda) + b_{\rm abs}(\lambda) = b^{\rm m}_{\rm sca}(\lambda) + b^{\rm a}_{\rm sca}(\lambda) + b^{\rm m}_{\rm abs}(\lambda) + b^{\rm a}_{\rm abs}(\lambda), \tag{4.3}$$

with superscripts 'm' and 'a' denoting the gas and the aerosol particles (i.e. cloud and/or haze particles), respectively. The single scattering albedo is given by

$$a(\lambda) = \frac{b^{\rm m}_{\rm sca}(\lambda) + b^{\rm a}_{\rm sca}(\lambda)}{b(\lambda)}. \tag{4.4}$$

We calculate $b^{\rm m}_{\rm sca}$ of an atmospheric layer using Stam et al. (1999)

$$b^{\rm m}_{\rm sca}(\lambda) = \frac{24\pi^3}{\lambda^4 N_{\rm L}^2} \frac{(n^2(\lambda)-1)^2}{(n^2(\lambda)+2)^2} \frac{(6+3\rho_n(\lambda))}{(6-7\rho_n(\lambda))} \frac{N_{\rm av}}{R} \int_{z_i}^{z_{i+1}} \frac{p(z)}{T(z)} dz, \tag{4.5}$$

where $N_{\rm L}$ is Loschmidt's number, $N_{\rm av}$ Avogadro's number, R the universal gas constant, and n the refractive index of the atmosphere, which we assume to consist entirely of CO_2 and we thus use $n = 1.0004$ between 1.4 and 1.5 μm (Bideau-Mehu et al., 1973). The depolarization factor ρ_n equals 0.09 (see Hansen and Travis, 1974). Furthermore, p is the ambient pressure, T the ambient temperature, and z_i and z_{i+1} are the altitudes at the bottom and top of the atmospheric layer, respectively. We use the pressure and temperature profile representative for a latitude of 30° (Seiff et al., 1985), and a geometric layer thickness of 4 km until $z = 40$ km, and 1 km above for a total of 71 layers.

The gaseous absorption optical thickness, $b^{\rm m}_{\rm abs}$, of an atmospheric layer is calculated according to

$$b^{\rm m}_{\rm abs}(\lambda) = \frac{N_{\rm av}}{R} \int_{z_i}^{z_{i+1}} \frac{p(z)}{T(z)} \sigma^{\rm m}_{\rm abs}(\lambda, z) dz, \tag{4.6}$$

with $\sigma^{\rm m}_{\rm abs}$ the gaseous absorption cross-section, which we calculate using HITRAN16 absorption line data (Gordon et al., 2017). Figure 4.2 shows the atmospheric absorption optical thickness, i.e. the sum of $b^{\rm m}_{\rm abs}$ across all atmospheric layers across the wavelength region of our interest, $b^{\rm abs}$ of a 2-km thick layer around 65 km, and the atmospheric gaseous scattering optical thickness, i.e. the sum of $b^{\rm m}_{\rm sca}$ across all layers.

For efficient computations of the flux and polarization across the CO_2 absorption bands as shown in Fig. 4.2, we use the correlated k-distribution method (the 'ck-method') (Lacis and Oinas, 1991; Fu and Liou, 1992; Stam et al., 2000). In this method, the strongly wavelength dependent absorption cross-sections across an instrumental spectral response function are redistributed according to their strength, such that the number of radiative transfer computations required to cover the resulting distribution function is much smaller than required by the line-by-line method (the 'lbl-method').

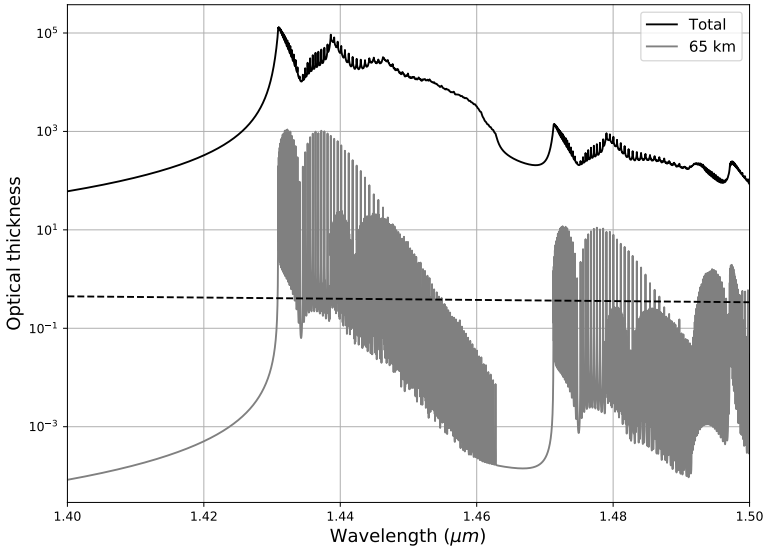

Figure 4.2: Atmospheric gaseous absorption optical thickness (upper solid line), the gaseous absorption optical thickness of a 2-km thick atmospheric layer around 65 km altitude (lower solid line), and the atmospheric gaseous scattering optical thickness (dashed line), which is about 0.4.

A key assumption in the ck-method is that the absorption line cross-sections at different altitudes in the atmosphere are correlated in the spectral domain. In particular in the presence of scattering, this assumption leads to errors in the computed reflected fluxes and polarization. The errors depend on the actual vertical variation of the absorption cross-sections, on the spectral region under consideration, and on the vertical distribution of the scattering particles (Stam et al., 2000). In Sect. 4.7, the errors due to the assumptions of the ck-method for the numerical simulations presented in this paper are discussed.

The single scattering matrix $\mathbf{P}^{\mathrm{m}}$ of the CO_2 gas is the anisotropic Rayleigh scattering matrix (Hansen and Travis, 1974). The single scattering phase function, P_{11}, and the single scattering degree of polarization for unpolarized incident light, $-P_{21}/P_{11}$, of the gas are shown in Fig. 4.3.

The cloud and haze particles are spherical and homogeneous. We assume their refractive index to be 1.40, which is representative for 75 % sulfuric acid (H_2SO_4) at 1.45 μm (Palmer and Williams, 1975). Their single scattering albedo, a^{a}, is thus one. We describe the sizes of the cloud and haze particles by log-normal distributions with a modal radius r_{g} and variance σ. For the cloud particles, we use the micron-sized "mode 2" particles, with $r_{\mathrm{g}} = 1.05$ μm and $\sigma = 1.21$, and for the haze particles, the sub-micron sized "mode 1" particles, $r_{\mathrm{g}} = 0.15$ μm and $\sigma = 1.91$ (Fedorova et al., 2016). The lower cloud region (below 60 km) should also have the so–called "mode 3" particles (Knollenberg and Hunten, 1980) with sizes of ~ 4 μm, but we neglect these particles, as the traces they leave in the reflected light are negligible.

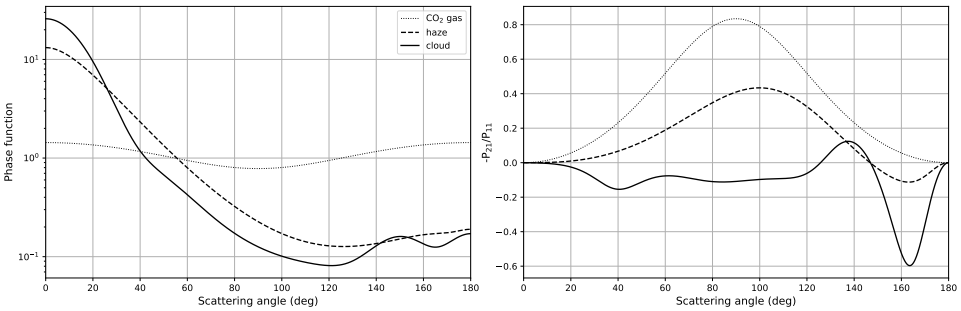

Figure 4.3: The phase functions (left) and degree of linear polarization (right) for incident unpolarized light that is singly scattered by the cloud particles (solid lines), the haze particles (dashed lines) at $\lambda = 1.45$ µm, and the CO_2 gas (dotted lines). The average of each phase function over all scattering directions equals 1.0 (Hansen and Travis, 1974).

The extinction cross-section $\sigma^{\mathrm{a}}_{\mathrm{ext}}$ and the single scattering matrix $\mathbf{P}^{\mathrm{a}}$ of the cloud and haze particles are computed using a Mie-algorithm (De Rooij and Van der Stap, 1984). Figure 4.3 shows the single scattering phase functions and degree of linear polarization for unpolarized incident light of the cloud and haze particles at $\lambda = 1.45$ μm. The aerosol optical thickness b^{a} of an atmospheric layer is computed using

$$b^{\mathrm{a}}(\lambda) = \sigma^{\mathrm{a}}_{\mathrm{ext}}(\lambda) N^{\mathrm{a}} dz, \tag{4.7}$$

with N^{a} the aerosol particle number density (in m^{-3}) across the layer. Because the single scattering albedo is one, $b^{\mathrm{a}}_{\mathrm{sca}} = b^{\mathrm{a}}$.

Figure 4.14 shows the vertical distribution of aerosols as a function of their particle number density N^{a}. N^{a} is assumed to be constant between altitudes z_{bot} and z_{cut}, and subsequently decreases exponentially with altitude, as follows

$$N^{\mathrm{a}} = N_0 \exp\left(-\frac{z - z_{\mathrm{cut}}}{H}\right) \tag{4.8}$$

with N_0 the (constant) number density below z_{cut}, H the aerosol scale height (in km), z the altitude of the middle of an atmospheric layer. For the clouds, we furthermore use the cloud-top altitude z_{top}: the altitude at which the total cloud optical thickness reaches 1.0 as measured from the top of the atmosphere. Because the cloud optical thickness depends on the wavelength, z_{top} also depends on the wavelength. Details about the aerosol profile are given in 4.7. Lastly, the single scattering matrix pertaining to an atmospheric layer containing a mixture of gas and aerosol is given by

$$\mathbf{P}(\lambda) = \frac{b^{\mathrm{m}}_{\mathrm{sca}}(\lambda)\mathbf{P}^{\mathrm{m}}(\lambda) + b^{\mathrm{a}}_{\mathrm{sca}}(\lambda)\mathbf{P}^{\mathrm{a}}(\lambda)}{b_{\mathrm{sca}}(\lambda)}. \tag{4.9}$$

4.3. RESULTS

Given the strong spectral variations of the gaseous absorption (see Fig. 4.2), the total flux F and degree of polarization P of the sunlight that is reflected by Venus will also show strong spectral variations. An instrument like SPICAV-IR has a spectral resolution of ~0.001 μm in its long-wavelength (1.05 - 1.7 μm) spectral region (Korablev et al., 2012), which is not enough to resolve individual absorption lines. To understand measurements such as those by SPICAV-IR across gaseous absorption bands, understanding the underlying high-spectral resolution variation is important. We therefore first present F and P of reflected sunlight as functions of the atmospheric absorption optical thickness $\sum b^{\mathrm{m}}_{\mathrm{abs}}$ (Sect. 4.3.1) and then as functions of the wavelength for various instrument response functions (Sect. 4.3.2). Finally we conduct a sensitivity analysis of our model parameters at three wavelengths in the absorption band (Sect. 4.3.3).

4.3.1. F AND P AS FUNCTIONS OF $\sum b^{\mathrm{m}}_{\mathrm{abs}}$

Figure 4.4 shows F and P as functions of $\sum b^{\mathrm{m}}_{\mathrm{abs}}$ (see Fig. 4.2). To cover a range from zero to 10^4, we multiply $b^{\mathrm{abs}}_{\mathrm{m}}$ (at 1.425 μm) of each atmospheric layer with a constant. The viewing direction is nadir ($\theta = 0°$) and the solar zenith angle, θ_0, is 30°, 45°, or 60°. Angle $\phi - \phi_0$ is 0°. As can be seen, increasing $\sum b^{\mathrm{m}}_{\mathrm{abs}}$ decreases F for all vertical aerosol profiles and angles θ_0, as expected. Adding a haze slightly increases F, because more light is scattered back. At these long wavelengths, there is little gaseous scattering above the cloud and haze, hence the cloud top altitude has virtually no effect on F at small $\sum b^{\mathrm{m}}_{\mathrm{abs}}$. However, in the presence of absorption, the higher the cloud top, the higher F at a given $\sum b^{\mathrm{m}}_{\mathrm{abs}}$, as more light is scattered. With a smaller cloud scale height H, the cloud particle number density increases per unit volume where the scattering takes place (cf. Fig. 4.14) which increases the scattering by clouds, and thus F. And, with increasing θ_0, F decreases at a given $\sum b^{\mathrm{m}}_{\mathrm{abs}}$ as the incident flux per unit area at the top of the atmosphere decreases, and as the path-length through the atmosphere increases. In addition, the flux of light that is singly scattered by the cloud particles decreases with increasing θ_0 (see Fig. 4.3).

For P, the results are less straightforward: an increase in $\sum b^{\mathrm{m}}_{\mathrm{abs}}$ can increase or decrease P. The continuum P depends strongly on the single scattering P (cf. Fig. 4.3). This explains the (small) difference (~ 1%) in the continuum P in the top row of Fig. 4.4, where the haze optical thickness is varied, and it explains the lack of a difference in the continuum P when only the cloud top altitude is varied. With increasing $\sum b^{\mathrm{m}}_{\mathrm{abs}}$, multiple scattering decreases and the altitude where P of the reflected light is determined, increases. This means that P is thus increasingly determined by the single scattering properties of the particles at increasing altitudes. At large values of $\sum b^{\mathrm{m}}_{\mathrm{abs}}$, the single scattering by the haze particles and eventually the gas molecules dominates. Increasing scale height H (third row) influences P as it increases the number of cloud and haze particles in the higher atmospheric layers. Increasing θ_0 (bottom row), decreases the single scattering angle and thus changes P of the singly scattered light (cf. Fig. 4.3) that is apparent at large values of $\sum b^{\mathrm{m}}_{\mathrm{abs}}$.

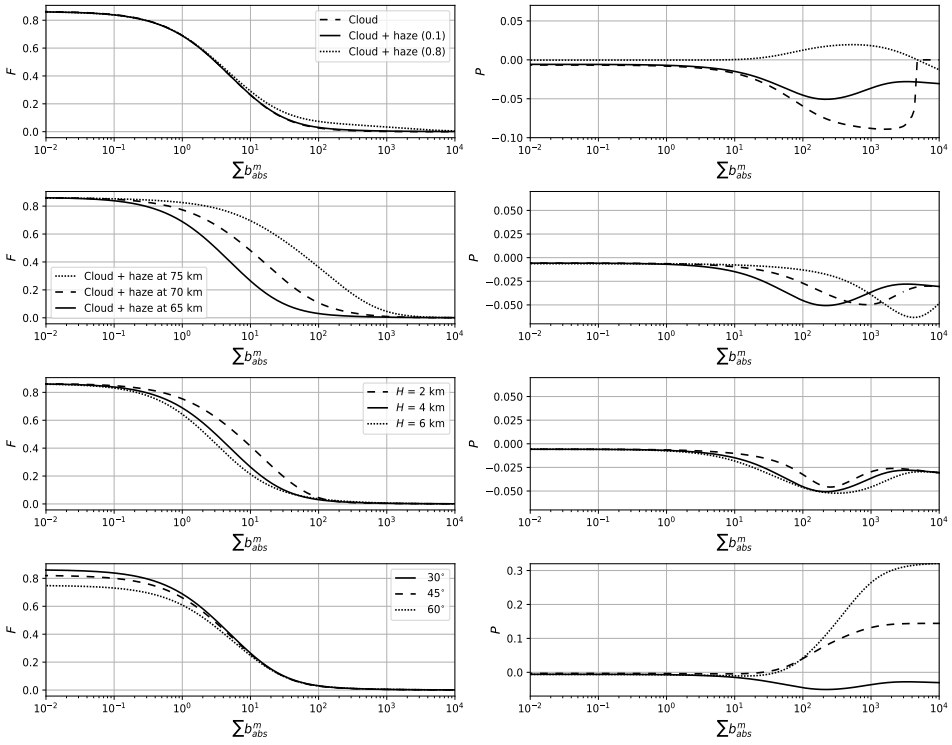

Figure 4.4: Reflected flux F (left) and degree of polarization P (right) as functions of $\sum b^{\mathrm{m}}_{\mathrm{abs}}$. The viewing direction is nadir ($\theta = 0°$). Unless specified otherwise, the parameter settings are as follows (the solid lines are all for these settings): The solar zenith angle, θ_0, is 30°. The cloud optical thickness, b^{a}, is 30, the cloud top, z_{top}, at 65 km, and the scale height, H, is 4 km. The haze optical thickness is 0.1, the haze top altitude is always 2 km above the cloud top altitude. Top row: The haze optical thickness is 0.0 (dashed lines), 0.1 (solid lines), or 0.8 (dotted lines). Second row: The cloud top is 65 km (solid lines), 70 km (dashed lines), or 75 km (dotted lines). Third row: The cloud scale height, H, is 2 km (dashed lines), 4 km (solid lines), or 6 km (dotted lines). Bottom row: The solar zenith angle, θ_0, is 30° (solid lines), 45° (dashed lines), or 60° (dotted lines).

4.3.2. F AND P AS FUNCTIONS OF THE WAVELENGTH

Figure 4.5 shows computed high-spectral resolution spectra of F and P for a model atmosphere with a cloud and a haze, with optical thicknesses of 30 and 0.1, respectively. The cloud and haze scale heights are both 4 km, and the cloud top altitude is 65 km. The viewing direction is nadir and θ_0 is 30°. The numerous fine lines following the CO_2 absorption lines can clearly be seen in F. As expected from the previous section, the spectral behaviour of P is more complex, with P varying rapidly and frequently changing sign, and thus direction, across individual absorption lines. The simulations show that high-spectral resolution P measurements contain information on the aerosol characteristics, depending on the absorption line strength. As mentioned earlier, fine lines have been previously observed on Venus with a very high resolution Fourier spectropolarimetry instrument (Forbes and Fymat, 1974) , albeit as a function of angular fluxes.

Figure 4.6 shows what an instrument with a coarser spectral resolution would mea-

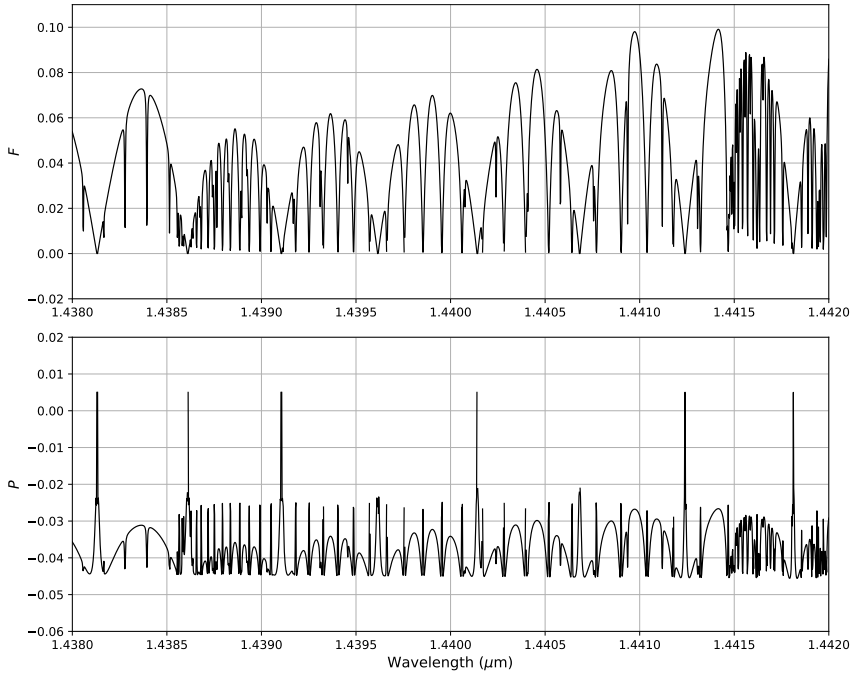

Figure 4.5: High–spectral resolution F and P around 1.44 μm of light reflected by an atmosphere with a cloud and haze, with the cloud top at 65 km, H= 4 km, $\theta = 0°$ and $\theta_0 = 30°$, b. The optical thicknesses of the cloud and the haze are 30 and 0.1, respectively.

sure, assuming a box-shaped, 1 nm wide instrument spectral response function. These computations have been performed using the ck-method as described in 4.6 and for the same atmosphere models and geometries as in Fig. 4.4. As in that figure, F is very insensitive to the haze optical thickness (top row): only in the deepest part of the absorption band, an optically thicker haze leads to a slightly higher F. The corresponding P curves do differ from each other, because of the different single scattering polarization of the cloud and the haze particles, similarly to the curves in Fig. 4.4. Increasing the cloud top altitude (second row) increases F inside the band as less CO_2 is located above the cloud, and decreases $|P|$ as also seen in Fig. 4.4. Note that the 1 nm spectral resolution washes out the behaviour of P as seen at the largest values of $\sum b_{\text{abs}}^{\text{m}}$ in Figs. 4.4 and 4.5. Increasing θ_0 (third row) increases F except in the deepest part of the absorption band. It increases $|P|$ in the deepest part and changes the polarization direction from negative (parallel to the reference plane) to positive (perpendicular to the plane). This is due to the corresponding decrease of the single scattering angle and single scattering P (Fig. 4.3). The influence of scale height H (fourth row) is similar to that of F and P shown in Fig. 4.4.

Figure 4.7 is similar to Fig. 4.6, except with curves for instrumental response functions corresponding to a box-shaped 5 nm response and SPICAV-IR's response function respectively. As expected, increasing the response function width decreases the strength

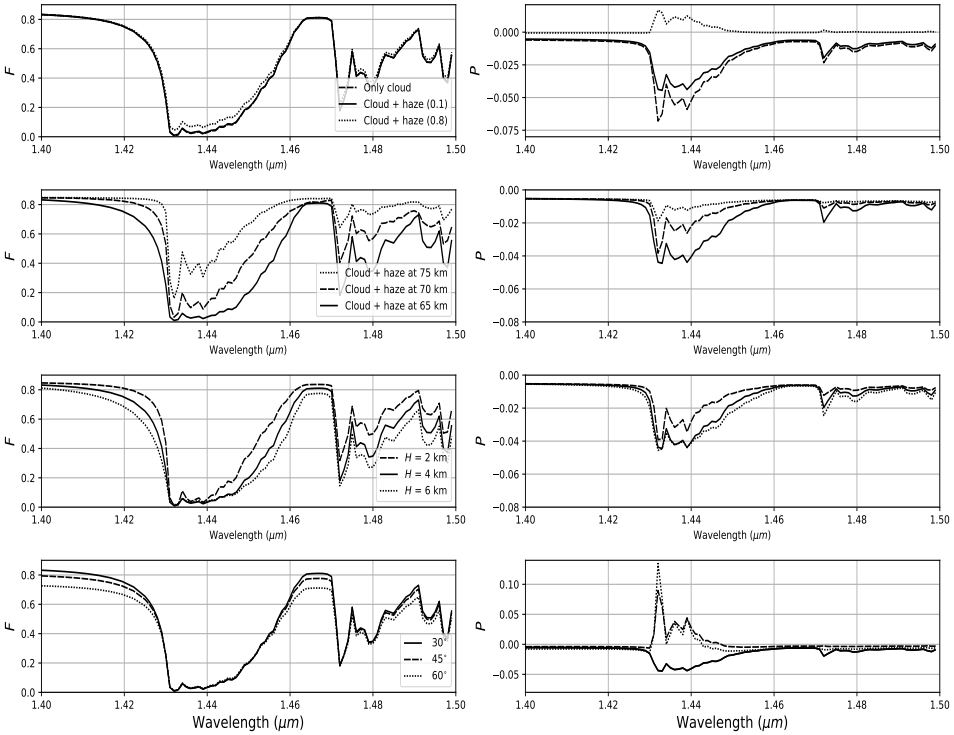

Figure 4.6: Reflected flux F (left) and P (right) as functions of λ for the same model atmospheres, and θ_0 and θ as in Fig. 4.4, except using a 1 nm wide, box-shaped spectral response function.

of the absorption band features both in F and in P. As described in Korablev et al. (2012), SPICAV-IR's response function is asymmetric around the central wavelength under consideration resulting in an added complexity in the nature of the resulting F and P.

4.3.3. AN AEROSOL SENSITIVITY ANALYSIS

We have performed a sensitivity study with different aerosol parameters to identify what could be retrieved from measurements. Following Boesche et al. (2009), we define the changes in the flux as $\Delta F = F_b/F_c$, with F_b the flux inside the bands, and F_c the flux in the continuum. We define the changes in the polarization as $\Delta P = P_b$ - P_c, with P_b, P in the band, and P_c, P in the continuum. For the continuum, we choose 1.40 μm, and for the band, we choose a strong absorption region, at 1.44 μm, and a weaker one, at 1.48 μm.

Figure 4.8 shows ΔF and ΔP computed with a 1 nm wide spectral response function for $\theta_0 = 30°$ and 60°, respectively. In the top row, the haze optical thickness b_{haze} increases from 0 to 1. In general, ΔF increases with b_{haze}, but more so when there is increased absorption (at 1.44 μm), although the band itself is much deeper, and when θ_0 is larger. This is due to increased scattering by the haze particles. This increase in scat-

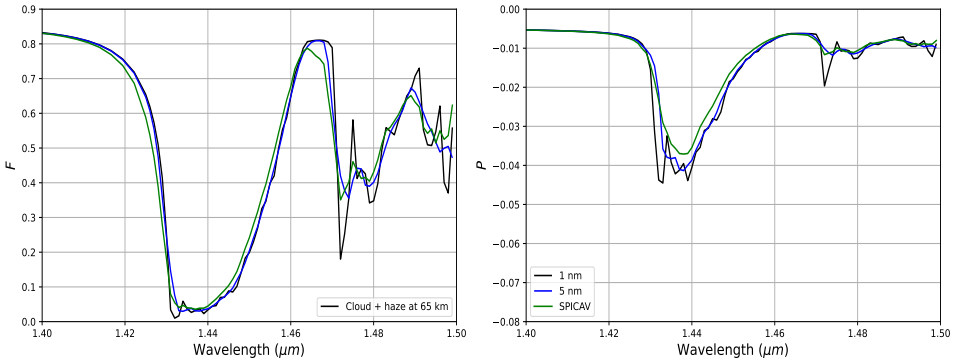

Figure 4.7: Similar to Fig. 4.6, except only for the standard model atmosphere (b_{cloud} = 30, b_{haze} = 0.1, H= 4 km), with box-shaped instrument response functions with the following widths: 1 nm (black), 5 nm (blue) and SPICAV-IR IRF (green).

tering is also noticeable in ΔP: in the deepest band, ΔP increases more with b_{haze} than in the weaker band. The difference in single scattering P of the haze particles (Fig. 4.3) causes the difference in ΔP with the different values of θ_0. ΔP at 60° reaches an asymptote for b_{haze} greater than 0.4, but for 30° there is no such asymptote which can be explained by the combination of the decreasing band depth with increased cloud top altitude and specific single scattering properties of the cloud particles at 60° as compared to 30°.

In the second row, the cloud top altitude increases from 60 to 76 km. Here, ΔF increases with cloud top altitude in both bands, but strongest in the weaker band, because there, lower altitudes are probed. This band would thus be a good choice for cloud top altitude retrievals in F. In the strong band and for larger θ_0, P could also be used to retrieve cloud top altitudes, as ΔP depends strongly on these altitudes. The large change in P at θ_0 = 60° is primarily due to scattering by haze, having a higher positive polarization at this angle as compared to that at θ_0 = 30°, and gas above the clouds, which decreases as the amount of gas above the clouds with increasing cloud top altitude decreases. In the bottom row, the cloud scale height H increases from 2 to 6 km. In the weak absorption band (1.48 μm), ΔF varies the most with H as that is where the contribution of total flux due to haze is higher. In the strong absorption band, F is less sensitive to cloud properties. Furthermore, ΔF in the strongest band and ΔP in both bands do not change significantly with H.

Figure 4.9 shows the influence of the instrument response width on ΔF and ΔP, for widths of 5 nm and SPICAV instrument response alongwith the box shaped function of width 1 nm as comparison. The widths do not change the change of ΔF with b_{haze}, cloud top altitude, or H, except that the absolute values are different, because a wider response function decreases the measured depths of the deep and the weaker absorption band. For ΔP, increasing the width decreases the sensitivity for b_{haze}, the cloud top altitude, and H. Indeed, increasing the width decreases ΔP such that the bands will be indistinguishable from the continuum. Clearly, a narrow response function is preferred if one

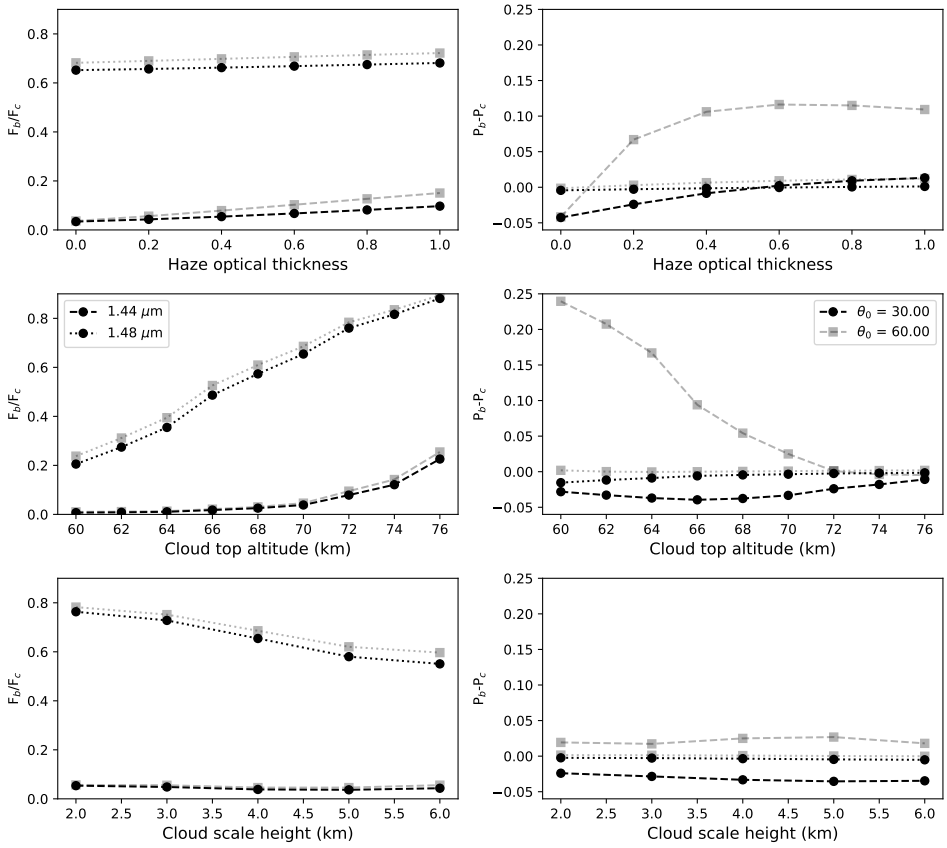

Figure 4.8: The absorption band depth in flux, $\Delta F = F_b/F_c$, (left column) and in degree of polarization, $\Delta P = P_b - P_c$, (right column) as functions of the haze optical thickness b_{haze} (top row), the cloud top altitude (middle row), and the cloud scale height H (bottom row). The instrument response function was assumed to be box-shaped, with a width of 1 nm. The solar zenith angle θ_0 ('SZA' in the legend) is 30° (black lines) or 60° (gray lines). The viewing angle θ is 0°. The continuum wavelength is 1.40 μm, and results are shown for a wavelength in a strong absorption band, 1.44 μm (dashed lines), and a weak absorption band, 1.48 μm (dotted lines). Except in the top row, b_{haze} is 0.1. Except in the middle row, the cloud top altitude is 70 km. Except in the bottom row, scale height H is 4 km.

aims to use polarimetry across absorption bands to derive aerosol properties. The differences in the sensitivity due to varying absorption at different wavelengths can also add to the information regarding the atmospheric constituents and thus enable better characterization of aerosols.

4.4. ANALYSIS OF SPICAV-IR POLARIZATION MEASUREMENTS

Figure 4.10 shows P as derived from the SPICAV-IR measurements, and the uncertainty on the data, along orbit 1478 (see Fig. 4.1), which covers latitudes between +15° and +72°. We have performed a comparison between this P and results from model compu-

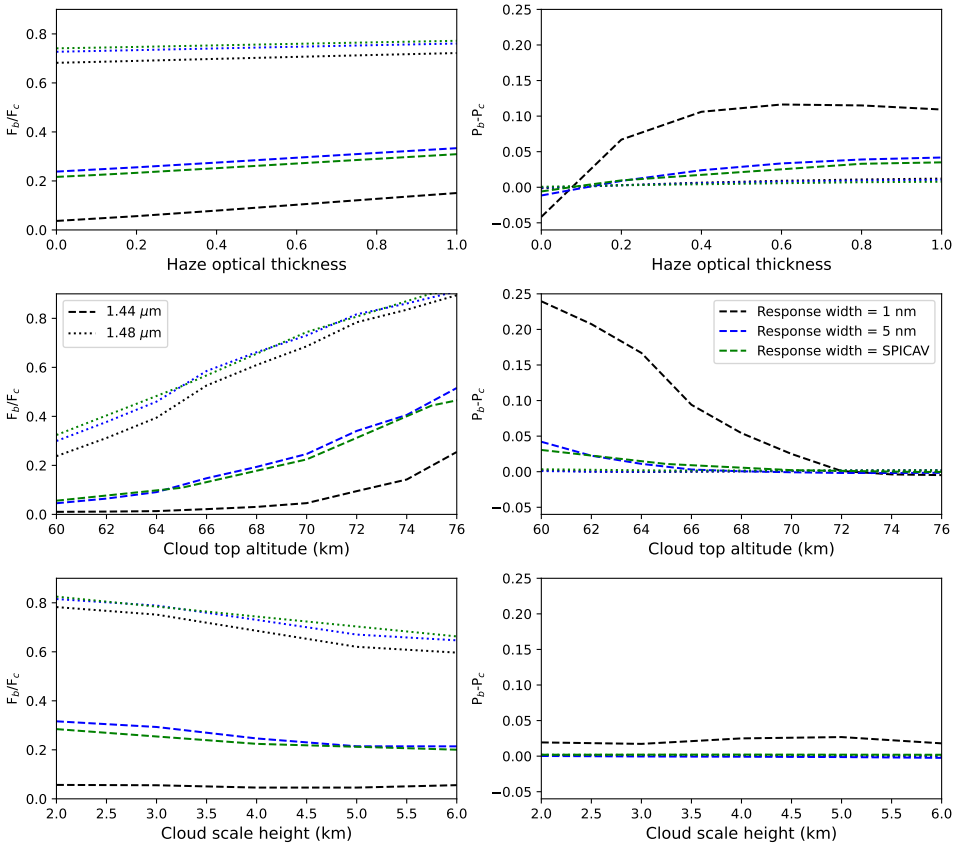

Figure 4.9: Similar to Fig. 4.8, except only for $\theta_0 = 60°$ and with curves for instrument response widths of 5 nm (blue) and SPICAV instrument response function added (green).

tations for three cloud top altitudes, with b_{haze} ranging from 0.0 (no haze) to 0.8. The SPICAV-IR response function as described by Korablev et al. (2012), is taken into account in our computations, although the response during the measurements in orbit might have been different (Fedorova et al., 2016). We use a continuum wavelength, i.e. 1.40 μm, and a wavelength in the strong absorption band, i.e. 1.44 μm. Note the different vertical scale for the 1.40 μm and the 1.44 μm plots. Along orbit 1478, θ_0 ranges from 20° to 75°, the relative azimuth angle $\phi - \phi_0$ varies between 4° and 7° and the viewing angle between 7° and 11°. For every data point, we use the appropriate θ_0, θ, and $\phi - \phi_0$.

The top row of Fig. 4.10 pertains to 1.40 μm. At this continuum wavelength, the model P-curves show no dependence on the cloud top altitude, as expected from Fig. 4.9). At small values of θ_0 ($< 50°$), small values of b_{haze} fit the data better than large values. At large values of θ_0 ($> 60°$), which correspond to high latitudes, values of b_{haze} between 0.1 and 0.4 appear to fit the data best. This latitude-dependence agrees with what is expected on Venus, i.e. a haze optical thickness that increases towards the poles (Knol-

lenberg and Hunten, 1980).

In the strong absorption band, at 1.44 μm, P does show sensitivity to the cloud top altitude, in addition to sensitivity to b_{haze}. At low latitudes, the model curves for a cloud top altitude of 70 km agree best with the data. Like at the continuum wavelength, the comparison in the band indicates that at high latitudes, models with a relatively large b_{haze} (> 0.2) fit better if the cloud top is at 70 km. At high latitudes, the best fit b_{haze} depends on the cloud top altitude: a higher cloud requires a smaller b_{haze}. According to Knollenberg and Hunten (1980), the cloud top altitudes decreases from ~ 75 km close to the equator to ~ 65 km close to the poles while the haze optical thickness increases. With a cloud top at 65 km, our model computations in the absorption band suggest that b_{haze} should be between 0.1 and 0.2 at high latitudes. In the bottom row of Fig. 4.10, we show $\Delta P = P_{\text{b}} - P_{\text{c}}$ (thus P at 1.44 μm minus P at 1.40 μm) with model curves. The fit of ΔP agrees with the findings at 1.44 μm. Being able to use ΔP instead of the absolute values of P eliminates the need for absolute polarisation calibration of an instrument, as only the difference in polarisation is relevant.

We performed a simple b_{haze} retrieval using the ΔP data from four orbits spanning latitudes -60° to +60°, as shown in Fig. 4.1, assuming cloud top altitudes as derived from flux data by Fedorova et al. (2016), and a cloud scale height H of 4 km (Ignatiev et al., 2009). The fitting of b_{haze} was done with a least square error minimization routine LMFIT as described in Newville et al. (2016). The best fitting b_{haze} profiles were obtained for each orbit between wavelength range of 1.4 to 1.5 μm and a unique observation geometry of SPICAV-IR. Figure 4.11 shows the derived b_{haze} averaged over the four orbits which has been binned with respect to latitude (20 bins) and the error bars show the standard deviation of the distribution around each latitude bin. Although the retrieved b_{haze} profile has a large uncertainty that can be primarily attributed to the low signal-to-noise ratio within the absorption band, the averaged trend clearly shows that b_{haze} increases towards the poles which is what is to be expected from previous studies (Kawabata et al., 1980; Knollenberg and Hunten, 1980; Braak et al., 2002). Our retrieval reaches a maximum b_{haze} of ≈0.6 near -60° and +60°.

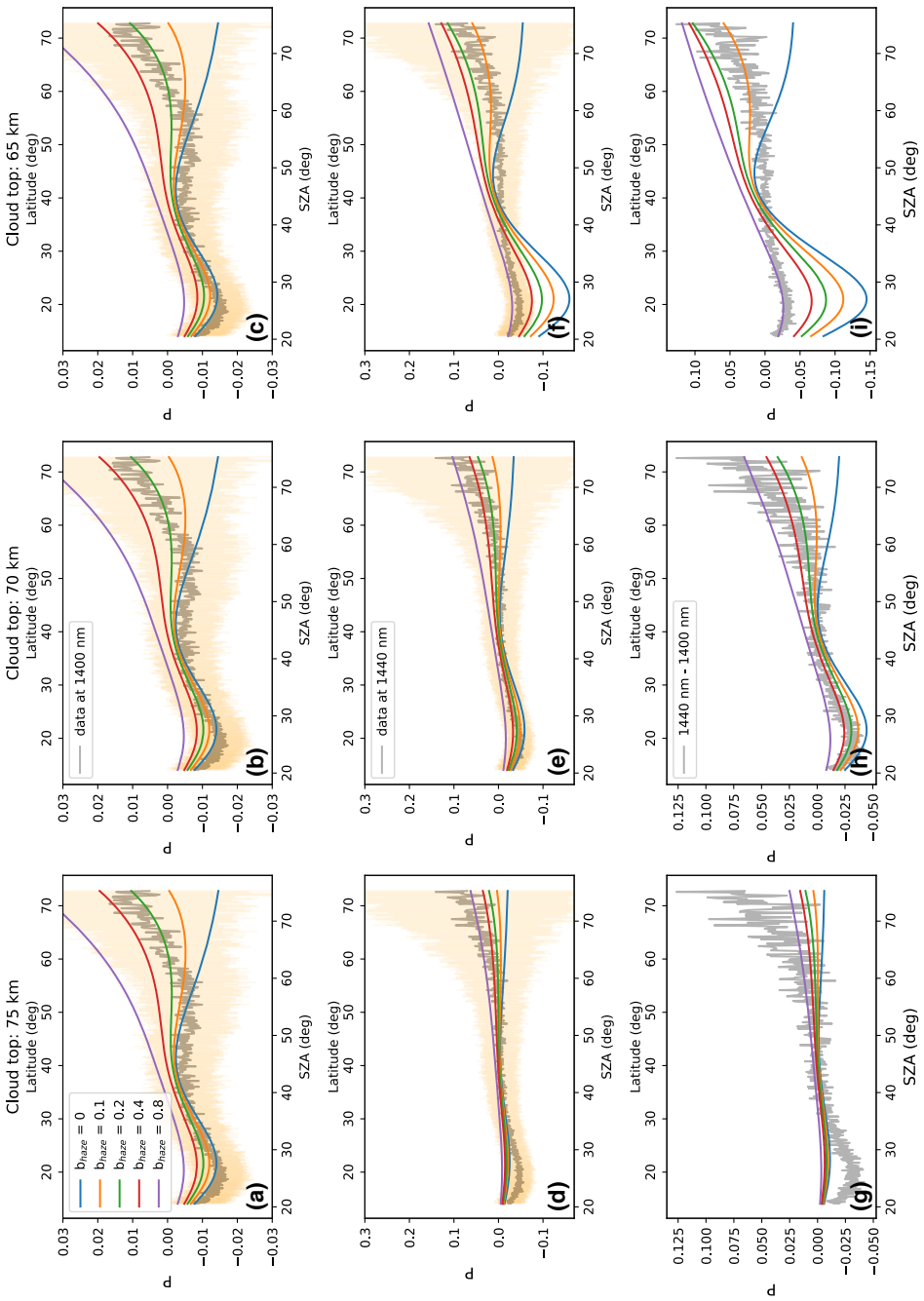

Figure 4.10: The degree of polarisation P derived from SPICAV-IR data along orbit 1478 (cf. Fig. 4.1) in the continuum at 1.40 μm (top row), and in the strong absorption band at 1.44 μm (middle row). The bottom row shows the absolute difference between P in the middle and in the top row. The shaded area in the top and middle rows is the standard deviation of the error in the data. The lines are model results for cloud top altitudes of 75 km (first column), 70 km (middle column), and 65 km (right column). The cloud scale height is 4 km. For b_{haze}, we have used: 0.0 (blue), 0.1 (orange), 0.2 (green), 0.4 (red), and 0.8 (purple).

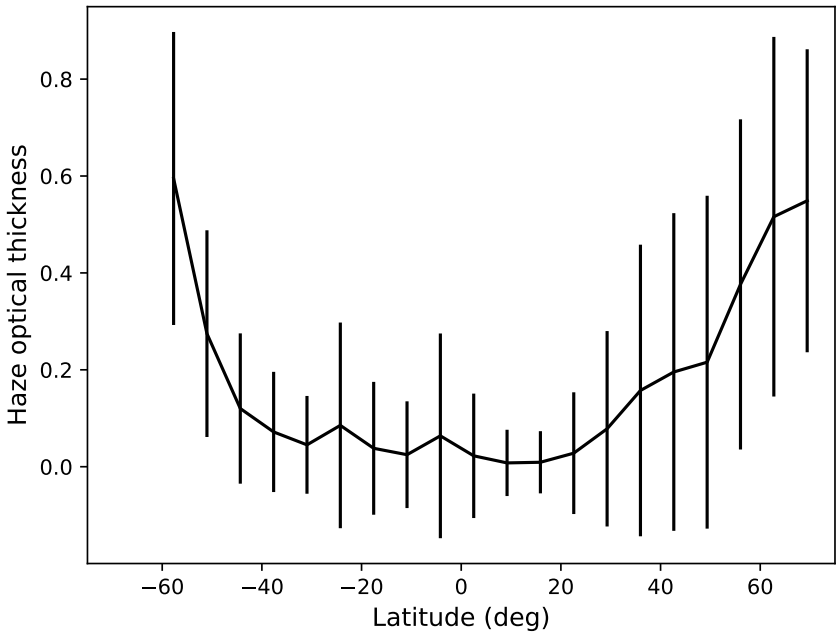

Figure 4.11: The haze optical thickness b_{haze} as a function of latitude derived from fitting model computations to SPICAV-IR data along 4 orbits (see Fig. 4.1). The error bars show the standard deviation of the retrieved values.

4.5. DISCUSSION AND CONCLUSIONS

We have presented a way of systematically understanding the behaviour of flux F and degree of (linear) polarization P of light reflected locally by the atmosphere of Venus by first performing an analysis with increasing total atmospheric absorption optical thickness ($\sum b_{\text{abs}}^{\text{m}}$) and then simulating the signal across the wavelength range between 1.4 - 1.5 μm which contains a strong CO_2 absorption band.

We carried out an error analysis taking into account various realistic aerosol parameters, to understand if ck-method can be used for modelling the F and P. The large errors in P (~3.5%) close to $\theta_0 = 60°$ at strong absorption makes ck-method unsuitable for modelling the signals for a well calibrated polarimetric instrument as this is at the order of the change in signal one would expect due to a variation in aerosol parameters as demonstrated in our sensitivity analysis.

Our sensitivity analysis with a 1 nm box instrument response indicates that changes in cloud tops results in detectable changes in both F_b/F_c and P_b-P_c in the absorption bands. Change in haze optical thickness results in significant change in P_b-P_c while not significant enough change in F_b/F_c. Retrieving cloud scale height using either F or P will be challenging by making observations at the three wavelengths we chose in this study as there is no significant change with cloud scale height variation. Although having observations at more wavelengths around the wavelength region considered in this study might make it possible to retrieve cloud scale height as our forward models show significant change in the shape of the band due to a change in cloud scale height.

The spectral resolution of measurements of P across a gaseous absorption band strongly determines the band strength and information content: the higher the resolution, the stronger the features and the more information. Measurements in F appear to be more robust to change in instrument response. Thus a narrow spectral instrument response would be a better option to reap the benefit of both. Our model simulations show satisfactory agreement with P derived using the orthogonally polarized SPICAV-IR flux data. We find that the increase in $|P|$ (as observed in the data in Fig. 4.1) is to be expected inside the absorption bands and its sign depends on the aerosol present in the atmosphere and the observation geometry. The increase in $|P|$ is primarily due to increased single scattering by the aerosol particles which contribute the most to the scattered signal. Close to the Venus equator, scattering by cloud particles dominate as the haze optical thickness is small. That is the reason for negative P in SPICAV-IR data (cf. Fig. 4.1) at equatorial and mid-latitude regions. The scattering is dominated by sub-micron haze particles that have a strong positive P closer to the poles.

We presented a qualitative analysis and derived haze optical thickness b_{haze} as a function of latitude using a select few orbits of SPICAV-IR data. With an assumed cloud top and scale height we find that b_{haze} increases towards the planets poles which is in good agreement with previous measurements. This is despite the uncertainty associated with the response of the instrument as a function of wavelength. Our intention here was to show that the P data derived from the absorption band contains valuable information regarding the cloud and haze properties. An elaborate retrieval is out of the scope of this theoretical modelling paper but more information could be used (for example the whole of absorption band wavelength range between 1.4 - 1.5 μm) to possibly derive more accurate information regarding the haze and/or determine other aerosol properties such

as cloud top and cloud scale height. In future we intend to better quantify the errors associated with the SPICAV-IR instrument response and hope to be able to derive cloud top and/or haze optical thickness for a larger dataset using P.

In this paper, we have conclusively shown that the P signal contained within the absorption band data of SPICAV-IR instrument contains valuable information regarding the cloud and haze particles of Venus by as a first attempt, deriving the haze optical thickness above the cloud deck which was previously ignored while fitting total flux data. Our forward models with theoretical instrument response functions suggests that an instrument measuring degree of polarization with a well calibrated and narrow instrument response width should be able to measure not only changes due to haze optical thickness, but also changes due to cloud top and cloud scale heights which would help in adding valuable information about the dynamic spatial and temporal variation of clouds and hazes on Venus.

4.6. APPENDIX: CORRELATED-k METHOD

In this paper, we use the correlated k-distribution method (ck-method), for the computations of reflected sunlight across CO_2 absorption bands (Lacis and Oinas, 1991; Fu and Liou, 1992; Stam et al., 2000). In this method, the highly wavelength dependent absorption cross-sections (σ_{abs}) across a given spectral interval (see Fig. 4.12 top) are rearranged based on their strength, resulting in a relatively smooth function (see Fig. 4.12 bottom) that describes the same variation in absorption cross-sections as the original absorption cross-section spectrum, that can be represented with far less radiative transfer computations than the original spectrum. Because the spectral information about the absorption cross-sections is lost in this process, the ck-method assumes that these cross-sections are correlated in wavelength space, which is not necessarily the case due to the dependence of absorption cross-section on the ambient pressure and temperature (see Fig. 4.12). We have analyzed the errors in our computed flux and polarization for Venus due to using the ck-method by comparing them with flux and polarization computed using line-by-line (lbl-method) computations, following the analysis by Stam et al. (2000) for sunlight reflected by Earth.

For the comparison of lbl-method results with ck-method results, we use a spectral resolution of 1 nm and a box-shaped response function. We thus convolve the computed high-spectral resolution line-by-line total and polarized fluxes with the response function, and apply the ck-method to the same, 1 nm wide spectral bins, using Gauss-Legendre integration for each bin, with 20 Gaussian abscissae. The errors also depend on the number of Gaussian abscissae. We found that there was not a significant improvement with an increase in abscissae for the model cases discussed here. Fig. 4.13 shows examples of computed total flux F and degree of polarization P for the whole range of wavelength from 1.4 μm to 1.5 μm.

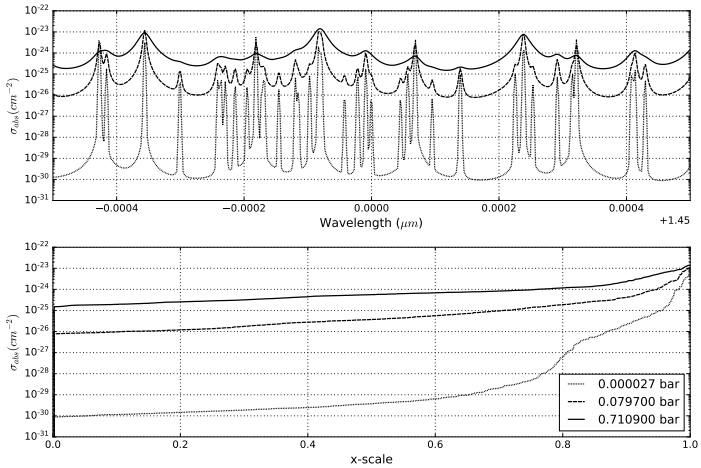

Figure 4.12: Top: CO_2 absorption cross-sections at three pressure levels as functions of the wavelength. Bottom: the corresponding sorted cross-sections on a cumulative distribution scale.

4.7. APPENDIX: AEROSOL VERTICAL DISTRIBUTION FORMULATION

Here, we outline our computation method of the number densities of aerosol (cloud or haze) particles in the atmospheric layers. Figure 4.14 shows an example of an aerosol vertical distribution with both a cloud and a haze. In the bottom part of the cloud, starting at altitude z_{bot}, the particle number density is constant. Above altitude z_{cut}, it decreases exponentially with scale height H, until 76 km, above which, there are no cloud particles. The altitude of the cloud top, z_{top}, is defined as the altitude where the cloud optical thickness equals 1 measured from the top of the atmosphere (see below). The particle number density of the haze is chosen to decrease exponentially from the bottom upwards.

The aerosol number density, N^a, in a given atmospheric layer, is equal to $k_{\text{ext}}/\sigma_{\text{ext}}$, where k_{ext} is the (wavelength dependent) extinction coefficient in the layer, and σ_{ext} the (wavelength dependent) extinction cross-section of the aerosol. According to Fedorova et al. (2016), $k_{\text{ext}} = 2$ km^{-1} in the bottom part of the clouds and across the wavelength region between 1.4 and 1.5 μm. For a log-normal size distribution for the spherical cloud particles, with $r_g = 1.05$ μm and $\sigma = 1.21$ and a refractive index of 1.400, we then find $\sigma_{\text{ext}} = 18.889 \cdot 10^{-8}$ cm^2, and $N^a = N_0 = 108$ cm^{-3} in the bottom part of the clouds, thus between z_{bot} and z_{cut}.

Above altitude z_{cut}, the particle number density in layer i, with altitude z_i in the middle of the layer, is then given by

$$N_i^a = N_0 \exp^{-\frac{z_i - z_{\text{cut}}}{H}}, \tag{4.10}$$

with H the scale height (e.g. in km), the value of which we choose ourselves, based on the literature. We also choose the cloud top altitude, z_{top}, based on the literature. In order to

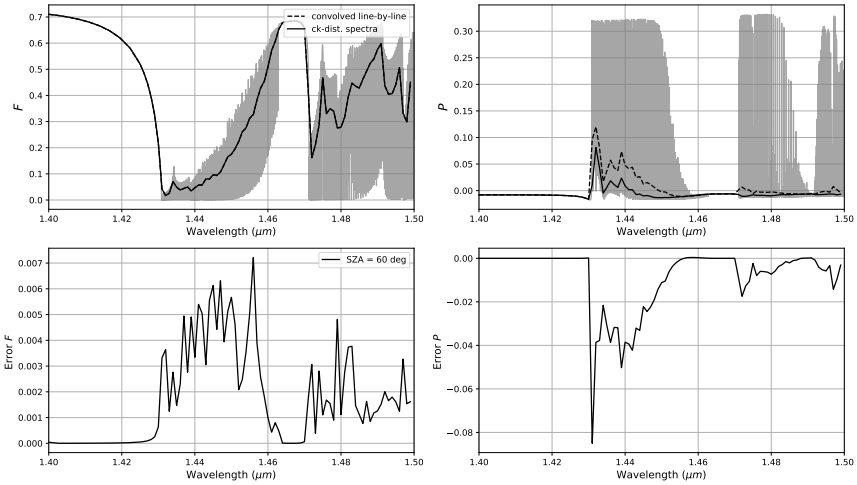

Figure 4.13: The flux F and degree of polarization P as computed using the line-by-line method, before and after convolution with the instrument response function, and the ck-method (top row). For these computations, $\theta_0 = 60°$ and $\theta = 0°$. Errors due to using the ck-method (bottom row) for $\theta = 0°$ and θ_0=60°. The atmosphere has cloud top at 65 km, cloud scale height of 2 km and haze with optical thickness 0.1.

determine N^a in a layer, we have to determine z_{cut}, for which we can use the following equation:

$$\int_{z_{\text{top}}}^{\infty} \sigma_0 N_0 \exp(-\frac{z - z_{\text{cut}}}{H})\, dz = 1, \tag{4.11}$$

with '1' the cloud optical thickness. From this equation, it follows that

$$z_{\text{cut}} = z_{\text{top}} - H \ln(\sigma_0 N_0 H) \tag{4.12}$$

In the equation above, we implicitly assume that z_{top} falls above z_{cut}. Whether this assumption holds, depends on H. For our cases, it holds for H between 2 and 6 km. The bottom altitude of the cloud, z_{bot}, is determined from the total optical thickness of the cloud, which we take as 30. In our case, $z_{\text{bot}} = 47$ km.

The haze layer (see Fig. 4.14) is located above the cloud layer and extends up to 96 km. The haze particle number density is computed using Eq. 4.10, assuming a log-normal size distribution with $\sigma_0 = 0.161 \cdot 10^{-8}$ cm^2 (this is assumed to be wavelength independent). For a given value of H, N_0 is chosen such that the total haze optical thickness equals 0.1.

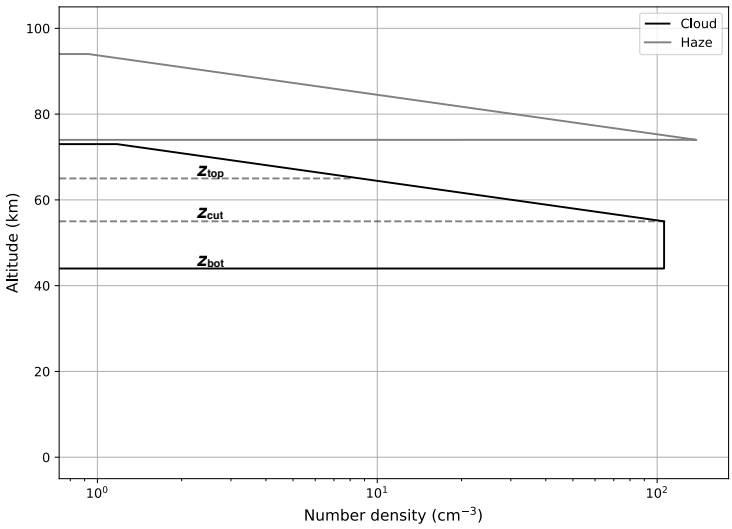

Figure 4.14: A sample vertical distribution of cloud and haze particles expressed in their number density N^a (cm^{-3}). Both the cloud and the haze have a scale height H of 4 km. The optical thicknesses of the cloud and the haze are 30 and 0.1, respectively. The various altitudes z_{top}, z_{cut}, and z_{bot} are explained in the text.

5

From exo-Earths to exo-Venuses: Flux and Polarization Signatures of Reflected Light

Gourav Mahapatra, Fouad Abiad, Loic Rossi, Daphne M. Stam

Terrestrial-type exoplanets in or near stellar habitable zones appear to be ubiquitous. It is, however, unknown which of these planets have temperate, Earth-like climates or e.g. extreme, Venus-like climates.Technical tools to distinguish different types of terrestrial-type planets are crucial for determining whether a planet could be habitable or incompatible with life as we know it. We investigate the potential of spectropolarimetry for distinguishing exo-Earths from exo-Venuses. We present numerically computed fluxes and degrees of linear polarization of starlight that is reflected by exoplanets with atmospheres in evolutionary states ranging from similar to the current Earth to similar to the current Venus, with cloud compositions ranging from pure water to 75% sulfuric acid solution, for wavelengths between 0.3 and 2.5 μm. We also present flux and polarization signals of such planets in stable but spatially unresolved orbits around the star Alpha Centauri A. The degree of polarization of the reflected starlight shows larger variations with the planetary phase angle and wavelength than the total flux. Across the visible, the largest degree of polarization is reached for an Earth-like atmosphere with water clouds, due to

Parts of this chapter have been published in the journal of Astronomy & Astrophysics **(A&A 671, A165 (2023))**, Mahapatra et al. (2023).

Rayleigh scattering above the clouds and the rainbow feature at phase angles near 40°. At near-infrared wavelengths, the planet with a Venus-like CO_2 atmosphere and thin water clouds shows the most prominent polarization features due to Rayleigh-like scattering by the small cloud droplets. A planet in a stable orbit around Alpha Centauri A would leave temporal variations on the order of 10^{-13} W/m^3 in the total reflected flux and 10^{-11} in the total degree of polarization as the planet orbits the star and assuming a spatially unresolved star-planet system. Star-planet contrasts are in the order of 10^{-10} and vary proportionally with planetary flux. Current polarimeters appear to be incapable to distinguish between the possible evolutionary phases of spatially unresolved terrestrial exo-planets, as a sensitivity close to 10^{-10} would be required to discern the planetary signal given the background of unpolarized starlight. A telescope/instrument capable of achieving planet-star contrasts lower than 10^{-9} should be able to observe the large variation of the planets resolved degree of polarization as a function of its phase angle and thus be able to discern an exo-Earth from an exo-Venus based on their clouds unique polarization signatures.

5.1. INTRODUCTION

Despite having similar sizes, being formed around the same time and from similar materials, it is clear that the Earth and Venus have evolved into dramatically different worlds. While it is generally acknowledged that Venus once had much larger amounts of water than today, it is still debated whether Venus was once more Earth-like with oceans of water before the runaway-greenhouse-effect took off (Donahue et al., 1982), or whether the atmospheric water vapour never actually condensed on the surface (Turbet et al., 2021). Bullock and Grinspoon (2001) conducted a detailed study of the possible evolution of Venus' climate over long time periods starting with a water vapour enriched atmosphere. Terrestrial-type exoplanets are also expected to harbour a wide variety of atmospheric compositions with maybe only a few planets hospitable to life as we know it. Various climate models suggest that the likelihood of a planetary atmosphere exhibiting a Venus-like runaway-greenhouse-effect is higher than that of an atmosphere in an Earth-like, N_2-dominated state (Lincowski et al., 2018, and references therein). A study by Kane et al. (2020) even shows that Jupiter's migration might have stimulated the runaway-greenhouse-effect on Venus, suggesting that there could be more Venus-analogs than Earth-analogs in planetary systems with Jupiter-like planets.

As planned powerful telescopes and dedicated, sensitive detection techniques will allow us to characterize smaller exoplanets in the near-future, it will become possible to probe terrestrial-type planets in and near the habitable zones of solar-type stars and to find out whether they resemble Earth or Venus, or something else all together. The high-altitude cloud deck on an exo-Venus would make it difficult to use a technique like transit spectroscopy for the characterization of the planet as the clouds themselves would block the transmission of the starlight and apart from a spectral dependence of the cloud optical thickness which could leave a wavelength dependent transmission through the cloud tops, the microphysical properties of the cloud particles, such as their composition, shape and size distribution would remain a mystery. Also, the clouds would inhibit measuring trace gas column densities as they would block the planet's lower atmosphere and only allow transit spectroscopy of the highest regions of the atmosphere (see, e.g. Lustig-Yaeger et al., 2019a, and references therein). Indeed, a Venus-like ubiquitous cloud deck could possibly be mistaken for the planet's surface, as one would only measure the transmittance through the gaseous atmosphere above the clouds, possibly inferring the atmosphere to be thin and eroding (Lustig-Yaeger et al., 2019b).

Jordan et al. (2021) modelled the photochemistry of some of the primary sulphuric chemical species that should be responsible for the formation and sustenance of Venus' sulfuric acid solution clouds, such as SO_2, OCS and H_2S, and found that the abundances of such species above the cloud deck would depend heavily on the effective temperature and distance to the parent star, with their abundances decreasing with increasing temperature and being depleted, as we see on Venus, in the presence of a star like the Sun. Thus it would be challenging to rule out the possibility of an exoplanet being a Venus analog solely on the basis of the detection of such chemical species in transmission spectra (Jordan et al., 2021). Indeed, the full characterization of rocky exoplanets and their classification appears to require the direct imaging of starlight that is reflected by such planets and/or the thermal radiation that is emitted by them. While telescopes able to perform such measurements are not yet available, plans are underway for their

development and deployment (Keller et al., 2010; Team et al., 2019).

While most of telescopes and instruments are designed for only measuring total fluxes of exoplanets, including (spectro)polarimetry is also being considered. The main reason to include (spectro)polarimetry (see e.g. Rossi et al., 2021, and references therein) is that it increases the contrast between star and planet, as the stellar flux will be mostly unpolarized when integrated over the disk (Kemp et al., 1987), while the flux of the reflected starlight will usually be (linearly) polarized. And in addition, (spectro)polarimetry can be used for the characterization of planetary atmospheres and surfaces. As a classic example of the latter, Hansen and Hovenier (1974) used Earth-based measurements of the disk-integrated degree of polarization of sunlight that was reflected by Venus in three spectral bands and across a broad phase angle range, to deduce that the particles forming Venus' main cloud deck consist of 75% sulfuric acid solution, that the effective radius of their size distribution is 1.05 μm, and that the effective width of the distribution is 0.07. They also derived the cloud top altitude (at 50 mbars) by determining the amount of Rayleigh scattering in the gas above the cloud tops at a wavelength of 0.365 μm. This was later confirmed by the Pioneer Venus mission which performed in-situ measurements using a nephelometer on a probe that descended through the clouds (Knollenberg and Hunten, 1980).

Polarimetry proved to be an effective technique for disentangling Venus' cloud properties because the scattering particles leave a unique angular polarization pattern in the reflected sunlight depending on the particles' micro- and macro-physical properties (for an extensive explanation of the application of polarimetry for the characterization of planetary atmospheres, see Hansen and Travis, 1974). While multiple scattered light usually has a low degree of polarization, and thus dilutes the angular polarization patterns of the singly scattered light, the angles where the absolute degree of polarization reaches a local maximum and/or where it is zero (the so-called 'neutral points') are preserved and thus still allow for the characterization of the particles.

Another factor in the successful application of (spectro)polarimetry for the characterization of Venus' clouds and hazes is that with Earth-based telescopes, inner planet Venus can be observed at a wide range of phase angles, thus allowing observations of the angular variation of the degree of polarization due to the light that has been singly scattered by the atmospheric constituents. In our solar system, only Venus, Mercury, and the Moon can be observed at a large phase angle range with Earth-based telescopes (ignoring the proximity of Mercury to the Sun). To effectively apply polarimetry to the outer planets in the solar system, a polarimeter onboard a space mission would be needed. An example of such an instrument was OCCP onboard NASA's Galileo mission (Russell et al., 1992) that orbited Jupiter. Regarding exoplanets, however, the range of observable phase angles depends on the inclination angle of the planetary orbits: for a face-on orbit, the planet's phase angle will be 90° everywhere along the orbit, while for an edge-on orbit, the phase angle will range from close to 0° (when the planetary disk is fully illuminated) to 180° (when the night-side of the planet is in view). The precise range of accessible phase angles would of course depend on the observational technique and e.g. the use of a coronagraph or star-shade.

Here we investigate the total flux and degree of polarization of starlight that is reflected by terrestrial-type exoplanets, focusing on the possible evolutionary stages of

Venus as described by Bullock and Grinspoon (2001). Our goal is to identify characteristic signatures that could help to identify the properties of exo-Venuses, thus to guide the design of future telescope instruments. We compute the disk-integrated total and polarized fluxes of light reflected between wavelengths of 0.3 to 2.5 μm. First, we study the single scattering properties of spherical cloud droplets of pure water (H_2O) or 75% sulphuric acid (H_2SO_4) in order to identify potentially distinct signatures for each particle type as a function of wavelength and planetary phase angle. Second, we compute the multiple scattered flux and polarization signals that are integrated over the planet's illuminated disk as functions of the planet's phase angle. Third, we compute the signals of the planets in the four evolutionary phases in stable orbits around the nearby solar-type Alpha Centauri A, simulating the observations of such planets if they are spatially unresolved from their parent star.

The outline of this paper is as follows. In Sect. 5.2, we define the fluxes and polarization of planets, and we describe our numerical algorithm and the four model planets in the evolutionary phases as described by Bullock and Grinspoon (2001). In Sect. 5.3, we present the total and polarized fluxes as computed for planets that are spatially resolved from their star and for planets that are spatially unresolved. In the latter case, the planet's signal is thus combined with the stellar light. We specifically assume that our model planet orbits the solar-type star Alpha Centauri A. In Sect. 5.4, we summarize our results and present our conclusions.

5.2. NUMERICAL METHOD

5.2.1. FLUX AND POLARIZATION DEFINITIONS

In this paper, we present the flux and polarization signals of starlight that is reflected by potentially habitable exoplanets that orbit solar-type stars, and in particular, Alpha Centauri A. Because these planets will be very close in angular distance to their parent star, they will usually be spatially unresolved, i.e. it will not be possible to spatially separate the planet's signal from that of its parent star. The flux vector $\mathbf{F}_\mathrm{u}$ (u= 'unresolved') that describes the light of the star and its spatially unresolved planet, and that arrives at a distant observer is then written as

$$\mathbf{F}_\mathrm{u}(\lambda,\alpha) = \mathbf{F}_\mathrm{s}(\lambda) + \mathbf{F}_\mathrm{p}(\lambda,\alpha), \tag{5.1}$$

with $\mathbf{F}_\mathrm{s}$ the star's flux vector and $\mathbf{F}_\mathrm{p}$ that of the planet. Furthermore, λ is the wavelength (or wavelength band), and α is the planetary phase angle, i.e. the angle between the star and the observer as measured from the center of the planet. We assume that the light of the star is captured together with the starlight that is reflected by the planet. A telescope with a coronagraph or star-shade would of course limit the amount of captured direct starlight, depending on its design and the angular distance between the star and the planet.

A flux (column) vector is given by (Hansen and Travis, 1974)

$$\mathbf{F} = [F, Q, U, V], \tag{5.2}$$

with F the total flux, Q and U the linearly polarized fluxes, and V the circularly polarized flux. The dimensions of F, Q, U, and V are W m^{-2}, or W m^{-3} when defined per wavelength.

Measurements of FGK-stars, such as the Sun and Alpha Centauri A, indicate that their (disk-integrated) polarized fluxes are virtually negligible (Kemp et al., 1987; Cotton et al., 2017), thus we describe the star's flux (column) vector that arrives at the observer located at a distance D as

$$\mathbf{F}_{\rm s}(\lambda) = F_{\rm s}(\lambda)\ \mathbf{1} = \frac{R_{\rm s}^2}{D^2}\ \pi B(\lambda, T_{\rm s})\ \mathbf{1}, \tag{5.3}$$

with πB the stellar surface flux, $T_{\rm s}$ the star's effective temperature, $R_{\rm s}$ the stellar radius, and $\mathbf{1}$ the unit (column) vector. The parameter values that we adopt for the Alpha Centauri A system are listed in Table 5.1.

Because of the huge distances to stars and their planets, flux vector $\mathbf{F}_{\rm p}$ of the starlight that is reflected by an exoplanet pertains to the planet as a whole, thus integrated across the illuminated and visible part of the planetary disk. It is given by (see e.g. Rossi et al., 2018)

$$\mathbf{F}_{\rm p}(\lambda,\alpha) = A_{\rm G}(\lambda)\ \mathbf{R}_{\rm p}(\lambda,\alpha)\ \frac{r_{\rm p}^2}{D^2}\frac{R_{\rm s}^2}{d^2}\ \pi B(\lambda, T_{\rm s})\ \mathbf{1} \tag{5.4}$$

$$= A_{\rm G}(\lambda)\ \mathbf{R}_{\rm 1p}(\lambda,\alpha)\ \frac{r_{\rm p}^2}{D^2}\frac{R_{\rm s}^2}{d^2}\ \pi B(\lambda, T_{\rm s}). \tag{5.5}$$

Here, $A_{\rm G}$ is the planet's geometric albedo, $\mathbf{R}_{\rm p}$ the matrix describing the reflection by the planet and $\mathbf{R}_{\rm 1p}$ its first column, $r_{\rm p}$ is the planet's radius, d the distance between the star and the planet, and D the distance to the observer. The planet's reflection is normalized such that planetary phase function $R_{\rm 1p}$, which is the first element of $\mathbf{R}_{\rm 1p}$, equals 1.0 at $\alpha = 0°$.

The contrast C between the total flux of the planet and the total flux of the star is then given by

$$C(\lambda,\alpha) = \frac{F_{\rm p}(\lambda,\alpha)}{F_{\rm s}(\lambda)} = A_{\rm G}(\lambda)\ R_{\rm 1p}(\lambda,\alpha)\frac{r_{\rm p}^2}{d^2}, \tag{5.6}$$

with $F_{\rm p}$ the first element of the planetary flux vector $\mathbf{F}_{\rm p}$. Using the parameters from Table 5.1, the contrast C between a planet with the radius of Venus at a Venus-like distance from Alpha Centauri A equals about $2\cdot10^{-9}A_{\rm G}$ at $\alpha = 0°$ (at this phase angle, the planet would actually be precisely behind the star with respect to the observer and thus out of sight).

The degree of polarization of the spatially resolved planet (without including any direct light of the star) is defined as

$$P_{\rm p} = \frac{\sqrt{Q_{\rm p}^2 + U_{\rm p}^2}}{F_{\rm p}}, \tag{5.7}$$

where we ignore the planet's circularly polarized flux $V_{\rm p}$ as it is expected to be very small compared to the linearly polarized fluxes (Rossi and Stam, 2018). We also ignore the circularly polarized fluxes in our radiative transfer computations, as this saves significant amounts of computing time without introducing significant errors in the computed total and linearly polarized fluxes (see Stam and Hovenier, 2005).

Table 5.1: The values of the parameters describing the planetary system of Alpha Centauri A used in our numerical modelling[1]

Parameter (unit)	Symbol	Value
Stellar radius ($R_{\rm Sun}$)	$R_{\rm s}$	1.2234
Stellar effective temperature (K)	$T_{\rm s}$	5790
Planet radius (km)	$r_{\rm p}$	6052
Planet orbital distance (AU)	d	0.86
Planet orbital period (yr)	P	0.76
Distance to the system (ly)	D	4.2
Angular separation (arcsecs)	S	0.67

Fluxes $Q_{\rm p}$ and $U_{\rm p}$ are defined with respect to the planetary scattering plane, which is the plane through the planet, the star and the observer. In case the planet is mirror-symmetric with respect to the planetary scattering plane, linearly polarized flux $U_{\rm p}$ equals zero and we can use an alternative definition of the degree of polarization that includes the polarization direction as follows

$$P_{\rm p} = -\frac{Q_{\rm p}}{F_{\rm p}}. \tag{5.8}$$

If $P_{\rm p} > 0$ ($P_{\rm p} < 0$), the light is polarized perpendicular (parallel) to the reference plane.

In case a planet is not completely spatially resolved from its parent star, and the background of the planet on the sky is thus filled with (unpolarized) starlight, the observable degree of polarization $P_{\rm u}$ can be written as (cf. Eqs. 5.6-5.7)

$$P_{\rm u} = \frac{\sqrt{Q_{\rm p}^2 + U_{\rm p}^2}}{F_{\rm p} + xF_{\rm s}} = \frac{F_{\rm p}}{F_{\rm p} + xF_{\rm s}}\ P_{\rm p} = \frac{C}{C+x}P_{\rm p}, \tag{5.9}$$

with x the fraction of the stellar flux that is in the background, which will depend on the angular distance between the star and the planet, on the starlight suppressing techniques that are employed, such as a coronagraph or star-shade, and on the spatial resolution of the telescope at the wavelength under consideration. This equation also holds for the signed degree of polarization as given by Eq. 5.8. If $x = 1$, the planetary and the stellar flux are measured together. In that case,

$$P_{\rm u} = \frac{C}{C+1}P_{\rm p} \approx CP_{\rm p}. \tag{5.10}$$

Here we used the fact that the contrast C will usually be very small (on the order of 10^{-9} as shown earlier).

The planet's degree of polarization $P_{\rm p}$ and the contrast C both depend on λ and α, but generally in a different way. The dependence of $P_{\rm u}$ on λ and α will thus generally differ from that of either $P_{\rm p}$ or C.

[1] The orbital distance d of the planet has been chosen such that it receives the same stellar flux as Venus receives from the Sun, and in accordance with the orbit stability requirements for a planet around Alpha Centauri A predicted by Quarles and Lissauer (2016). For the radius of the Sun, $R_{\rm Sun}$, we use 695,700 km

5.2.2. OUR RADIATIVE TRANSFER ALGORITHM

Our procedure to compute the flux vector $\mathbf{F}_p$ (Eq. 5.5) of the starlight that is reflected by the planet, is described in Rossi et al. (2018). The radiative transfer algorithm is based on an efficient adding-doubling algorithm (de Haan et al., 1987) and fully includes polarization for all orders of scattering. With this algorithm, through the use of a Fourier-series expansion of the planetary reflection matrix $\mathbf{R}_p$, the reflected flux vector can be computed for any planetary phase angle α.

Our model planetary atmospheres consist of horizontally homogeneous layers. For each layer, we prescribe the total optical thickness b, the single-scattering albedo a, and the single-scattering matrix $\mathbf{P}$. Our layered model atmosphere is bounded below by a Lambertian reflecting surface (i.e. the light is reflected isotropically and unpolarized) with an albedo $a_{\rm surf}$.

A layer's optical thickness b at a wavelength λ is the sum of the optical thicknesses of the gas molecules, $b^{\rm m}$, and, if present, the cloud particles, $b^{\rm c}$. We ignore other atmospheric particles, such as haze particles. The single-scattering matrix $\mathbf{P}$ of a mixture of gas molecules and cloud particles in a layer is given by

$$\mathbf{P}(\Theta,\lambda) = \frac{b^{\rm m}_{\rm sca}(\lambda)\,\mathbf{P}^{\rm m}(\Theta,\lambda) + b^{\rm c}_{\rm sca}(\lambda)\,\mathbf{P}^{\rm c}(\Theta,\lambda)}{b^{\rm m}_{\rm sca}(\lambda) + b^{\rm c}_{\rm sca}(\lambda)}, \tag{5.11}$$

with subscript 'sca' referring to 'scattering', thus $b_{\rm sca} = ab$, with a the single scattering albedo. Furthermore, $P^{\rm m}$ is the single-scattering matrix of the gas molecules, and $P^{\rm c}$ that of the cloud particles. Θ is the single scattering angle: $\Theta = 180^\circ - \alpha$.

We use two types of model atmospheres to study the influence of an exoplanet's atmospheric evolution on the reflected light signals: an Earth-like and a Venus-like atmosphere. For our Earth-like atmosphere, we define the pressure and temperature across 17 layers, representing a mid-latitude summer profile (following Stam, 2008). For our Venus-like atmosphere, we use 71 layers with pressure and temperature profiles from the Venus International Reference Atmosphere (VIRA) (Kliore et al., 1985), representing a mid-latitude afternoon profile. With these vertical profiles, and assuming anisotropic Rayleigh scattering (Hansen and Travis, 1974), we compute each layer's single scattering matrix $\mathbf{P}^{\rm m}$ and the scattering optical thickness $b^{\rm m}_{\rm sca}$. We neglect absorption, thus $b^{\rm m} = b^{\rm m}_{\rm sca}$. The depolarization factor for computing $\mathbf{P}^{\rm m}$ and $b^{\rm m}_{\rm sca}$ for anisotropic Rayleigh scattering depends on the atmospheric composition. For the Earth-like atmosphere, we use a (wavelength independent) depolarization factor of 0.03, which is representative for dry air, and for the Venus-like atmosphere, we use 0.09, which is representative for a pure CO_2 atmosphere (Hansen and Travis, 1974). We use wavelength-independent refractive indices of 1.00044 and 1.00027 for the Venus-like and the Earth-like model atmospheres, respectively; note that this assumption has a negligible effect on the reflected total and polarized fluxes.

The cloud particles in our model atmospheres are spherical and distributed in size according to a two-parameter gamma size distribution (see Hansen and Travis, 1974) that is described by an effective radius $r_{\rm eff}$ and an effective variance $v_{\rm eff}$. The terrestrial clouds are located between 2 and 4 km altitude, and the Venusian clouds, depending on their evolutionary phase, between 47 and 80 km. The cloud optical thickness has a uniform vertical distribution through the altitude range (see Fig. 5.1).

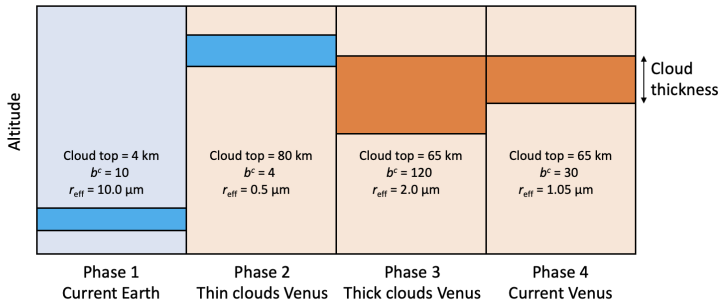

Figure 5.1: The four evolutionary phases of the model planets (Bullock and Grinspoon, 2001). In Phases 1 and 2, the clouds consist of liquid water droplets, and in Phases 3 and 4, of liquid sulfuric acid solution droplets. The cloud optical thickness is indicated by b^c and the cloud particle effective radius by r_{eff}. For the effective variance v_{eff} of the size distributions in Phases 1-3, we use 0.1, and for Phase 4, $v_{\text{eff}} = 0.07$.

The single-scattering properties of the cloud particles are computed using Mie-theory (De Rooij and Van der Stap, 1984), as these particles are expected to be spherical. For these computations we specify the wavelength λ and n_r, the refractive index of the cloud particles. The cloud particles are composed of either pure water or a sulphuric acid solution with varying concentration. We use the refractive index of water from Hale and Querry (1973) and that of sulphuric acid with 75 % acid concentration from Palmer and Williams (1975). We use a negligible value for the imaginary part of the particles' refractive indices, $n_i = 10^{-8}$.

5.2.3. CLOUD PROPERTIES THROUGH THE PLANET'S EVOLUTION

It is suspected that early Venus had a thin, Earth-like atmosphere and (possibly) an Earth-like ocean that was later lost due to the runaway greenhouse effect (Donahue et al., 1982; Kasting, 1988; Way and Del Genio, 2020). As the planet's surface heated up, the water would have evaporated and enriched the atmosphere with water vapor. The macroscopic cloud properties for the 4 evolutionary phases that we will use are illustrated in Fig. 5.1.

We start our evolutionary model of Venus assuming Earth-like conditions (Phase 1), i.e. an atmosphere consisting of 78% N_2 and 22% O_2. Model simulations showed that the actual dependence of the total and polarized flux signals on the percentage of oxygen appeared to be negligible. Hence we used the present day Earth atmosphere as the Earth-like atmosphere model while the actual percentage of oxygen on an exo-planet could be different. The cloud particles have an effective radius r_{eff} of 10 μm in agreement with ISCCP (Tselioudis, 2001) and an effective variance v_{eff} of 0.1. The total cloud optical thickness b^c is 10.0 at $\lambda = 0.55$ μm and the cloud layer extends from 2 to 4 km.

The next evolutionary phases are also inspired by the Venus climate model of Bullock and Grinspoon (2001). In Phase 2, the atmosphere is Venus-like as it consists of pure CO_2 gas, and has relatively thin liquid water clouds with $b^c = 4$, and with the cloud

tops at 80 km. For this phase, we use r_{eff} of 0.5 μm, which is smaller than the present day value, because the atmosphere is expected to be too hot for strong condensation to take place thus preventing the particles to grow larger. In Phase 3, the clouds are thick sulphuric-acid solution clouds, with $b^{\text{c}} = 120$ and the cloud tops at 65 km, because the atmosphere is cool enough to allow condensation and/or coalescence of saturated vapour over a large altitude range. Since the region of condensation covers a large altitude range, the particles can grow large until they evaporate. In this phase, $r_{\text{eff}} = 2$ μm, which is twice the effective radius of the present day Venus cloud particles. For both phases 2 and 3, we use $v_{\text{eff}} = 0.1$. In Phase 4, the clouds have the present-day properties of Venus' clouds with $b^{\text{c}} = 30$ and the cloud tops at 65 km (Rossi et al., 2015; Ragent et al., 1985). For the cloud particle sizes in this phase, we use $r_{\text{eff}} = 1.05$ μm and $v_{\text{eff}} = 0.07$ following the values derived by Hansen and Hovenier (1974). We ignore the absorption by cloud particles in the UV in all of our Venus-like clouds to avoid adding complexity and because the exact nature and location of the UV-absorption is still under debate (Titov et al., 2018).

Figure 5.2 shows the phase function (i.e. single scattering matrix element P_{11}) and the degree of linear polarization for unpolarized incident light (the ratio of single scattering matrix elements $-P_{21}/P_{11}$) that has been singly scattered by the four different types of cloud particles as functions of α (i.e. 180° - Θ), for a range of wavelengths λ.

As can be seen in Fig. 5.2, the phase functions show strong forward scattering peaks (near $\alpha = 180°$, thus when the night-side of the planet would be turned towards the observer) that decrease with increasing λ, thus with decreasing effective particle size parameter $x_{\text{eff}} = 2\pi r_{\text{eff}}/\lambda$ (for the large H_2O cloud particles, with $r_{\text{eff}} = 10$ μm, this decrease is not readily apparent from the figure). The H_2O particles with $r_{\text{eff}} = 10$ μm show a moderate local maximum in the phase function around $\alpha = 40°$, which is usually referred to as the primary rainbow (see e.g. Hansen and Travis, 1974). The large H_2O and the H_2SO_4 particles also produce higher fluxes towards $\alpha = 0°$ that are referred to as the glory (Laven, 2008; García-Muñoz et al., 2014; Markiewicz et al., 2014; Rossi et al., 2015; Markiewicz et al., 2018). For the small H_2O particles and the H_2SO_4 particles at larger wavelengths, the phase functions become more isotropic and the glory and other angular features disappear.

Figure 5.2 also shows the degree of linear polarization of the singly scattered light. This degree of polarization appears to be more sensitive to the particle composition than the scattered flux, especially for λ between 0.5 and 2 μm, where H_2O particles yield relatively high positive degrees of polarization (perpendicular to the scattering plane) between phase angles of about 20° and 100°, whereas the H_2SO_4 particles impart a mostly negative degree of polarization through a broad range of phase angles, except for narrow regions around $\alpha = 20°$ and 80°. The tiny, $r_{\text{eff}} = 0.5$ μm, water droplets have a strong, broad positive polarization region for $\lambda \geq 1$ μm, where they are so small with respect to the wavelength that they scatter like Rayleigh scatterers.

As mentioned before (see e.g. Hansen and Travis, 1974; Hansen and Hovenier, 1974), patterns in the single scattering degree of polarization are generally preserved when multiple scattered light is added, as the latter usually has a low degree of polarization, and thus adds mostly total flux, which subdues angular features, but does not change the angular pattern (local maxima, minima, neutral points) itself. The single scattering

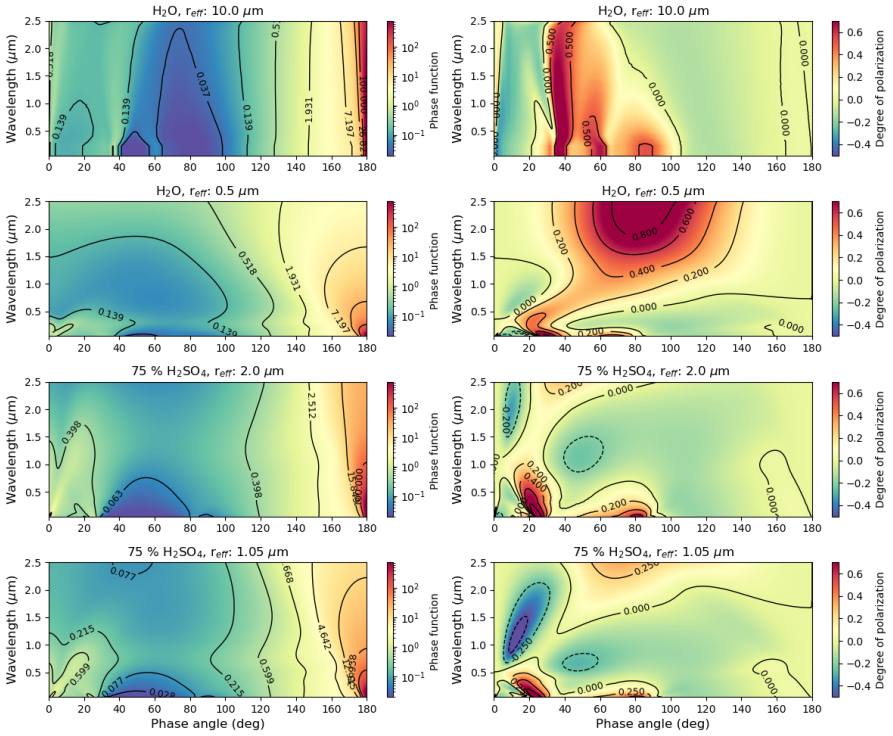

Figure 5.2: The total flux and degree of polarization of incident unpolarized light that has been singly scattered by four different types of cloud particles, as functions of the phase angle α and the wavelength λ. Left column: the total flux or phase function (single scattering matrix element P_{11}). Right column: the degree of polarization ($-P_{21}/P_{11}$). First row: H_2O particles with $r_{\rm eff} = 10$ μm and $v_{\rm eff} = 0.1$ (belonging to the Phase 1 model planet: 'Current Earth'); Second row: H_2O particles with $r_{\rm eff} = 0.5$ μm and $v_{\rm eff} = 0.1$ (Phase 2: 'Thin clouds Venus'); Third row: 75% H_2SO_4 particles with $r_{\rm eff} = 2.0$ μm and $v_{\rm eff} = 0.1$ (Phase 3: 'Thick clouds Venus'); Fourth row: 75% H_2SO_4 particles with $r_{\rm eff} = 1.05$ μm and $v_{\rm eff} = 0.07$ (Phase 4: 'Current Venus').

angular features in the polarization will thus also show up in the polarization signature of a planet as a whole, and can be used for characterisation of the cloud particle properties and thus possibly of various phases in the evolution of a Venus-like exoplanet. This will be investigated in the next section.

5.3. RESULTS

Here we present the disk-integrated total flux and degree of polarization of incident unpolarized starlight that is reflected by the model planets at different wavelengths λ and for phase angles α ranging from 0° to 180°. The actual range of phase angles at which an exoplanet can be observed depends on the inclination angle i of the planet's orbit (the angle between the normal on the orbital plane and the direction towards the observer): α ranges between $90° - i$ to $90° + i$. Obviously, at $\alpha = 0°$, the planet would be precisely behind its star, and at 180° it would be precisely in front of its star (in transit).

Other phase angles might be inaccessible due to restrictions of inner working angles of telescopes and/or instruments. For completeness, we include all phase angles in our computations.

Section 5.3.1 shows results for spatially resolved planets and Sect. 5.3.2 for planets that are spatially unresolved from their star. In particular, we show these latter results for a model planet orbiting the star Alpha Centauri A at a distance where the incident stellar flux is similar to the solar flux that reaches Venus. Because our model planets are all mirror-symmetric with respect to the reference plane, their linearly polarized flux U_p equals zero and will not be discussed further.

5.3.1. FLUX AND POLARIZATION OF SPATIALLY RESOLVED PLANETS

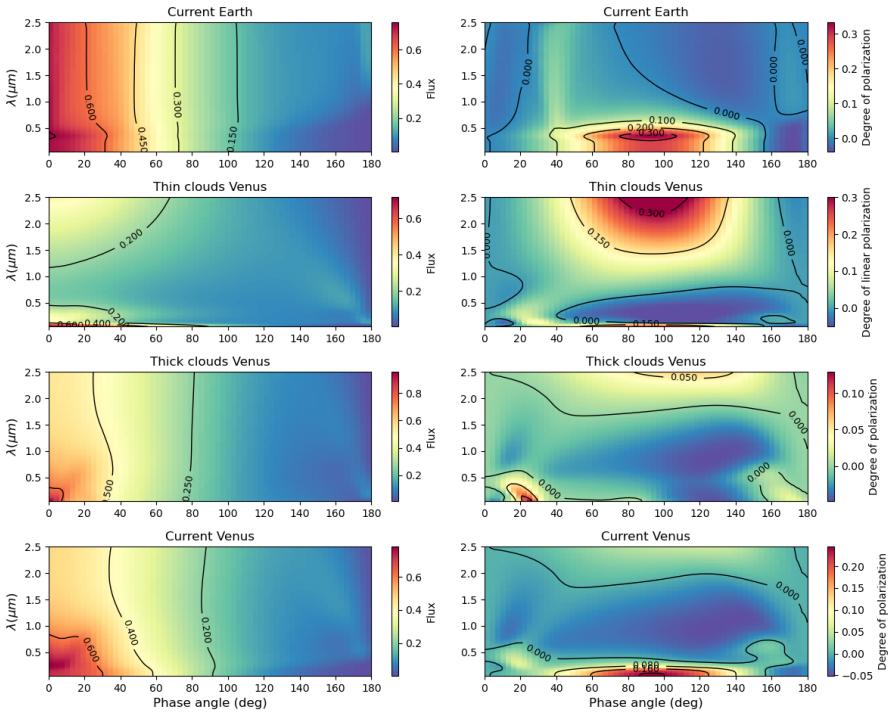

Figure 5.3: Left column: The total flux (or phase function); and right column: The degree of polarization of incident unpolarized starlight that is reflected by the model planets in the 4 evolutionary phases as functions of α and λ. First row: Phase 1 ('Current Earth'); Second row: Phase 2 ('Thin clouds Venus'); Third row: Phase 3 ('Thick clouds Venus'); Fourth row: Phase 4 ('Current Venus'). The phase functions are normalised such that at $\alpha = 0°$, they equal the planet's geometric albedo A_G.

Figure 5.3 shows the total flux F_p (the planetary phase function) and degree of polarization P_p as functions of α and λ for the four evolutionary phases illustrated in Fig. 5.1. The total fluxes are normalized such that at $\alpha = 0°$, they equal the planet's geometric albedo A_G (see Eq. 5.5). Figure 5.4 shows A_G of the planets in the four evolutionary phases as functions of the wavelength λ. Table 5.2 lists the geometric albedo's at 0.5, 1.0,

1.5 and 2.0 μm. The 'Current Earth' (Phase 1) shows very little variation in A_G, and the 'Thin clouds Venus' (Phase 2) has the lowest albedo because of the small cloud particles and the small cloud optical thickness. The geometric albedo's of the 'Thick clouds Venus' (Phase 3) and the 'Current Venus' (Phase 4) are very similar. Thus across the wavelength region investigated in this paper, the 'Current Earth' (Phase 1) has the highest geometric albedo.

Table 5.2: The model planets' geometric albedo's A_G for the four evolutionary phases at four wavelengths.

λ (μm)	0.5	1.0	1.5	2.0
Current Earth	0.757	0.752	0.740	0.739
Thin clouds Venus	0.186	0.184	0.240	0.310
Thick clouds Venus	0.727	0.627	0.580	0.564
Current Venus	0.726	0.573	0.500	0.484

For each model planet, the total flux F_p decreases with increasing α mostly because less of the planet's observable disc is illuminated. The planet with thin H_2O clouds (Phase 2) is very dark over all α's because the cloud optical thickness b^c is small and the surface is black. The total fluxes show vague similarities with the single scattering phase functions of the cloud particles (Fig. 5.2). In particular, for the 'Current Earth' (Phase 1) with large H_2O particles, F_p increases slightly around $\alpha = 40°$, the rainbow angle. Also, the decrease of F_p with λ is stronger for the Venus-type planets with H_2SO_4 clouds (Phases 3 and 4) than for the planet with the large H_2O particles ('Current Earth', Phase 1), because the single scattering phase function of the sulfuric acid particles decreases stronger with λ than that of the water droplets (see Fig. 5.2).

Unlike F_p, the degree of polarization P_p of each of the model planets, shows angular and spectral features that depend strongly on the cloud properties and should thus allow distinguishing between the different evolutionary phases. In Phase 1 ('Current Earth'), P_p is high and positive up till $\lambda = 0.5$ μm and around $\alpha = 90°$, which is due to Rayleigh scattering by the gas above the clouds. Starting at the shortest λ, P_p increases

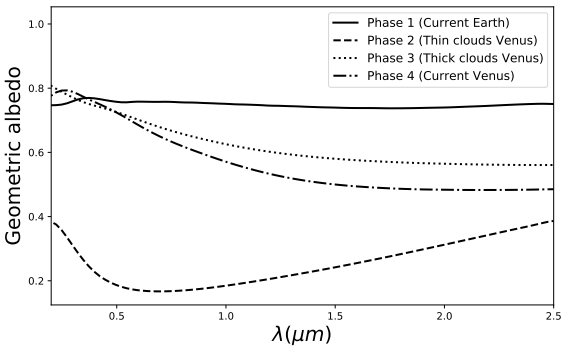

Figure 5.4: The planets' geometric albedo's A_G as functions of the wavelength λ for the four evolutionary phases.

slightly with λ before decreasing. This is due to the slightly larger contribution of multiple scattered light, with a lower degree of polarization, at the shortest wavelengths. A Rayleigh-scattering peak is also seen for Phase 4 ('Current Venus'), except there, the peak decreases more rapidly with λ because the clouds are higher in the atmosphere and there is thus less gas above them. In Phase 3 ('Thick clouds Venus'), the Rayleigh-scattering peak is suppressed by the contribution of low polarized light that is reflected by the thicker clouds below the gas. In Phase 2 ('Thin clouds Venus'), the relatively thin clouds are higher in the atmosphere than in Phase 1 ('Current Earth'), which is why the Rayleigh-scattering peak only occurs at the very shortest wavelengths (the peak is hardly visible in Fig. 5.3). Because the Phase 2 cloud particles are small ($r_{\rm eff}$ = 0.5 μm), they themselves give rise to a Rayleigh-scattering peak at $\lambda \geq 1.0$ μm.

The two model planets with the H_2O cloud particles (Phases 1 and 2) show a narrow region of positive polarization between 30° and 40°, which is the rainbow peak (see Fig. 5.2). On exoplanets, this local maximum in $P_{\rm p}$ could be used to detect liquid water clouds on exoplanets (Karalidi et al., 2011, 2012; Bailey, 2007). In Phase 1 ('Current Earth'), the rainbow region starts near the Rayleigh scattering peak of the gas and extends towards the largest wavelengths. In Phase 2 ('Thin clouds Venus'), with the small water droplets, the rainbow only occurs at the shortest wavelengths. With increasing wavelength, it broadens and disappears into the cloud particles' Rayleigh scattering peak.

The H_2SO_4 cloud particles (Phases 3 and 4) have their own specific polarization patterns, such as the broad negative polarization region at $\alpha \gtrapprox 80°$, which can be traced back to their single scattering patterns (Fig. 5.2). In Phase 3 ('Thick clouds Venus'), the cloud particles give rise to a sharp positive polarization peak at the shortest wavelengths and for $20° \leq \alpha \leq 30°$. In Phase 4 ('Current Venus'), there is a broader, lower, positive polarization branch across this phase angle range, which resembles the positive polarization branch of the tiny H_2O droplets in Phase 2 ('Thin clouds Venus'). However, at the longer wavelengths, the phase angle dependence of the polarization of the latter planet is very different which should help to distinguish between such planets. This emphasizes the need for measurements at a wide range of wavelengths and especially phase angles (if the planet's orbital inclination angle allows this).

5.3.2. FLUX AND POLARIZATION OF SPATIALLY UNRESOLVED PLANETS

In the previous section, we showed the signals of spatially resolved planets, thus without background starlight. When observing an exoplanet in the habitable zone of a solar-type star, it will be difficult to avoid the starlight. Here, we show the total flux of the planet $F_{\rm p}$, the star-planet contrast C (see Eq. 5.6), the spatially resolved degree of polarization of the planet $P_{\rm p}$ (thus without the starlight) and the spatially unresolved degree of polarization of the combined star-planet signal $P_{\rm u}$ (thus including the starlight). While the total planet fluxes shown in Fig. 5.3 were normalized at $\alpha = 0°$ to the planets' geometric albedo's $A_{\rm G}$, here they are computed according to Eq. 5.5, and thus depend on the parameters of the planet-star system. We assume our model planets orbit Alpha Centauri A.

The solar-type star Alpha Centauri A is part of a double star system, and the orbital parameters of ourplanets are chosen based on the stable planet orbital distances and orbital inclination angles around this star as predicted by Quarles and Lissauer (2016).

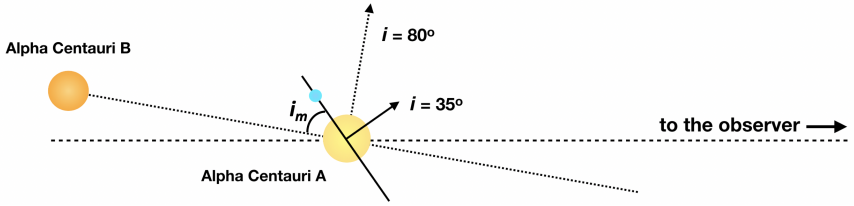

Figure 5.5: A sketch of the geometries within the Alpha Centauri system: the orbital plane of the stars Alpha Centauri A and B is inclined by about 80° with respect to the observer on Earth. Our model planet (the blue dot) orbits Alpha Centauri A. In this sketch, the line of nodes of the planet's orbit was chosen to coincide with that of the stellar orbits. The inclination angle $i_{\rm m}$ of the planet's orbit with respect to the stellar orbital plane is 45°, and the inclination angle of the planet's orbit with respect to the observer is $80° - 45° = 35°$. The phase angles of the planet in this sketch would range from $90° - 35° = 55°$ to $90° + 35° = 125°$.

Figure 5.5 shows a sketch of the system. We use a planetary orbital distance d of 0.86 AU, such that each model planet receives a stellar flux similar to the solar flux received by Venus. Additional system parameter values are listed in Table 5.1. According to Quarles and Lissauer (2016), stable orbits around Alpha Centauri A can be found for a range of angles between the planetary orbital plane and the plane in which the two stars orbit, and thus for a range of inclination angles i of the planetary orbit.

Figure 5.6 shows the variation of the planetary phase angle α along a planetary orbit for two values of the longitude of the orbit's ascending node Ω: for $\Omega = 0°$ (the line connecting the planet's ascending and descending nodes is perpendicular to the line to the observer) and for $\Omega = 205°$ which represents the configuration of Earth with Alpha Centauri A. The orbital phase of the planet is defined such that at an orbital phase angle of 0°, $\alpha = 180°$. The inclination angle $i_{\rm m}$ is the angle between the plane in which the stars move and the planetary orbital plane. For $\Omega = 0°$, $i_{\rm m} = -10°$ would yield a face-on planetary orbit ($i = 0°$) with $\alpha = 90°$ everywhere along the orbit. For $i_{\rm m} = 80°$, the orbit is edge-on ($i = 90°$) and α varies between 0° and 180°. Figure 5.6 also shows the

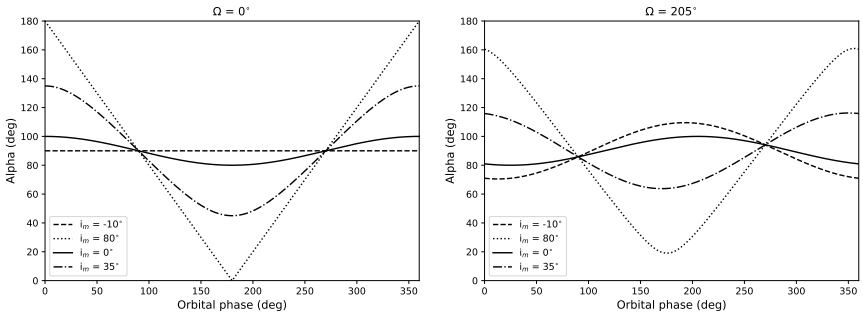

Figure 5.6: Variation of the planet's phase angle α along the planet's orbit around Alpha Centauri A for different mutual inclination angles $i_{\rm m}$ of the planetary orbit with respect to the orbital plane of the two stars. Top: Ω, the longitude of the ascending node of the planet's orbit, is 0°. For $i_{\rm m} = -10°$, the planet is then in a face-on orbit ($i = 0°$), while for $i_{\rm m} = 80°$, it is in an edge-on orbit ($i = 90°$). Bottom: $\Omega = 205°$, and the planetary orbit is aligned with the node of the stellar orbital plane.

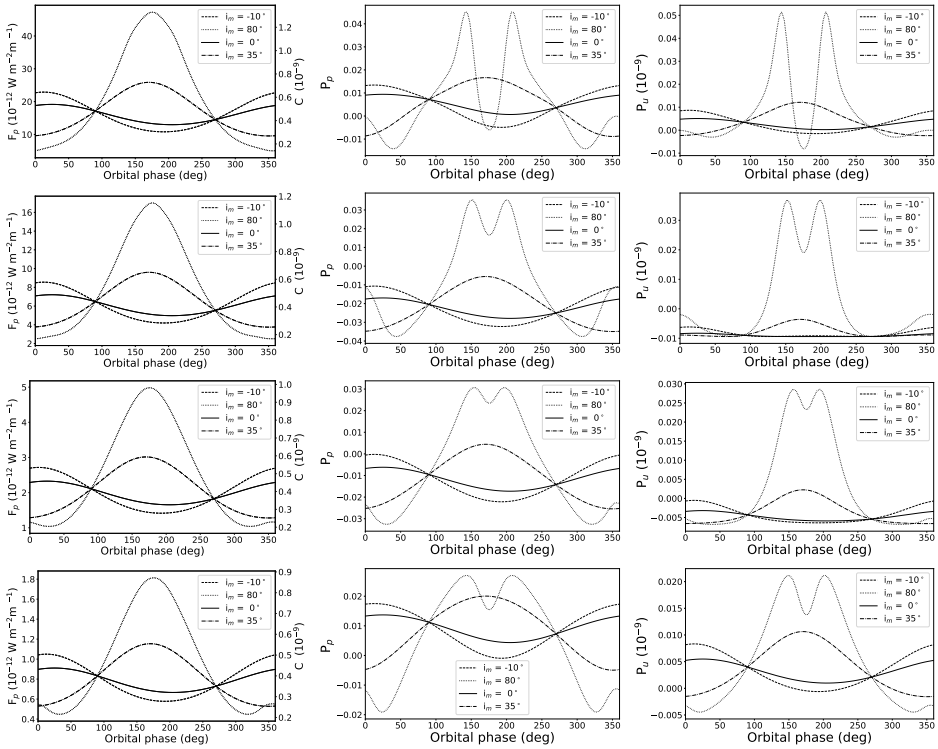

Figure 5.7: The total planetary flux F_p (in W m^{-3}) and the star-planet contrast C, the degree of polarization P_p of the spatially resolved planet, and P_u, the degree of polarization of the star and the spatially unresolved planet, all for a 'Current Venus' model planet (Phase 4) as functions of the planet's orbital phase for four mutual inclination angles i_m and four wavelengths λ: 0.5 μm (row 1); 1.0 μm (row 2); 1.5 μm (row 3); and 2.0 μm (row 4). The longitude of the ascending node of the planetary orbit, Ω, is 205°.

range of α for $i_m = 0°$ and 35°. According to Quarles and Lissauer (2016), the latter is the most probable orientation of a stable planetary orbit. For these two cases, the accessible phase angles range from 80° to 100°, and from 45° to 135°, respectively. For $\Omega = 205°$, the maximum range of α would be from 20° to 160°, depending on i_m.

Figure 5.7 shows F_p, P_p and P_u (the spatially unresolved planet, thus with starlight included) for Phase 4 ('Current Venus') as functions of the planet's orbital phase for Ω = 205°, four values of i_m (-10°, 80°, 0°, and 35°), and four wavelengths (0.5, 1.0, 1.5, and 2.0 μm). The plots for F_p also show the contrast C. Because C is the ratio of the planetary flux F_p to the stellar flux F_s (Eq. 5.6), its variation with the orbital phase is proportional to that of F_p.

At the two orbital phases in each plot where all the lines cross, the planetary phase angles α are the same (see Fig. 5.6) and thus all F_p and P_p are the same. The plots for F_p appear to be very similar for the different wavelengths, apart from a difference in magnitude which is mainly due to the decrease of the stellar flux that is incident on the planet with increasing wavelength, although the planetary albedo A_G and phase function R_{1p}

also decrease with increasing λ as can be seen in Fig. 5.3. This wavelength dependence of F_p also causes the decrease of the contrast C with increasing wavelength (i.e. the planet darkens with increasing λ), as C is independent of the wavelength dependence of the stellar flux (see Eq. 5.6). The shape differences between the F_p (and C) curves are due to the wavelength dependence of the planetary flux that can also be seen in Fig. 5.3.

At each wavelength λ, the largest variation in F_p with the orbital phase is seen for $i_m = 80°$, because for that configuration the variation of α along the orbit is largest (see Fig. 5.6). The degree of polarization P_p of the planet shows significant variation with the orbital phase at all wavelengths. A particularly striking feature for the geometry with $i_m = 80°$ is the double peak close to the orbital phases of 150° and 200°. As can be seen in Fig. 5.6 for $\Omega = 205°$ and $i_m = 80°$, α decreases from about 160° at an orbital phase of 0°, to 20° at an orbital phase around 175°, to then increase again with increasing orbital phase. Tracing this path of α through the P_p panel in the bottom row of Fig. 5.3 explains the double peaked behaviour of P_p and its wavelength dependence as shown in Fig. 5.7. For the other values of i_m, the phase angle range that is covered along the orbit is smaller, and therefore the variation in P_p is also smaller.

The degree of polarization of the spatially unresolved planet, P_u, shows similar variations along the orbital phase as P_p, except that most features are flattened out because of the addition of the unpolarized stellar flux, which is independent of the orbital phase angle. The double peaked feature for $i_m = 80°$ remains strong, however, as at those orbital phase angles, the contrast C is relatively large and thus the influence of the added stellar flux relatively small. The variation in the polarisation of the unresolved system due to the orbiting planet is on the order of 10^{-11}.

Figure 5.8 is similar to Fig. 5.7, except for the four model planets in the different evolutionary phases and all for $i_m = 80°$ and $\Omega = 0°$. Because here the planetary orbits are seen edge-on ($i = 90°$), the full range of phase angles is covered, which makes it possible to explore the full extent of variation of flux and polarization signals. Because of this large phase angle range, F_p varies strongly with the orbital phase. The wavelength dependence of the total flux can be traced back to Fig. 5.3, where in particular the Phase 2 planet ('Thin cloud Venus') is dark at all wavelengths, but relatively bright at the longest wavelengths and small phase angles. As was the case in Fig. 5.7, the variation of C is the same as that of F_p, except for the off-set due to the stellar flux. The largest values of C (about 1.6×10^{-9}), are found for $\lambda = 0.5$ μm and around the orbital phase of 180° (at 180°, the planets would actually be behind the star).

Furthermore in Fig. 5.8, P_p depends strongly on λ and the planet's evolutionary phase. At 0.5 μm, the Phase 1 planet ('Current Earth') shows the largest values of P_p due to the Rayleigh scattering gas above the low altitude clouds. At the longer wavelengths, where the Rayleigh scattering is less prominent, the curves for the Phase 1 planet clearly show the positive polarization of the rainbow around the orbital phases of 140° and 220° (see Fig. 5.6). For the Phase 2 planet ('Thin clouds Venus') and 0.5 μm, the small cloud particles cause positive polarization around 150° and 210°, which connect the rainbow and the Rayleigh scattering maximum in Fig. 5.3. At longer wavelengths, the broad positive polarization signature of Rayleigh scattering by the cloud particles dominates the curves, while the curves for the Phase 3 and 4 planets show mostly negative polarization apart from the orbital phases around 180°. When adding the starlight, the angular features of

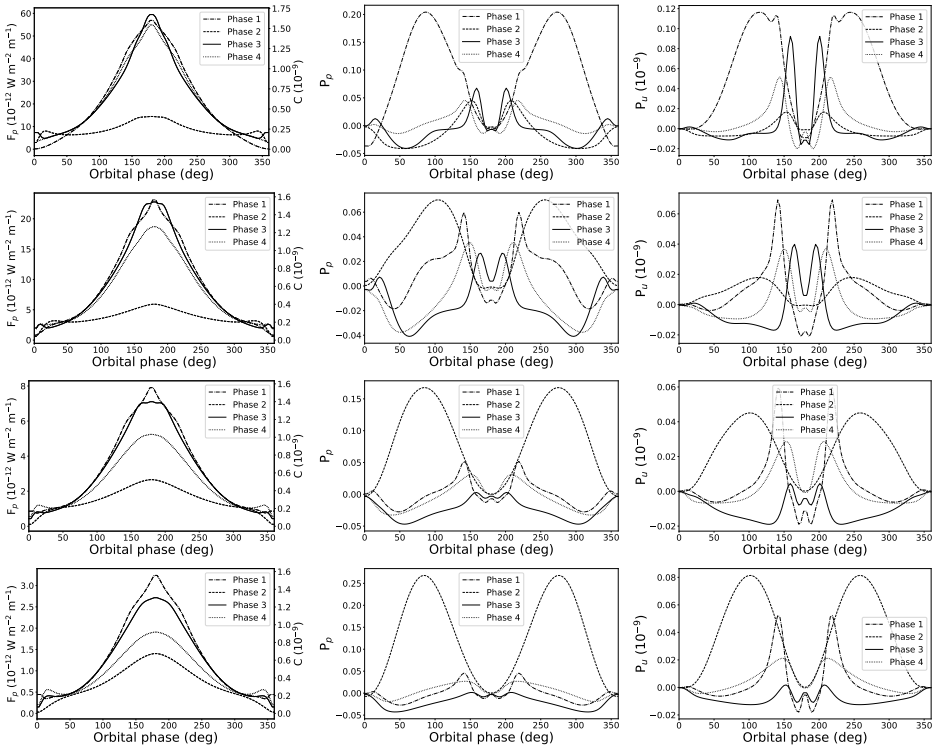

Figure 5.8: Similar to Fig. 5.7 except for the model planets in the four evolutionary phases and $\Omega = 0°$ and $i_m = 80°$ (thus for an edge–on orbit, $i = 90°$): Phase 1 ('Current Earth'), Phase 2 ('Thin clouds Venus'), Phase 3 ('Thick clouds Venus'), Phase 4 ('Current Venus'). The wavelengths λ are like before: 0.5 μm (row 1); 1.0 μm (row 2); 1.5 μm (row 3); and 2.0 μm (row 4).

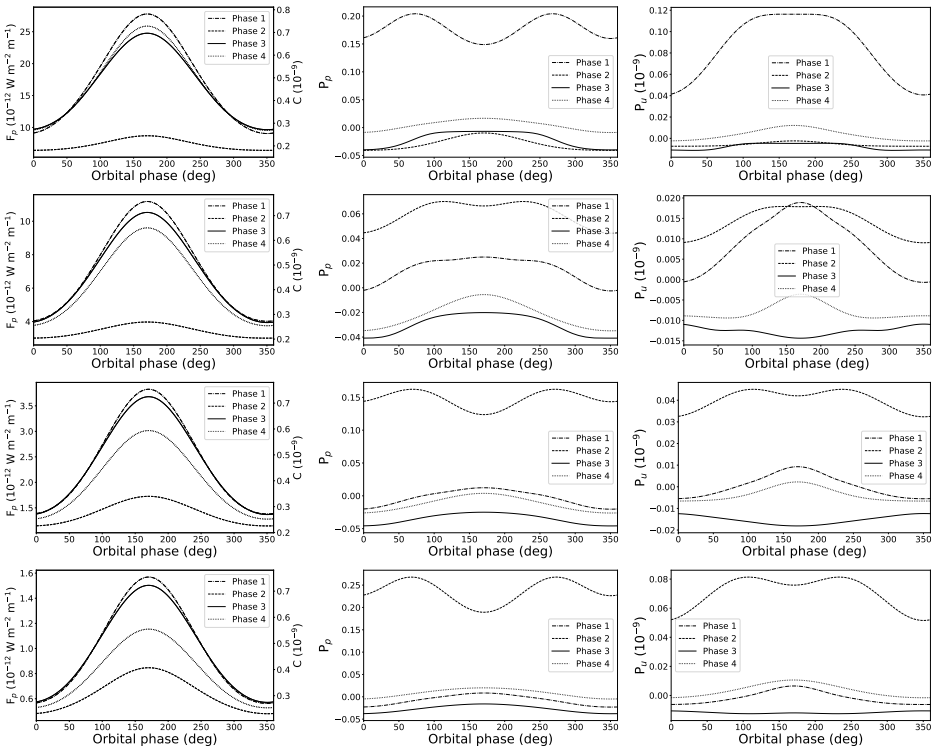

Figure 5.9: Similar to Fig. 5.8 except for the most probable, stable orbit around Alpha Centauri A, i.e. for Ω = 205° and i_m= 35° (Quarles and Lissauer, 2016). The wavelengths are like before: 0.5 μm (row 1); 1.0 μm (row 2); 1.5 μm (row 3); and 2.0 μm (row 4).

the polarization P_u are suppressed along those parts of the orbits where C is smallest, thus away from the orbital phase angle of 180°. In particular within 180° ±40°, P_u still shows distinguishing features, although they are very small in absolute sense (smaller than 10^{-10}).

Figure 5.9 is similar to Fig. 5.8 except here the model planets are in the most probable stable orbit around Alpha Centauri A as predicted by Quarles and Lissauer (2016), namely with $\Omega = 205°$ and $i_m = 35°$. As can be seen in Fig. 5.6, for this geometry α varies between about 60° and 120°. In Fig. 5.9, F_p shows a similar variation as the curves in Fig. 5.8, although less prominent, as the planets do not reach a 'full' phase (where $\alpha = 0°$) nor the full night phase ($\alpha = 180°$) along their orbit. The flux curves in Fig. 5.9 also miss small angular features that appear in the single scattering phase functions of the cloud particles (see Fig. 5.2), such as the glory, again because the planets do not go through the related phase angles.

In this particular orbital geometry, P_p shows less pronounced angular features than for the same model planets in edge-on orbits (Fig. 5.8) because of the more limited phase angle range. For example, the 'Current Earth' (Phase 1) shows no rainbow despite the H_2O clouds, because the phase angle of about 40° is not reached. In the visible ($\lambda = 0.5$ μm), P_p reaches the largest values for the 'Current Earth' (Phase 1). At longer wavelengths, P_p of the 'Thin clouds Venus' (Phase 2) strongly dominates because of the Rayleigh scattering by the small cloud particles. The 'Thick clouds Venus' (Phase 3) shows predominant negative polarization at all wavelengths and across the whole orbital phase angle range except at $\lambda = 0.5$ μm around an orbital phase angle of 20°.

The polarization of the spatially unresolved planets, P_u, clearly shows the suppression of the polarization features due to the added starlight towards the smaller and larger orbital phase angles, where the planets are darker. While the Phase 2 planet ('Thin clouds Venus') is relatively dark (C is very small), its Rayleigh scattering polarization signal is so strong that its unresolved polarization signal is larger than that of the other planets, except the Phase 1 planet ('Current Earth') at 1.0 μm and orbital phase angles close to 180°.

5.3.3. EVOLUTIONARY PHASES ACROSS α AND λ

In Fig. 5.10, we show which evolutionary phase has the highest values of $|P_p|$ across all phase angles α and wavelengths λ. We find that $|P_p|$ of the Phase 1 planet ('Current Earth') dominates between 30° and 150°, and mostly for $\lambda < 1.0$ μm. In particular, around $\alpha = 40°$ and up to $\lambda = 2.0$ μm, the polarization signal of the rainbow produced by the large water cloud particles is about 0.1 (see the bottom plot of Fig. 5.10). For $\lambda > 1.0$ μm, the Phase 2 planet ('Thin clouds Venus') shows the strongest polarization due to the Rayleigh scattering by the small H_2O cloud particles, as can clearly be seen in the bottom plot. The small patches where the strongest polarization signal is from the 'Thick clouds Venus' (Phase 3), for example near $\alpha = 20°$ and $\lambda < 1.0$ μm, or from the 'Current Venus' (Phase 4) are due to the single scattering polarization features of the H_2SO_4 cloud particles, as can be seen in Fig. 5.2.

The accessible phase angle range for direct observations of such exoplanets obviously depends on the actual orientation of the planetary orbits and cannot be optimized by the observer. Precisely because of that, Fig. 5.10 clearly indicates that measurements should be performed across a broad wavelength range, including wavelengths below

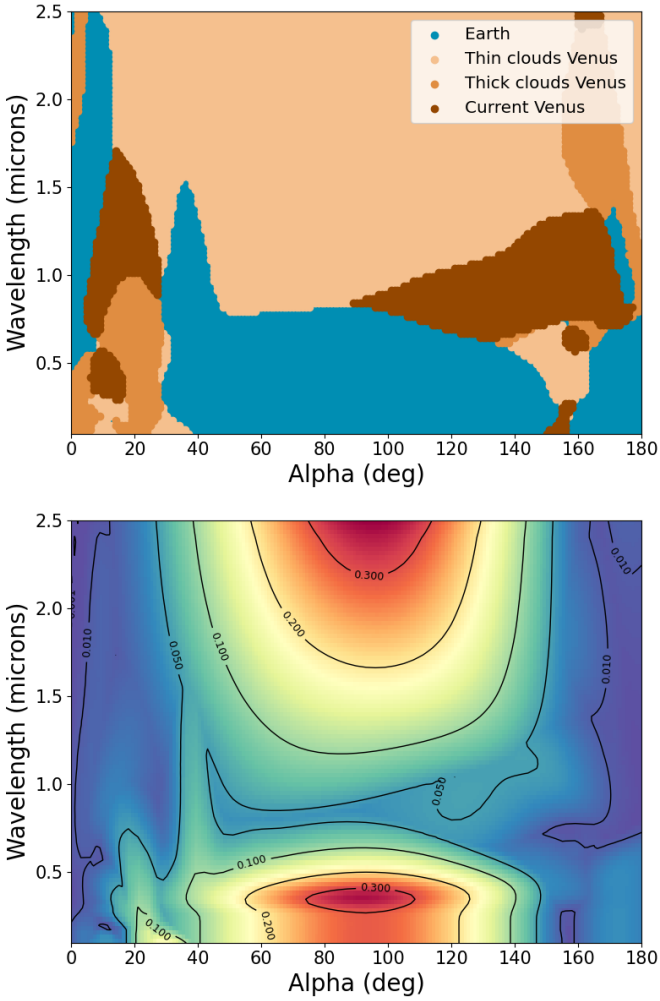

Figure 5.10: Top: The planet models that yield the largest absolute degree of polarization $|P_p|$ over all phase angles α and wavelengths λ: Phase 1 - 'Current Earth' (blue); Phase 2 - 'Thin clouds Venus' (light orange); Phase 3 - 'Thick clouds Venus' (dark orange); and Phase 4 - 'Current Venus' (brown). Bottom: The maximum values of $|P_p|$ of the four model planets as functions of α and λ.

1 μm to allow distinguishing between Earth-like and Venus-like planets in various evolutionary phases.

5.4. SUMMARY AND CONCLUSIONS

We presented the total flux and linear polarization of starlight that is reflected by model planets of various atmospheric types to investigate whether different phases in the evolution of planets like the Earth and Venus can be distinguished from each other. We have used four planet models to represent possible evolutionary phases. Phase 1 ('Current Earth') has an Earth-like atmosphere and liquid water clouds; Phase 2 ('Thin clouds Venus') has a Venus-like CO_2 atmosphere and thin water clouds; Phase 3 ('Thick clouds Venus') has a Venus-like CO_2 atmosphere and thick sulphuric acid solution clouds; and Phase 4 ('Current Venus') has a CO_2 atmosphere and thin sulphuric acid solution clouds. We have computed the total flux and polarization signals specifically for model planets orbiting our neighbouring solar-type star Alpha Centauri A using predicted stable orbits (Quarles and Lissauer, 2016) in its habitable zone.

We have computed the reflected starlight for wavelengths λ ranging from 0.3 μm to 2.5 μm and for planetary phase angles α from 0° to 180°. We not only present the fluxes and polarization of spatially resolved model planets (thus without background starlight) but also of spatially unresolved planets, thus the combined signal of the planet and the star. For the latter cases, we also computed the planet-star contrast C as a function of α and λ to determine what would technically be required to detect the planetary signals upon the background starlight.

The range of planetary phase angles α at which a planet can be observed (spatially resolved or unresolved) depends on the inclination of the planetary orbit with respect to the observer. We have specifically studied the reflected light signals of planets orbiting solar-type star Alpha Centauri A. This star is part of a double star system with solar-type star Alpha Centauri B. The distance between the two stars varies from 35.6 to 11.2 AU (M-dwarf Alpha Centauri C or Proxima Centauri orbits the pair at a distance of about 13,000 AU). Dynamical computations (Quarles and Lissauer, 2016) predict stable planetary orbits around Alpha Centauri A in a narrow range of mutual inclination angles i_m between the orbital planes of the two stars and that of the planet. In particular, the most stable orbit has $i_m = 35°$, which provides an α range from 60° to 120°. We find that with this orbital geometry the degree of polarization of the planet would be largest for the 'Current Earth' (Phase 1) across the visible ($\lambda < 1.0$ μm) due to Rayleigh scattering by the gas above the clouds. At near infrared wavelengths (1.0 μm $< \lambda <$ 2.5 μm), the polarization of the 'Thin clouds Venus' (Phase 2) is highest, because this planet has small cloud droplets that scatter like Rayleigh scatterers at the longer wavelengths.

The well-known advantage of measuring the degree of polarization for the characterization of (exo)planets is that the angular features in the signal of the planet as a whole are similar to the angular features in the light that has been singly scattered by the gas molecules and cloud particles, which are very sensitive to the microphysical properties (such as the size distribution, composition, shape) of the scattering molecules and cloud particles and to the atmosphere's macrophysical properties (such as cloud altitude and thickness). The reflected total flux is much less sensitive to the atmospheric properties than the degree and direction of polarization (see e.g. Hansen and Travis, 1974, for

several examples). Indeed, the variations of the planetary flux F_p along a planet's orbit appear to be mostly due to the change of the fraction of the planetary disk that is illuminated and visible to the observer. They provide limited information on the planet's atmospheric characteristics, especially if one takes into account that with real observations, the planet radius will be unknown unless the planet happens to transit its star. The variation of the planetary flux F_p with phase angle α and wavelength λ is similar that of planet-star contrast C, the ratio of F_p to the stellar flux F_s. For a Venus-like planet orbiting Alpha Centauri A, C is on the order of 10^{-9}.

Our numerical simulations show that variations in P_p, the degree of polarization of the spatially resolved planets (thus without any starlight), with α combined with variations with λ could be used to distinguish the planetary evolutionary phases explored in this paper:

- Phase 1 planets ('Current Earth') show strong positive (perpendicular to the reference plane through the star, planet, and observer) polarization around $\alpha = 40°$ due to scattering by large water cloud droplets (the rainbow) and also higher polarization for $\lambda < 0.5$ μm and $\alpha \approx 90°$ due to Rayleigh scattering by the gas above the clouds.

- Phase 2 planets ('Thin clouds Venus') polarize light negatively (parallel to the reference plane) across most phase angles and at visible wavelengths. At near-infrared wavelengths, they have strong positive polarization around $\alpha = 90°$ due to Rayleigh scattering by the small cloud droplets, and a 'bridge' of higher polarization from the Rayleigh maximum to the rainbow angle ($\alpha \approx 40°$) with decreasing λ.

- Phase 3 planets ('Thick clouds Venus') have predominantly negative polarization from the visible to the near-infrared, with small regions of positive polarization for $\lambda < 1.0$ μm and for $20° \leq \alpha \leq 30°$, that are characteristic for the 75% H_2SO_4 cloud particles with $r_{eff} = 2.0$ μm.

- Phase 4 planets ('Current Venus') yield similar polarization patterns as the Phase 3 planets, except with more prominent negative polarization for $10° \leq \alpha \leq 30°$ and for 0.5 μm $\leq \lambda \leq 2$ μm. Rayleigh scattering by the small cloud particles produces a maximum of positive polarization around $\alpha = 90°$ and for $\lambda > 2$ μm.

Our simulations of the planetary polarisation P_p do not include any background starlight, and can thus reach several percent to even 20% for the 'Current Earth' (Phase 1) planet in an edge-on orbit (Fig. 5.8). Whether or not such polarization variations could be measured depends strongly on the techniques used to suppress the light of the parent star. If the background of the planet signal contains a fraction x of the flux of the star, the degree of polarization of the light gathered by the detector pixel that contains the planet will equal $(C/(C+x))P_p \approx (C/x)P_p$ with C the contrast between the total fluxes of the planet and the star (Eq. 5.9). For a Venus-like planet orbiting Alpha Centauri A, C is on the order of 10^{-9}, thus x should be as small as 10^{-4} to get a polarisation signal on the order of 10^{-6}, assuming P_p is about 0.1. Not only excellent direct starlight suppression techniques, but also a very high spatial resolution would help to decrease x.

Our simulations further show that temporal variations in the total flux F_u of Alpha Centauri A with a spatially unresolved terrestrial-type planet orbiting in its habitable

zone would be less than 10^{-12} W/m^3. The degree of polarization P_u of the combined star and planet signals, would show variations smaller than 0.05 ppb. To identify this planetary flux on top of the stellar flux, a very high-sensitivity instrument would be required and an even higher sensitivity would be required to subsequently characterize the planetary atmosphere. Recall that the orbital period of such a planet, and with that the period of the signal variation and presumably the stability requirements of an instrument, would be about 0.76 years. Bailey et al. (2018) computed the polarization signal of spatially unresolved, hot, cloudy, Jupiter-like planet HD 189733b to be on the order of ~20 ppm. Because of their large size, Jupiter-like planets, and in particular those in close-in orbits that receive large stellar fluxes, would clearly be less challenging observing targets than terrestrial-type planets.

The HARPS instrument on ESO's 3.6 m telescope includes polarimetric observations with a polarimetric sensitivity of 10^{-5} (Snik et al., 2010). Planetpol on the 4.2 m William Herschel Telescope (WHT) on La Palma achieved a sensitivity to fractional linear polarization (the ratio of linearly polarized flux to the total flux) of 10^{-6}. While PlanetPol did not succeed in detecting exoplanets, it did provide upper limits on the albedo's of a number of exoplanets (Lucas et al., 2009). The Extreme Polarimeter (ExPo), that was also mounted on the WHT, was designed to target young stars embedded in protoplanetary disks and evolved stars surrounded by dusty envelopes, with a polarimetric sensitivity better than 10^{-4} (Rodenhuis et al., 2012). The HIPPI-2 instrument uses repeated observations of bright stars in the SDSS g' band for achieving better than 3.5 ppm accuracy on the 3.9-m Anglo-Australian Telescope and better than 11 ppm on the 60-cm Western Sydney University's telescope (Bailey et al., 2020). The POLLUX-instrument on the LUVOIR space telescope concept aims at high-resolution (R~120,000) spectropolarimetric observations across ultra-violet and visible wavelengths (100-400 nm) to characterize atmospheres of terrestrial-type exoplanets (Team et al., 2019; Rossi et al., 2021). The EPICS instrument planned to be mounted on the ELT telescope, is designed to achieve a contrast of 10^{-10} depending the angular separation of the objects (Kasper et al., 2010).

In our simulations, we have neglected absorption by atmospheric gases. Including such absorption would yield lower total fluxes in specific spectral regions, depending on the type and amount of absorbing gas, its vertical distribution, and on the altitude and microphysical properties of the clouds and hazes. Including absorption by atmospheric gases could increase or decrease the degree of polarization, depending on the amount and vertical distribution of the absorbing gas and on the microphysical properties of the scattering particles at various altitudes (see e.g. Trees and Stam, 2022; Stam, 2008, for examples of polarization spectra of Earth-like planets). While measuring total and polarized fluxes of reflected starlight across gaseous absorption bands is of obvious interest for the characterization of planets and their atmospheres, the small numbers of photons inside gaseous absorption bands would make such observations extremely challenging.

We have also neglected any intrinsic polarization of Alpha Centauri A. Measurements of the degree of linear polarization of FKG stars indicate that active stars like Alpha Centauri A have a typical mean polarization of 28.5 ± 2.2 ppm (Cotton et al., 2017). This could add to the challenges in distinguishing the degree of polarization of the planet from that of the star if the planet is spatially unresolved, although the phase angle variation of the planetary signal and the direction of polarization of the planet signal (i.e.

usually either perpendicular or parallel to the plane through the star, the planet, and the observer) could be helpful provided of course that the instrument that is used for the observations has the capability to measure the extremely small variations in the signal as the planet orbits its star (on the order of 10^{-9}).

State-of-the-art instruments with sensitivity to polarization signals down to 10^{-6} (i.e. 1000 ppb) are still a few orders of magnitude away from detecting variations in polarization signals from spatially unresolved exo-Earths or exo-Venuses around nearby solar-type stars such as Alpha Centauri A. To be able to distinguish between the different planetary evolutionary phases explored in this paper, e.g. between water clouds or sulphuric acid clouds, variations on the order of 10^{-9} and hence significant improvements in sensitivity would be needed if the planets are spatially unresolved. The variation in the degree of polarization of spatially resolved planets along their orbital phase should be detectable by instruments capable of achieving star-planet contrasts of 10^{-9} and that would allow to distinguish between water clouds or sulphuric acid clouds. Current high-contrast imaging instruments manage to directly image self-luminous objects such as young exoplanets and brown dwarfs in NIR total fluxes at contrasts of 10^{-2}-10^{-6} (Bowler, 2016; Nielsen et al., 2019; Langlois et al., 2021; van Holstein, 2021). Further, instruments such as EPICS on ELT and concepts for instruments on future space observatories such as HabEx (Gaudi et al., 2020) and LUVOIR (Team et al., 2019) hold the promise for attaining contrasts of ~10^{-10}. Reaching such extreme contrasts would make it possible to directly detect terrestrial-type planets and to use polarimetry to differentiate between exo-Earths and exo-Venuses.

6

CONCLUDING REMARKS, RECOMMENDATIONS & OUTLOOK

In this chapter we provide concluding remarks on the work described in the previous chapters, give directions for future research, and reflect on its applicability for future missions.

6.1. POLARIMETRY FOR GRAVITY WAVE DETECTION

Understanding the atmospheric dynamics of Venus, including its super-rotation driven by solar-induced thermal tides (Horinouchi et al., 2020), requires studying the propagation and effects of gravity waves in the upper atmosphere of the planet. Waves, such as those observed by the Akatsuki spacecraft, drive variations in atmospheric density and aerosol distribution. Although direct and thermal imaging have primarily been used to detect gravity waves, those affecting higher altitudes, where changes in atmospheric density are minimal, remain challenging to observe. Such waves have typically been studied using in-situ sensors or night-glow measurements, but polarimetry presents a promising alternative for their detection due to its sensitivity to small density variations.

In Chapter 2, we used the Venus Mesoscale Model (VMM) (Lefèvre et al., 2020) to simulate the propagation of orographic gravity waves in the upper atmosphere of Venus. Using these simulations, we calculated the Stokes vectors F (total flux) and Q (linearly polarized flux) of sunlight that is reflected by Venus and determined the degree of polarization P as $-Q/F$. The simulations revealed that variations in gas optical thickness b_{m} above the cloud tops influence both F and Q. Although F is more sensitive to cloud properties, Q and P increase with increasing b_{m}, either due to the higher atmospheric gas density in exposed lower regions or with decreasing light wavelengths from visible towards UV.

Observations in nadir-viewing geometry and increasing solar zenith angles also add to Q and P. The signal change in P is most pronounced in the UV, with an expected magnitude of 500 ppm at 300 nm (for a solar zenith angle of 60°). This decreases to 50

ppm and 5 ppm at 600 nm and 900 nm, respectively, which require instruments with sensitivities of 10^{-4} or better for detection of such waves. The increase in polarization at shorter wavelengths aligns with expectations from Rayleigh scattering by CO_2 in the atmosphere. However, the Stokes parameters Q and P exhibit a non-monotonic dependence on b_m. Beyond a critical threshold, both parameters diminish due to enhanced multiple scattering effects within the atmospheric column.

Building on this, Chapter 3 focused on the concentric rings observed in polarized flux and the degree of polarization during ExPo observations of Venus. These observations were conducted under excellent atmospheric conditions using the William Herschel Telescope (WHT) at the Isaac Newton Group (ING) of telescopes, La Palma, Spain. Narrow-band filters centered on H-alpha (656.3 nm), H-alpha Continuum (647.1 nm), and Na (589.4 nm) revealed concentric rings covering the illuminated and visible part of Venus's disk, while broadband filters did not. The latter appeared to have coincided with deteriorating atmospheric seeing as Venus got closer to the horizon.

Our numerical simulations show that these concentric rings could be due to gravity waves inducing column gas density variations between 5–10% above the clouds. Such density changes did not significantly affect F but caused the detectable variations in P, with signals ranging between 10^{-3} and 10^{-4}. Supporting evidence for planet-wide atmospheric waves comes from Pioneer Venus ONMS measurements, which detected density fluctuations at altitudes of 160–200 km over 600 orbits, with activity concentrated near the terminators (Kasprzak et al., 1988; Mayr et al., 1988). Similarly, the Venus Express Atmospheric Drag Experiment (VEx ADE) detected thermospheric density fluctuations late in the mission (Müller-Wodarg et al., 2016; Rosenblatt et al., 2012).

Despite the promising results, the observation of gravity waves through polarimetry remains largely unvalidated. Previous missions like Venus Express and Akatsuki lacked dedicated polarization instruments, and while the Pioneer Venus Orbiter Cloud Photo Polarimeter (OCPP) did carry a polarimeter, its sensitivity was insufficient for detecting such waves. Modern instruments, such as the experimental ExPo polarimeter (Rodenhuis et al., 2012), have demonstrated the required sensitivity (10^{-4} or better) for detecting these phenomena. However, ExPo was an experimental setup, and no follow-up observations have been conducted.

ESA's upcoming EnVision mission to Venus, equipped with the polarization-sensitive VenSpec-H instrument, offers promising potential for detecting these waves (Neefs et al., 2024). However, the instrument lacks polarization measurement capability in the UV and visible wavelengths, where our numerical simulations indicate the signal strength is most pronounced. Ground-based observations under excellent seeing conditions (<0.5") or space-based missions with dedicated polarimetric instruments in UV and visible and targeting phase angles of 90° are crucial for advancing our understanding of Venusian atmospheric dynamics.

6.2. AEROSOL RETRIEVAL FROM GASEOUS ABSORPTION BANDS

Chapter 4 shows a sensitivity analysis to access whether the F and P across the strong CO_2 absorption bands in reflected sunlight spectra of Venus, between 1.4 and 1.5 μm, is sensitive to properties of the cloud and haze particles in the atmosphere of Venus. Rossi et al. (2015) successfully derived the cloud microphysical properties and analyzed

the variation in haze optical thickness across the planet by utilizing F and P data from Venus Express' SPICAV instrument in the continuum bands.

The investigation in this thesis was undertaken to determine whether the available polarimetry data in CO_2 absorption bands could be exploited to derive independent insights into the aerosol properties of Venus. Since radiative transfer computations that are based on line-by-line computations of a gaseous absorption spectrum are very time consuming, especially when polarisation is taken into account, we made use of the approximate but fast correlated k-distribution method (the ck-method) (Stam et al., 2000; Tsang et al., 2008).

We compared F and P across the absorption bands and the continuum, and our sensitivity analysis with a 1 nm box instrument response function indicates that changes in cloud tops result in detectable changes in both F and P across the absorption bands. Changes in haze optical thickness result in significant changes in P while they leave not significant enough changes in F. Retrieving cloud scale height using either F or P will be challenging as there is no significant change with cloud scale height variation.

Although SPICAV-IR on ESA's Venus Express mission had not been calibrated for polarimetry (as it was not meant to do any polarimetry), P as measured by the SPICAV-IR instrument agrees with P as computed with our code, where $|P|$ increases with increasing absorption line strength, with its sign depending on the aerosol properties and the observational geometry. We successfully retrieved a planet-wide haze optical thickness profile (Fig. 4.11) that aligns well with previous studies using the SPICAV-IR data and that supports our hypothesis that absorption bands offer unique and valuable insights into Venus' cloud and haze properties.

Our study used a small number of wavelengths across the CO_2 absorption band, based on varying absorption strengths to understand the variability in the signal and also to retrieve the haze properties from SPICAV-IR data. Future work could enhance retrievals by using more detailed aerosol models and specific wavelength ranges to assess cloud and haze properties across both continuum and absorption features. In addition: the haze layer above the Venusian clouds exhibits significant temporal variability (Braak et al., 2002) that has not been taken into account in our retrievals. It would be interesting to investigate the influence of such variability on the measured signals.

Our forward modeling indicates that a spectrally narrow instrument response function, ideally 1 nm or less, is essential for independently retrieving cloud or haze macrophysical properties within this absorption band. A broader response function leads to an effective loss of information regarding these aerosols. Additionally, it is crucial to design a spectropolarimeter with a minimal signal-to-noise ratio to effectively utilize the signal in high absorption bands.

We found that the errors in P because of the approximations in the ck-method depend on both the region of the absorption band and the observational geometry. Specifically, large observation angles (~60°) are unsuitable for this method due to errors exceeding 3.5% in P within the strongest absorption regions of these bands. Additionally, our numerical model assumes fixed cloud and haze microphysical properties, even though variability in particle sizes and spatial distributions is expected (Titov et al., 2018). This variability would further contribute to uncertainties in retrievals which should be studied in further detail.

The VenSpec-H spectrometer aboard ESA's EnVision mission is expected to measure polarization using two polarization-enabled filters in the bands 2a (2.34–2.42 μm), 2b (2.45–2.48 μm), and 4 (1.37–1.39 μm) (Neefs et al., 2024). Polarization measurements at these wavelengths will facilitate characterization of H_2O, HDO, SO_2, HF, and OCS content within Venus's cloud and haze layers, that are key constituents for understanding the sulphur based chemistry on Venus. A better understanding of the distribution of these gases helps answering questions that are related to Venus's geological history. While these species were not examined in this thesis, the requirements for a narrow instrument response and high signal-to-noise ratio identified here remain critically applicable.

6.3. POLARIMETRY OF STARLIGHT REFLECTED BY EXOPLANETS

With upcoming advanced telescopes, observing terrestrial planets around other stars will become possible. Venus, similar in size and mass to Earth and cloaked in dense clouds, might appear to have an Earth-like atmosphere and surface when viewed as a single point of light. However, it has a harsh, uninhabitable environment with a surface temperature of around 737 K. It is highly likely that we find many exo-Venuses in the search for exo-Earths (Lincowski et al., 2018).

Given the potential of polarimetry to distinguish atmospheric and cloud properties, Chapter 5 explores the signals in F and P that could help differentiate an exo-Venus from an exo-Earth. Furthermore, based on the hypothesis that Venus may have been present day Earth-like a few billion years ago, we also examined two intermediate evolutionary scenarios with thin and thick cloud cover (Bullock and Grinspoon, 2001). We assumed that the planet is situated in a stable orbit around Alpha Centauri A, with a mutual inclination angle of 35° allowing an Earth-based observer to access planetary phase angles α between 60° and 120°. In this study, we considered a wide wavelength range from 0.3 to 2.5 μm.

Our analysis indicates that observing F alone would be insufficient to distinguish between Earth-like and Venus-like exoplanets. In contrast, P provides significant variability with cloud microphysical properties, wavelength and phase angle α, making it a more effective diagnostic variable. Earth-like, liquid water clouds, characterized by spherical cloud droplets with large sizes, exhibit strong positive polarization close to the rainbow angle ($\alpha \approx 40°$) and close to 90° due to Rayleigh scattering. Venus-like clouds, that are composed of smaller sulfuric acid solution droplets, predominantly produce negative polarization at visible and infrared wavelengths. If the cloud particles on a Venus-like planet would have small sizes, comparable to the upper atmospheric haze on present-day Venus, they would be efficient Rayleigh scatterers at wavelengths greater than 1 μm, resulting in strong positive polarization at phase angles near 90°.

In particular, planets in orbits that are observed as edge-on, offer the almost full range of phase angles, which would facilitate a detailed study of the variation in P. This would enable precise characterization of their cloud properties, similar to the successful analysis of Venus's clouds by Hansen and Hovenier (1974), especially when the observations are performed across a wide wavelength range.

Detecting polarization signals of exoplanets, however, poses significant challenges. When the planetary signal is observed upon a background of (unpolarized) starlight, P typically ranges from 10^{-11} to 10^{-9}, necessitating the use of highly sensitive instruments

capable of achieving star-planet contrasts of 10^{-9} or better.

In our Earth-like planetary model, we have only investigated a specific case of an Earth that is fully covered with homogeneous clouds that consist of large water droplets while on the real Earth, clouds are patchy, have various thicknesses and have formed at various altitudes. In addition, clouds can contain solid, crystalline cloud particles. Such variations will impact a planet's polarization signals (Rossi and Stam, 2017).

Our numerical models also neglect the presence of oceans that can produce glints, when the starlight is reflected by the ocean surface. Glints can strongly polarize the reflected light as shown by Trees and Stam (2022). The angle at which P switches sign, also known as the inversion angle could provide important markers to indicate the type of underlying atmosphere and clouds (Bagnulo et al., 2024, and references therein). And of course, using evolutionary and climate models, different scenarios for the development of the surface and atmospheres of planets like the Earth, and the traces that would be left in the flux and polarization of the reflected starlight could be investigated.

Instruments such as POLLUX (Bouret et al., 2018), a proposed instrument for the LUVOIR Space Telescope, and EPICS (Kasper et al., 2010), designed for the Extremely Large Telescope (ELT) along with the HWO (Habitable Worlds Observer, Vaughan et al. (2023)) hold the promise of achieving the desired high contrasts ($>10^{-9}$). Together, these instruments are expected to deepen our understanding of exoplanet atmospheres, compositions, and evolutionary processes, paving the way for identifying Earth-like worlds and their potential habitability within the coming few decades.

ACKNOWLEDGEMENTS

This very long journey, more like an ultramarathon, filled with lessons, triumphs, and setbacks, would have been impossible to complete without the support of many wonderful people. I feel deeply fortunate to be surrounded by positive and encouraging individuals who gave me the strength and motivation to keep going, especially during times when the end was nowhere in sight.

I would like to thank Daphne for believing in me and making it possible for me to embark on this journey. Her inspiring lectures opened my eyes to the wonders of planetary science and convinced me to pursue this path during my master's, eventually leading to my PhD on Venus under her supervision. Through her quiet encouragement, we were able to explore bold ideas and establish collaborations with research institutions across the world. These experiences brought valuable insights and growth. I will always be grateful for her unwavering dedication to this work and for her continued support in helping me complete my PhD, even as I took a long detour and she faced challenging circumstances during the course of our work together. I hope to carry forward her courage, commitment, and deep passion for the subject as guiding principles in the years to come.

I was also fortunate to have Loïc as both a mentor and a friend throughout this journey. His expertise on Venus and polarimetry was essential to the progress of this research. His timely and detailed feedback at critical stages helped steer the work in the right direction and reduce delays. Beyond the science, his guidance on writing better and more efficient code in Python saved countless hours and made a significant impact on the overall productivity of this thesis.

I am thankful to my promotor, Bert Vermeersen, for enabling this PhD and for helping me navigate various complex administrative matters. His prompt feedback and steady support were instrumental in keeping this work on track. His encouragement throughout this process played a key role in bringing it to completion.

Throughout this PhD, I had the opportunity to collaborate with many excellent scientists, resulting in valuable insights and fruitful projects. I am especially grateful to Michiel Rodenhuis for allowing me to work with his Venus observations taken using ExPo and for the many hours spent together analyzing the waves data. I would also like to thank Maxence Lefèvre for his quick and generous collaboration on our investigation into gravity waves through polarimetry, which led to a rewarding publication. I am deeply thankful to Bhavesh Jaiswal for including me in the exciting effort to develop polarimetric capabilities at ISRO. I would like to express my sincerest appreciation to all the collaborators and PhD committee members who contributed to this journey and whose involvement has enriched this work: Aymeric Spiga, Frans Snik, Christoph Keller, Fouad Abiad, Emmanuel Marcq, F. Vanhellemont, S.J. Paardekooper, A.P. Siebesma, T. Horiouchi, T. Imamura, and J. Snively.

A significant part of my PhD journey was spent on the ninth floor of the faculty building. The quiet absence during the COVID period made me realise just how important it is to be surrounded by inspiring and supportive colleagues. My time on that floor was filled with engaging conversations that brought both insight and joy, within the workplace and beyond. Some of the memories I will always hold dear include organising coffee and cake moments with Yuxin, thought-provoking and wide-ranging discussions with Kartik, Mao's passion for beer and politics, practising Dutch with Bas, and gezellig lunch breaks shared with Teresa, Jesse, and Marc. I am especially grateful to Jesse for being a true friend during the difficult COVID period and beyond, where we exchanged thoughts on research, fitness, and life itself. The warm and motivating spirit of our floor would not have been the same without Relly (we miss you), Vidhya, Svenja, Jacco, Gunther, Tim, Bart, Hermes, Wouter, Jeannette, Jose, Dominic, Marc, Kevin, Stéphanie, Erwin, Ron, Ejo, Bernhard and Pieter. Each one of them played a part in shaping this thesis by enriching my experience during these important years as a PhD candidate.

When you are far from home, friends become your family. I was lucky to find friendships along the way that I will carry with me for life. Yask and Mihir were the perfect companions on this journey, from our spontaneous IKEA breakfasts to long bike rides along the canals of Delft, as we tried to make sense of life in a new country. The countless hours of laughter and conversation with miyagos made even the hardest days feel lighter and more like home. I am deeply grateful to Krithika for her wisdom and fun but calm presence, and to Ivana for her warm friendship and inspiring musical talent, which I truly admire and strive to learn from. I am also thankful to Kim for being the perfect "bro", someone with whom I could share my love for self defense, spirituality, and health, always with a sense of fun and ease. Joreen played an important role in shaping this work through her steady support, especially during the difficult days of the COVID period. Her thoughtful conversations and generous feedback on my manuscript helped improve this thesis in ways I will always appreciate. In recent years, I have also been fortunate to share many joyful moments with Bea, Luca, Kate, Valerio, Lotte, Mat, Keven, Lars, Shrey and Sumit whose friendship has added to the beauty of my life in the Netherlands.

Last but not least, family plays the most influential role in shaping a child's worldview. I have been fortunate to have parents whose love, patience, and steady encouragement gave me the strength to walk this path, even when it meant being far from them for nearly a decade. My sister, with her warmth, wisdom, and quiet support from afar, has been a constant source of strength throughout this journey. Their unwavering belief in me and gentle push forward provided the foundation and motivation I needed to keep going.

Like in a marathon, the final stretch is often the hardest. Having someone by your side to cheer you on can make all the difference. I am deeply grateful to life and its quiet magic for bringing Tejaswini into my world. Her grounded presence, boundless love, and steadfast encouragement gave me the final momentum to see this work through. None of it would have been possible without her.

BIBLIOGRAPHY

M. Alexander. A mechanism for the venus thermospheric superrotation. *Geophysical research letters*, 19(22):2207–2210, 1992.

M. Alexander, A. Stewart, S. Solomon, and S. Boucher. Local time asymmetries in the venus thermosphere. *Journal of Geophysical Research: Planets*, 98(E6):10849–10871, 1993.

S. Bagnulo, I. Belskaya, A. Cellino, Y. G. Kwon, O. Muñoz, and D. M. Stam. Polarimetry of solar system minor bodies and planets. *The Astronomy and Astrophysics Review*, 32 (1):1–103, 2024.

J. Bailey. Rainbows, Polarization, and the Search for Habitable Planets. *Astrobiology*, 7: 320–332, May 2007. doi: 10.1089/ast.2006.0039.

J. Bailey, L. Kedziora-Chudczer, and K. Bott. Polarized radiative transfer in planetary atmospheres and the polarization of exoplanets. *Monthly Notices of the Royal Astronomical Society*, 480(2):1613–1625, 2018.

J. Bailey, D. V. Cotton, L. Kedziora-Chudczer, A. De Horta, and D. Maybour. Hippi-2: a versatile high-precision polarimeter. *Publications of the Astronomical Society of Australia*, 37, 2020.

J. Barstow, C. Tsang, C. Wilson, P. Irwin, F. Taylor, K. McGouldrick, P. Drossart, G. Piccioni, and S. Tellmann. Models of the global cloud structure on venus derived from venus express observations. *Icarus*, 217(2):542–560, 2012.

M. J. Belton, G. R. Smith, G. Schubert, and A. D. Del Genio. Cloud patterns, waves and convection in the venus atmosphere. *Journal of the Atmospheric Sciences*, 33(8):1394–1417, 1976.

D. A. Belyaev, F. Montmessin, J.-L. Bertaux, A. Mahieux, A. A. Fedorova, O. I. Korablev, E. Marcq, Y. L. Yung, and X. Zhang. Vertical profiling of so2 and so above venus' clouds by spicav/soir solar occultations. *Icarus*, 217(2):740–751, 2012.

J.-L. Bertaux, D. Nevejans, O. Korablev, E. Villard, E. Quémerais, E. Neefs, F. Montmessin, F. Leblanc, J.-P. Dubois, E. Dimarellis, et al. Spicav on venus express: Three spectrometers to study the global structure and composition of the venus atmosphere. *Planetary and Space Science*, 55(12):1673–1700, 2007.

A. Bideau-Mehu, Y. Guern, R. Abjean, and A. Johannin-Gilles. Interferometric determination of the refractive index of carbon dioxide in the ultraviolet region. *Optics Communications*, 9(4):432–434, 1973.

E. Bjonnes, B. Johnson, and A. Evans. Estimating venusian thermal conditions using multiring basin morphology. *Nature Astronomy*, 5(5):498–502, 2021.

E. Boesche, P. Stammes, and R. Bennartz. Aerosol influence on polarization and intensity in near-infrared o2 and co2 absorption bands observed from space. *Journal of Quantitative Spectroscopy and Radiative Transfer*, 110(3):223–239, 2009.

S. Bougher, M. Alexander, and H. Mayr. Upper atmosphere dynamics: global circulation and gravity waves. *Venus II: Geology, Geophysics, Atmosphere, and Solar Wind Environment*, pages 259–291, 1997.

S. Bougher, S. Rafkin, and P. Drossart. Dynamics of the venus upper atmosphere: Outstanding problems and new constraints expected from venus express. *Planetary and Space Science*, 54(13):1371–1380, 2006.

J.-C. Bouret, C. Neiner, A. I. G. de Castro, C. Evans, B. Gaensicke, S. Shore, L. Fossati, C. Gry, S. Charlot, F. Marin, et al. The science case for pollux: a high-resolution uv spectropolarimeter onboard luvoir. In *Space Telescopes and Instrumentation 2018: Ultraviolet to Gamma Ray*, volume 10699, pages 851–861. SPIE, 2018.

B. P. Bowler. Imaging extrasolar giant planets. *Publications of the Astronomical Society of the Pacific*, 128(968):102001, 2016.

C. Braak, J. De Haan, J. Hovenier, and L. Travis. Spatial and temporal variations of venus haze properties obtained from pioneer venus orbiter polarimetry. *Journal of Geophysical Research: Planets*, 107(E5):5–1, 2002.

M. A. Bullock and D. H. Grinspoon. The stability of climate on venus. *Journal of Geophysical Research: Planets*, 101(E3):7521–7529, 1996.

M. A. Bullock and D. H. Grinspoon. The recent evolution of climate on venus. *Icarus*, 150 (1):19–37, 2001.

E. Burgess and P. Gangooly. *Sûrya-Siddhânta: A Text-book of Hindu Astronomy*. Motilal Banarsidass Publ., 1989.

D. F. Buscher. Simulating large atmospheric phase screens using a woofer-tweeter algorithm. *Optics express*, 24(20):23566–23571, 2016.

P. K. Byrne and S. Krishnamoorthy. Estimates on the frequency of volcanic eruptions on venus. *Journal of Geophysical Research: Planets*, 127(1):e2021JE007040, 2022.

H. Canovas, M. Rodenhuis, S. Jeffers, M. Min, and C. Keller. Data-reduction techniques for high-contrast imaging polarimetry-applications to expo. *Astronomy & Astrophysics*, 531:A102, 2011.

M. Y. Chou, C. C. Lin, J. Yue, H. F. Tsai, Y. Y. Sun, J. Y. Liu, and C. H. Chen. Concentric traveling ionosphere disturbances triggered by super typhoon meranti (2016). *Geophysical Research Letters*, 44(3):1219–1226, 2017.

D. Coffeen and T. Gehrels. Wavelength dependence of polarization. xv. observations of venus. *The Astronomical Journal*, 74:433, 1969.

D. V. Cotton, J. P. Marshall, J. Bailey, L. Kedziora-Chudczer, K. Bott, S. C. Marsden, and B. D. Carter. The intrinsic and interstellar broad-band linear polarization of nearby fgk dwarfs. *Monthly Notices of the Royal Astronomical Society*, 467(1):873–897, 2017.

C. Counselman, S. Gourevitch, R. King, G. Loriot, and E. Ginsberg. Zonal and meridional circulation of the lower atmosphere of venus determined by radio interferometry. *Journal of Geophysical Research: Space Physics*, 85(A13):8026–8030, 1980.

D. CRISP, C. EDWARDS, R. KAHN, D. McCLEESE, and D. RIDER. Atmosphere: An assessment. *Venus II–geology, Geophysics, Atmosphere, and Solar Wind Environment*, 1:459, 1997.

J. F. de Haan, P. Bosma, and J. Hovenier. The adding method for multiple scattering calculations of polarized light. *Astronomy and Astrophysics*, 183:371–391, 1987.

J. F. de Haan, P. B. Bosma, and J. W. Hovenier. The adding method for multiple scattering calculations of polarized light. A&A, 183:371–391, Sept. 1987.

W. De Rooij and C. Van der Stap. Expansion of mie scattering matrices in generalized spherical functions. *Astronomy and Astrophysics*, 131:237–248, 1984.

W. A. de Rooij and C. C. A. H. van der Stap. Expansion of Mie scattering matrices in generalized spherical functions. A&A, 131:237–248, Feb. 1984.

A. D. Del Genio and W. B. Rossow. Temporal variability of ultraviolet cloud features in the venus stratosphere. *Icarus*, 51(2):391–415, 1982.

A. D. Del Genio and W. B. Rossow. Planetary-scale waves and the cyclic nature of cloud top dynamics on venus. *Journal of Atmospheric Sciences*, 47(3):293–318, 1990.

A. Dollfus and D. Coffeen. Polarization of venus i disk observations. *Astronomy and Astrophysics*, 8:251, 1970.

T. Donahue, J. Hoffman, R. Hodges, and A. Watson. Venus was wet: A measurement of the ratio of deuterium to hydrogen. *Science*, 216(4546):630–633, 1982.

P. Drossart, G. Piccioni, A. Adriani, F. Angrilli, G. Arnold, K. Baines, G. Bellucci, J. Benkhoff, B. Bézard, J.-P. Bibring, et al. Scientific goals for the observation of venus by virtis on esa/venus express mission. *Planetary and Space Science*, 55(12):1653–1672, 2007.

L. Esposito, R. Knollenberg, M. Marov, O. Toon, and R. Turco. 16. the clouds and hazes of venus. *Venus*, 484, 1983.

L. W. Esposito. Sulfur dioxide: Episodic injection shows evidence for active venus volcanism. *Science*, 223(4640):1072–1074, 1984.

A. Fedorova, E. Marcq, M. Luginin, O. Korablev, J.-L. Bertaux, and F. Montmessin. Variations of water vapor and cloud top altitude in the venus' mesosphere from spicav/vex observations. *Icarus*, 275:143–162, 2016.

F. Forbes and A. Fymat. Astronomical fourier spectropolarimetry. 1974.

D. C. Fritts and M. J. Alexander. Gravity wave dynamics and effects in the middle atmosphere. *Reviews of geophysics*, 41(1), 2003.

Q. Fu and K. Liou. On the correlated k-distribution method for radiative transfer in nonhomogeneous atmospheres. *Journal of the Atmospheric Sciences*, 49(22):2139–2156, 1992.

T. Fukuhara, M. Futaguchi, G. L. Hashimoto, T. Horinouchi, T. Imamura, N. Iwagaimi, T. Kouyama, S.-y. Murakami, M. Nakamura, K. Ogohara, et al. Large stationary gravity wave in the atmosphere of venus. *Nature Geoscience*, 10(2):85–88, 2017.

I. Garate-Lopez and S. Lebonnois. Latitudinal variation of clouds' structure responsible for Venus' cold collar. *Icarus*, 314:1–11, 2018. doi: 10.1016/j.icarus.2018.05.011.

A. García Muñoz, S. Pérez-Hoyos, and A. Sánchez-Lavega. Glory revealed in disk-integrated photometry of Venus. A&A, 566:L1, June 2014. doi: 10.1051/0004-6361/201423531.

A. García-Muñoz, S. Pérez-Hoyos, and A. Sánchez-Lavega. Glory revealed in disk-integrated photometry of venus. *Astronomy & Astrophysics*, 566:L1, 2014.

J. B. Garvin, S. A. Getty, G. N. Arney, N. M. Johnson, E. Kohler, K. O. Schwer, M. Sekerak, A. Bartels, R. S. Saylor, V. E. Elliott, et al. Revealing the mysteries of venus: The davinci mission. *The Planetary Science Journal*, 3(5):117, 2022.

B. S. Gaudi, S. Seager, B. Mennesson, A. Kiessling, K. Warfield, K. Cahoy, J. T. Clarke, S. Domagal-Goldman, L. Feinberg, O. Guyon, et al. The habitable exoplanet observatory (habex) mission concept study final report. *arXiv preprint arXiv:2001.06683*, 2020.

R. Ghail, C. Wilson, T. Widemann, L. Bruzzone, C. Dumoulin, J. Helbert, R. Herrick, E. Marcq, P. Mason, P. Rosenblatt, et al. Envision: understanding why our most earth-like neighbour is so different. *arXiv preprint arXiv:1703.09010*, 2017.

J. J. Goldstein, M. J. Mumma, T. Kostiuk, D. Deming, F. Espenak, and D. Zipoy. Absolute wind velocities in the lower thermosphere of venus using infrared heterodyne spectroscopy. *Icarus*, 94(1):45–63, 1991.

J. Gong, J. Yue, and D. L. Wu. Global survey of concentric gravity waves in airs images and ecmwf analysis. *Journal of Geophysical Research: Atmospheres*, 120(6):2210–2228, 2015.

I. E. Gordon, L. S. Rothman, C. Hill, R. V. Kochanov, Y. Tan, P. F. Bernath, M. Birk, V. Boudon, A. Campargue, K. Chance, et al. The hitran2016 molecular spectroscopic database. *Journal of Quantitative Spectroscopy and Radiative Transfer*, 203:3–69, 2017.

G. M. Hale and M. R. Querry. Optical constants of water in the 200-nm to 200-μm wavelength region. *Applied optics*, 12(3):555–563, 1973.

J. Hansen and J. Hovenier. The doubling method applied to multiple scattering of polarized light. *Journal of Quantitative Spectroscopy and Radiative Transfer*, 11(6):809–812, 1971.

J. E. Hansen and J. Hovenier. Interpretation of the polarization of venus. *Journal of the Atmospheric Sciences*, 31(4):1137–1160, 1974.

J. E. Hansen and J. W. Hovenier. Interpretation of the polarization of Venus. *Journal of Atmospheric Sciences*, 31:1137–1160, May 1974. doi: 10.1175/1520-0469(1974)031<1137:IOTPOV>2.0.CO;2.

J. E. Hansen and L. D. Travis. Light scattering in planetary atmospheres. *Space Science Reviews*, 16:527–610, 1974.

J. E. Hansen and L. D. Travis. Light scattering in planetary atmospheres. *Space science reviews*, 16(4):527–610, 1974.

R. Haus, D. Kappel, and G. Arnold. Atmospheric thermal structure and cloud features in the southern hemisphere of Venus as retrieved from VIRTIS/VEX radiation measurements. *Icarus*, 232:232–248, 2014. doi: 10.1016/j.Icarus.2014.01.020.

R. Haus, D. Kappel, and G. Arnold. Radiative heating and cooling in the middle and lower atmosphere of Venus and responses to atmospheric and spectroscopic parameter variations. *Planetary and Space Science*, 117:262–294, 2015. doi: 10.1016/j.pss.2015.06.024.

J. Helbert, A. C. Vandaele, E. Marcq, S. Robert, C. Ryan, G. Guignan, Y. Rosas-Ortiz, E. Neefs, I. R. Thomas, G. Arnold, et al. The venspec suite on the esa envision mission to venus. In *Infrared remote sensing and instrumentation XXVII*, volume 11128, pages 18–32. SPIE, 2019.

J. Helbert, M. Pertenaïs, I. Walter, G. Peter, T. Säuberlich, A. Cacovean, A. Maturilli, G. Alemanno, B. Zender, C. A. Carrasco, et al. The venus emissivity mapper: implementation for flight on the nasa veritas mission. In *Infrared Remote Sensing and Instrumentation XXX*, volume 12233, pages 13–23. SPIE, 2022.

S. Hensley, B. Campbell, D. Perkovic-Martin, K. Wheeler, W. Kiefer, and R. Ghail. Visar and vensar: Two proposed radar investigations of venus. In *2020 IEEE Radar Conference (RadarConf20)*, pages 1–6. IEEE, 2020.

R. R. Herrick and S. Hensley. Surface changes observed on a venusian volcano during the magellan mission. *Science*, 379(6638):1205–1208, 2023.

D. P. Hinson and J. M. Jenkins. Magellan radio occultation measurements of atmospheric waves on venus. *Icarus*, 114(2):310–327, 1995.

T. Horinouchi, T. Kouyama, Y. J. Lee, S.-y. Murakami, K. Ogohara, M. Takagi, T. Imamura, K. Nakajima, J. Peralta, A. Yamazaki, et al. Mean winds at the cloud top of venus obtained from two-wavelength uv imaging by akatsuki. *Earth, Planets and Space*, 70(1): 1–19, 2018.

T. Horinouchi, Y.-Y. Hayashi, S. Watanabe, M. Yamada, A. Yamazaki, T. Kouyama, M. Taguchi, T. Fukuhara, M. Takagi, K. Ogohara, et al. How waves and turbulence maintain the super-rotation of venus' atmosphere. *Science*, 368(6489):405–409, 2020.

A. Y. Hou and B. F. Farrell. Superrotation induced by critical-level absorption of gravity waves on Venus - an assessment. *J. of Atm. Sc.*, 44:1049–1061, 1987. doi: 10.1175/1520-0469(1987)044<1049:SIBCLA>2.0.CO;2.

R. Hueso, J. Peralta, I. Garate-Lopez, T. Bandos, and A. Sánchez-Lavega. Six years of venus winds at the upper cloud level from uv, visible and near infrared observations from virtis on venus express. *Planetary and Space Science*, 113:78–99, 2015.

D. M. Hunten, L. Colin, T. M. Donahue, and V. I. Moroz. *Venus*. University of Arizona Press, 2022.

N. Ignatiev, D. Titov, G. Piccioni, P. Drossart, W. Markiewicz, V. Cottini, T. Roatsch, M. Almeida, and N. Manoel. Altimetry of the venus cloud tops from the venus express observations. *Journal of Geophysical Research: Planets*, 114(E9), 2009.

N. I. Ignatiev, D. V. Titov, G. Piccioni, P. Drossart, W. J. Markiewicz, V. Cottini, T. Roatsch, M. Almeida, and N. Manoel. Altimetry of the Venus cloud tops from the Venus Express observations. *Journal of Geophysical Research (Planets)*, 114:E00B43, Aug. 2009. doi: 10.1029/2008JE003320.

T. Imamura, T. Higuchi, Y. Maejima, M. Takagi, N. Sugimoto, K. Ikeda, and H. Ando. Inverse insolation dependence of Venus' cloud-level convection. *Icarus*, 228:181–188, 2014. doi: 10.1016/j.Icarus.2013.10.012.

P. Irwin, R. de Kok, A. Negrao, C. Tsang, C. Wilson, P. Drossart, G. Piccioni, D. Grassi, and F. Taylor. Spatial variability of carbon monoxide in venus' mesosphere from venus express/visible and infrared thermal imaging spectrometer measurements. *Journal of Geophysical Research: Planets*, 113(E5), 2008.

S. Jeffers, M. Min, L. Waters, H. Canovas, M. Rodenhuis, M. de Juan Ovelar, A. Chies-Santos, and C. Keller. Direct imaging of a massive dust cloud around r coronae borealis. *Astronomy & Astrophysics*, 539:A56, 2012.

J. M. Jenkins, P. G. Steffes, D. P. Hinson, J. D. Twicken, and G. L. Tyler. Radio occultation studies of the venus atmosphere with the magellan spacecraft: 2. results from the october 1991 experiments. *Icarus*, 110(1):79–94, 1994.

S. Jordan, P. B. Rimmer, O. Shorttle, and T. Constantinou. Photochemistry of venus-like planets orbiting k-and m-dwarf stars. *arXiv preprint arXiv:2108.05778*, 2021.

S. R. Kane, P. Vervoort, J. Horner, and F. J. Pozuelos. Could the migration of jupiter have accelerated the atmospheric evolution of venus? *The Planetary Science Journal*, 1(2): 42, 2020.

T. Karalidi, D. Stam, and J. Hovenier. Flux and polarisation spectra of water clouds on exoplanets. *Astronomy & Astrophysics*, 530:A69, 2011.

T. Karalidi, D. Stam, and J. Hovenier. Looking for the rainbow on exoplanets covered by liquid and icy water clouds. *Astronomy & Astrophysics*, 548:A90, 2012.

M. Kasper, J.-L. Beuzit, C. Verinaud, R. G. Gratton, F. Kerber, N. Yaitskova, A. Boccaletti, N. Thatte, H. M. Schmid, C. Keller, et al. Epics: direct imaging of exoplanets with the e-elt. In *Ground-based and Airborne Instrumentation for Astronomy III*, volume 7735, pages 948–956. SPIE, 2010.

W. Kasprzak, A. Hedin, H. Mayr, and H. Niemann. Wavelike perturbations observed in the neutral thermosphere of venus. *Journal of Geophysical Research: Space Physics*, 93 (A10):11237–11245, 1988.

J. F. Kasting. Runaway and moist greenhouse atmospheres and the evolution of earth and venus. *Icarus*, 74(3):472–494, 1988.

K. Kawabata, D. Coffeen, J. Hansen, W. Lane, M. Sato, and L. Travis. Cloud and haze properties from pioneer venus polarimetry. *Journal of Geophysical Research: Space Physics*, 85(A13):8129–8140, 1980.

Y. Kawata. Circular polarization of sunlight reflected by planetary atmospheres. *Icarus*, 33(1):217–232, 1978.

C. U. Keller, H. M. Schmid, L. B. Venema, H. Hanenburg, R. Jager, M. Kasper, P. Martinez, F. Rigal, M. Rodenhuis, R. Roelfsema, et al. Epol: the exoplanet polarimeter for epics at the e-elt. In *Ground-based and airborne instrumentation for astronomy III*, volume 7735, page 77356G. International Society for Optics and Photonics, 2010.

J. C. Kemp, R. D. Wolstencroft, and J. B. Swedlund. Circular polarization: Jupiter and other planets. *Nature*, 232(5307):165–168, 1971.

J. C. Kemp, G. Henson, C. Steiner, and E. Powell. The optical polarization of the sun measured at a sensitivity of parts in ten million. *Nature*, 326(6110):270, 1987.

J. C. Kemp, G. D. Henson, C. T. Steiner, and E. R. Powell. The optical polarization of the sun measured at a sensitivity of parts in ten million. *Nature*, 326:270–273, Mar. 1987.

I. Khatuntsev, M. Patsaeva, D. Titov, N. Ignatiev, A. Turin, S. Limaye, W. Markiewicz, M. Almeida, T. Roatsch, and R. Moissl. Cloud level winds from the venus express monitoring camera imaging. *Icarus*, 226(1):140–158, 2013.

T. Kitahara, T. Imamura, T. M. Sato, A. Yamazaki, Y. J. Lee, M. Yamada, S. Watanabe, M. Taguchi, T. Fukuhara, T. Kouyama, et al. Stationary features at the cloud top of venus observed by ultraviolet imager onboard akatsuki. *Journal of Geophysical Research: Planets*, 124(5):1266–1281, 2019.

A. J. Kliore, V. I. Moroz, and G. M. Keating. The Venus International Reference Atmosphere. *Advances in Space Research*, 5(11), Jan. 1985.

W. J. Knibbe, J. F. de Haan, J. W. Hovenier, and L. D. Travis. Spatial variations of venus' cloud properties derived from polarimetry. In *Atmospheric Sensing and Modelling*, volume 2311, pages 47–57. International Society for Optics and Photonics, 1995.

W. J. J. Knibbe, J. F. de Haan, J. W. Hovenier, and L. D. Travis. Analysis of temporal variations of the polarization of venus observed by pioneer venus orbiter. *Journal of Geophysical Research: Planets*, 103(E4):8557–8574, 1998.

R. Knollenberg and D. Hunten. The microphysics of the clouds of venus: Results of the pioneer venus particle size spectrometer experiment. *Journal of Geophysical Research: Space Physics*, 85(A13):8039–8058, 1980.

R. G. Knollenberg and D. Hunten. Clouds of venus: Particle size distribution measurements. *Science*, 203(4382):792–795, 1979.

O. Korablev, A. Fedorova, J.-L. Bertaux, A. Stepanov, A. Kiselev, Y. Kalinnikov, A. Titov, F. Montmessin, J. Dubois, E. Villard, V. Sarago, D. Belyaev, A. Reberac, and E. Neefs. SPICAV IR acousto-optic spectrometer experiment on Venus Express. *Planetary and Space Science*, 65:38–57, may 2012. doi: 10.1016/j.pss.2012.01.002.

O. Korablev, A. Fedorova, J.-L. Bertaux, A. Stepanov, A. Kiselev, Y. K. Kalinnikov, A. Y. Titov, F. Montmessin, J.-P. Dubois, E. Villard, et al. Spicav ir acousto-optic spectrometer experiment on venus express. *Planetary and Space Science*, 65(1):38–57, 2012.

M. Koukouli, P. Irwin, and F. Taylor. Water vapor abundance in venus' middle atmosphere from pioneer venus oir and venera 15 fts measurements. *Icarus*, 173(1):84–99, 2005.

T. Kouyama, T. Imamura, M. Nakamura, T. Satoh, and Y. Futaana. Long-term variation in the cloud-tracked zonal velocities at the cloud top of venus deduced from venus express vmc images. *Journal of Geophysical Research: Planets*, 118(1):37–46, 2013.

T. Kouyama, T. Imamura, M. Taguchi, T. Fukuhara, T. M. Sato, A. Yamazaki, M. Futaguchi, S. Murakami, G. L. Hashimoto, M. Ueno, N. Iwagami, S. Takagi, M. Takagi, K. Ogohara, H. Kashimura, T. Horinouchi, N. Sato, M. Yamada, Y. Yamamoto, S. Ohtsuki, K. Sugiyama, H. Ando, M. Takamura, T. Yamada, T. Satoh, and M. Nakamura. Topographical and Local Time Dependence of Large Stationary Gravity Waves Observed at the Cloud Top of Venus. *Geophysical Research Letters*, 44:12098–12105, 2017. doi: 10.1002/2017GL075792.

T. Kouyama, T. Imamura, M. Taguchi, T. Fukuhara, T. M. Sato, A. Yamazaki, M. Futaguchi, S.-y. Murakami, G. L. Hashimoto, M. Ueno, et al. Topographical and local time dependence of large stationary gravity waves observed at the cloud top of venus. *Geophysical Research Letters*, 44(24):12–098, 2017.

A. Lacis and V. Oinas. A description of the correlated k distribution method for modeling nongray gaseous absorption, thermal emission, and multiple scattering in vertically

inhomogeneous atmospheres. *Journal of Geophysical Research: Atmospheres*, 96(D5): 9027–9063, 1991.

M. Langlois, R. Gratton, A.-M. Lagrange, P. Delorme, A. Boccaletti, M. Bonnefoy, A.-L. Maire, D. Mesa, G. Chauvin, S. Desidera, et al. The sphere infrared survey for exoplanets (shine)-ii. observations, data reduction and analysis, detection performances, and initial results. *Astronomy & Astrophysics*, 651:A71, 2021.

P. Laven. How are glories formed? *Appl. Opt.*, 44(27):5675–5683, Sep 2005. doi: 10.1364/AO.44.005675.

P. Laven. Effects of refractive index on glories. *Applied optics*, 47(34):H133–H142, 2008.

S. Lebonnois, V. Eymet, C. Lee, and J. Vatant d'Ollone. Analysis of the radiative budget of the Venusian atmosphere based on infrared Net Exchange Rate formalism. *J. of Geophys. Res. (Planets)*, 120:1186–1200, 2015. doi: 10.1002/2015JE004794.

Y. Lee, A. Yamazaki, T. Imamura, M. Yamada, S. Watanabe, T. Sato, K. Ogohara, G. Hashimoto, and S. Murakami. Scattering properties of the venusian clouds observed by the uv imager on board akatsuki. *The Astronomical Journal*, 154(2):44, 2017.

M. Lefèvre, A. Spiga, and S. Lebonnois. Three-dimensional turbulence-resolving modeling of the Venusian cloud layer and induced gravity waves. *Journal of Geophysical Research (Planets)*, 122:134–149, 2017. doi: 10.1002/2016JE005146.

M. Lefèvre, S. Lebonnois, and A. Spiga. Three-Dimensional Turbulence-Resolving Modeling of the Venusian Cloud Layer and Induced Gravity Waves: Inclusion of Complete Radiative Transfer and Wind Shear. *Journal of Geophysical Research (Planets)*, 123: 2773–2789, 2018. doi: 10.1029/2018JE005679.

M. Lefèvre, A. Spiga, and S. Lebonnois. Mesoscale modeling of venus' bow-shape waves. *Icarus*, 335:113376, 2020.

S. Limaye, R. Clancy, M. Rengel, and M. Sorning. Towards a better understanding of the venus atmosphere-observations needed between 65-120 km. In *AGU Fall Meeting Abstracts*, volume 2013, pages P41D–1950, 2013.

S. S. Limaye. Venus atmospheric circulation: Observations and implications of the thermal structure. *Advances in Space Research*, 5(9):51–62, 1985.

S. S. Limaye. Venus: Cloud level circulation during 1982 as determined from pioneer cloud photopolarimeter images: Ii. solar longitude dependent circulation. *Icarus*, 73 (2):212–226, 1988.

S. S. Limaye and V. E. Suomi. Cloud motions on venus: Global structure and organization. *Journal of the Atmospheric Sciences*, 38(6):1220–1235, 1981.

A. P. Lincowski, V. S. Meadows, D. Crisp, T. D. Robinson, R. Luger, J. Lustig-Yaeger, and G. N. Arney. Evolved climates and observational discriminants for the trappist-1 planetary system. *The Astrophysical Journal*, 867(1):76, 2018.

P. W. Lucas, J. H. Hough, J. A. Bailey, M. Tamura, E. Hirst, and D. Harrison. Planetpol polarimetry of the exoplanet systems 55 Cnc and T Boo*. *Monthly Notices of the Royal Astronomical Society*, 393(1):229–244, 01 2009. ISSN 0035-8711. doi: 10.1111/j.1365-2966.2008.14182.x. URL https://doi.org/10.1111/j.1365-2966.2008.14182.x.

M. Luginin, A. Fedorova, D. Belyaev, F. Montmessin, V. Wilquet, O. Korablev, J.-L. Bertaux, and A. Vandaele. Aerosol properties in the upper haze of venus from spicav ir data. *Icarus*, 277:154–170, 2016.

J. Lustig-Yaeger, V. S. Meadows, and A. P. Lincowski. The detectability and characterization of the trappist-1 exoplanet atmospheres with jwst. *The Astronomical Journal*, 158 (1):27, 2019a.

J. Lustig-Yaeger, V. S. Meadows, and A. P. Lincowski. A mirage of the cosmic shoreline: Venus-like clouds as a statistical false positive for exoplanet atmospheric erosion. *The Astrophysical Journal Letters*, 887(1):L11, 2019b.

B. Lustrement, S. Bertran, N. Rouanet, A. D. Damian, R. Hassen-Khodja, C. Montaron, S. Ruocco, A. Vontrat, F. Vivat, L. Baggio, et al. Design of the venspec-u instrument: a double uv imaging spectrometer to analyze sulfured gases in the venus' atmosphere. In *Infrared Remote Sensing and Instrumentation XXXII*, volume 13144, pages 164–196. SPIE, 2024.

B. Lyot. Recherches sur la polarisation de la lumière des planètes et de quelques substances terrestres; recherches sur la polarisation de la lumière des planètes et de quelques substances terrestres; research on polarization of light from planets and some terrestrial substances. *Ph. D. Thesis*, 1929.

G. Mahapatra, M. Lefèvre, L. Rossi, A. Spiga, and D. M. Stam. Polarimetry as a tool for observing orographic gravity waves on venus. *The Planetary Science Journal*, 2(3):96, 2021.

G. Mahapatra, F. Abiad, L. Rossi, and D. M. Stam. From exo-earths to exo-venuses: Flux and polarization signatures of reflected light. *Astronomy and Astrophysics-A&A*, 671: A165, 2023.

E. Marcq, D. Belyaev, F. Montmessin, A. Fedorova, J.-L. Bertaux, A. C. Vandaele, and E. Neefs. An investigation of the so2 content of the venusian mesosphere using spicav-uv in nadir mode. *Icarus*, 211(1):58–69, 2011.

E. Marcq, J.-L. Bertaux, F. Montmessin, and D. Belyaev. Variations of sulphur dioxide at the cloud top of venus's dynamic atmosphere. *Nature geoscience*, 6(1):25–28, 2013.

E. Marcq, F. P. Mills, C. D. Parkinson, and A. C. Vandaele. Composition and chemistry of the neutral atmosphere of venus. *Space Science Reviews*, 214:1–55, 2018.

W. Markiewicz, D. Titov, S. Limaye, H. U. Keller, N. Ignatiev, R. Jaumann, N. Thomas, H. Michalik, R. Moissl, and P. Russo. Morphology and dynamics of the upper cloud layer of venus. *Nature*, 450(7170):633–636, 2007.

W. J. Markiewicz, E. Petrova, O. Shalygina, M. Almeida, D. V. Titov, S. S. Limaye, N. Ignatiev, T. Roatsch, and K.-D. Matz. Glory on venus cloud tops and the unknown uv absorber. *Icarus*, 234:200–203, 2014.

W. J. Markiewicz, E. V. Petrova, and O. S. Shalygina. Aerosol properties in the upper clouds of venus from glory observations by the venus monitoring camera (venus express mission). *Icarus*, 299:272–293, 2018.

H. Mayr, I. Harris, W. Kasprzak, M. Dube, and F. Varosi. Gravity waves in the upper atmosphere of venus. *Journal of Geophysical Research: Space Physics*, 93(A10):11247–11262, 1988.

K. McGouldrick and O. B. Toon. Modeling the effects of shear on the evolution of the holes in the condensational clouds of venus. *Icarus*, 196(1):35–48, 2008.

A. Migliorini, F. Altieri, L. Zasova, G. Piccioni, G. Bellucci, A. C. Moinelo, P. Drossart, E. D'Aversa, F. Carrozzo, B. Gondet, et al. Oxygen airglow emission on venus and mars as seen by virtis/vex and omega/mex imaging spectrometers. *Planetary and Space Science*, 59(10):981–987, 2011.

M. Min, S. V. Jeffers, H. Canovas, M. Rodenhuis, C. Keller, and L. Waters. The color dependent morphology of the post-agb star hd 161796. *Astronomy & Astrophysics*, 554: A15, 2013.

R. Moissl, I. Khatuntsev, S. Limaye, D. Titov, W. Markiewicz, N. Ignatiev, T. Roatsch, K.-D. Matz, R. Jaumann, M. Almeida, et al. Venus cloud top winds from tracking uv features in venus monitoring camera images. *Journal of Geophysical Research: Planets*, 114(E5), 2009.

D. Mortimer. Telescope simulator. `https://github.com/dmortimer101/Telescope_Simulator`, 2023.

I. C. Müller-Wodarg, S. Bruinsma, J.-C. Marty, and H. Svedhem. In situ observations of waves in venus's polar lower thermosphere with venus express aerobraking. *Nature Physics*, 12(8):767–771, 2016.

T. Navarro, G. Schubert, and S. Lebonnois. Atmospheric mountain wave generation on Venus and its influence on the solid planet's rotation rate. *Nature Geoscience*, 11:487–491, 2018. doi: 10.1038/s41561-018-0157-x.

E. Neefs, A. C. Vandaele, R. De Cock, J. Erwin, S. Robert, I. R. Thomas, S. Berkenbosch, L. Jacobs, P. Bogaert, B. Beeckman, et al. Venspec-h spectrometer on the esa envision mission: Design, modeling, analysis. 2024.

M. Newman, G. Schubert, A. J. Kliore, and I. R. Patel. Zonal winds in the middle atmosphere of venus from pioneer venus radio occultation data. *Journal of the atmospheric sciences*, 41(12):1901–1913, 1984.

M. Newville, T. Stensitzki, D. B. Allen, M. Rawlik, A. Ingargiola, and A. Nelson. Lmfit: Non-linear least-square minimization and curve-fitting for python. *Astrophysics Source Code Library*, pages ascl–1606, 2016.

E. L. Nielsen, R. J. De Rosa, B. Macintosh, J. J. Wang, J.-B. Ruffio, E. Chiang, M. S. Marley, D. Saumon, D. Savransky, S. M. Ammons, et al. The gemini planet imager exoplanet survey: giant planet and brown dwarf demographics from 10 to 100 au. *The Astronomical Journal*, 158(1):13, 2019.

J. G. O'Rourke, A. S. Wolf, and B. L. Ehlmann. Venus: Interpreting the spatial distribution of volcanically modified craters. *Geophysical Research Letters*, 41(23):8252–8260, 2014.

K. F. Palmer and D. Williams. Optical constants of sulfuric acid; application to the clouds of venus? *Applied Optics*, 14(1):208–219, 1975.

J. Peralta, R. Hueso, and A. Sánchez-Lavega. Cloud brightness distribution and turbulence in venus using galileo violet images. *Icarus*, 188(2):305–314, 2007a.

J. Peralta, R. Hueso, and A. Sánchez-Lavega. A reanalysis of venus winds at two cloud levels from galileo ssi images. *Icarus*, 190(2):469–477, 2007b.

J. Peralta, R. Hueso, A. Sánchez-Lavega, G. Piccioni, O. Lanciano, and P. Drossart. Characterization of mesoscale gravity waves in the upper and lower clouds of venus from vex-virtis images. *Journal of Geophysical Research: Planets*, 113(E5), 2008.

J. Peralta, D. Luz, D. Berry, C. Tsang, A. Sánchez-Lavega, R. Hueso, G. Piccioni, and P. Drossart. Solar migrating atmospheric tides in the winds of the polar region of venus. *Icarus*, 220(2):958–970, 2012.

J. Peralta, R. Hueso, A. Sánchez-Lavega, Y. J. Lee, A. G. Muñoz, T. Kouyama, H. Sagawa, T. M. Sato, G. Piccioni, S. Tellmann, T. Imamura, and T. Satoh. Stationary waves and slowly moving features in the night upper clouds of Venus. *Nature Astronomy*, 1:0187, 2017. doi: 10.1038/s41550-017-0187.

J. Peralta, R. Hueso, A. Sánchez-Lavega, Y. J. Lee, A. G. Muñoz, T. Kouyama, H. Sagawa, T. M. Sato, G. Piccioni, S. Tellmann, T. Imamura, and T. Satoh. Stationary waves and slowly moving features in the night upper clouds of venus. *Nature Astronomy*, 1(8): 0187, jul 2017. doi: 10.1038/s41550-017-0187. URL https://doi.org/10.1038%2Fs41550-017-0187.

J. Peralta, T. Navarro, C. Vun, A. Sánchez-Lavega, K. McGouldrick, T. Horinouchi, T. Imamura, R. Hueso, J. Boyd, G. Schubert, et al. A long-lived sharp disruption on the lower clouds of venus. *Geophysical Research Letters*, 47(11):e2020GL087221, 2020.

M. Persson. Venus thermosphere densities as revealed by venus express torque and accelerometer data, 2015.

A. Petculescu and R. M. Lueptow. Atmospheric acoustics of titan, mars, venus, and earth. *Icarus*, 186(2):413–419, 2007.

E. V. Petrova, O. S. Shalygina, and W. J. Markiewicz. The vmc/vex photometry at small phase angles: Glory and the physical properties of particles in the upper cloud layer of venus. *Planetary and Space Science*, 113 - 114:120 – 134, 2015. ISSN 0032-0633. doi: http://dx.doi.org/10.1016/j.pss.2014.11.013. SI:Exploration of Venus.

A. Piccialli, D. V. Titov, A. Sanchez-Lavega, J. Peralta, O. Shalygina, W. J. Markiewicz, and H. Svedhem. High latitude gravity waves at the venus cloud tops as observed by the venus monitoring camera on board venus express. *Icarus*, 227:94–111, 2014.

J. B. Pollack, O. B. Toon, R. C. Whitten, R. Boese, B. Ragent, M. Tomasko, L. Esposito, L. Travis, and D. Wiedman. Distribution and source of the uv absorption in venus' atmosphere. *Journal of Geophysical Research: Space Physics*, 85(A13):8141–8150, 1980.

B. Quarles and J. J. Lissauer. Long-term Stability of Planets in the α Centauri System. AJ, 151(5):111, May 2016. doi: 10.3847/0004-6256/151/5/111.

B. Ragent, L. Esposito, M. Tomasko, M. Y. Marov, V. Shari, and V. Lebedev. Particulate matter in the venus atmosphere. *Advances in space research*, 5(11):85–115, 1985.

P. L. Read and S. Lebonnois. Superrotation on venus, on titan, and elsewhere. *Annual Review of Earth and Planetary Sciences*, 46:175–202, 2018.

G. R. Ricker, D. Latham, R. Vanderspek, K. Ennico, G. Bakos, T. Brown, A. Burgasser, D. Charbonneau, M. Clampin, L. Deming, et al. Transiting exoplanet survey satellite (tess). In *American Astronomical Society Meeting Abstracts# 215*, volume 215, pages 450–06, 2010.

M. Rodenhuis, H. Canovas, S. Jeffers, and C. Keller. The extreme polarimeter (expo): design of a sensitive imaging polarimeter. In *Ground-based and Airborne Instrumentation for Astronomy II*, volume 7014, page 70146T. International Society for Optics and Photonics, 2008.

M. Rodenhuis, H. Canovas, S. Jeffers, M. de Juan Ovelar, M. Min, L. Homs, and C. Keller. The extreme polarimeter: design, performance, first results and upgrades. In *Ground-based and Airborne Instrumentation for Astronomy IV*, volume 8446, pages 1413–1430. SPIE, 2012.

P. Rosenblatt, S. Bruinsma, I. Müller-Wodarg, B. Häusler, H. Svedhem, and J. Marty. First ever in situ observations of venus' polar upper atmosphere density using the tracking data of the venus express atmospheric drag experiment (vexade). *Icarus*, 217(2):831–838, 2012.

L. Rossi and D. M. Stam. Using polarimetry to retrieve the cloud coverage of Earth-like exoplanets. A&A, 607:A57, Nov. 2017. doi: 10.1051/0004-6361/201730586.

L. Rossi and D. M. Stam. Circular polarization signals of cloudy (exo)planets. A&A, 616: A117, Aug. 2018. doi: 10.1051/0004-6361/201832619.

L. Rossi, E. Marcq, F. Montmessin, A. Fedorova, D. Stam, J.-L. Bertaux, and O. Korablev. Preliminary study of venus cloud layers with polarimetric data from spicav/vex. *Planetary and Space Science*, 113:159–168, 2015.

L. Rossi, J. Berzosa-Molina, and D. M. Stam. Pymiedap: a python–fortran tool for computing fluxes and polarization signals of (exo) planets. *Astronomy & Astrophysics*, 616: A147, 2018.

L. Rossi, J. Berzosa-Molina, J.-M. Desert, L. Fossati, A. G. Muñoz, C. Haswell, P. Kabath, K. Kislyakova, D. Stam, and A. Vidotto. Spectropolarimetry as a tool for understanding the diversity of planetary atmospheres. *Experimental Astronomy*, pages 1–10, 2021.

Rossi, L. and Stam, D. M. Circular polarization signals of cloudy (exo)planets. *A&A*, 616: A117, 2018. doi: 10.1051/0004-6361/201832619. URL https://doi.org/10.1051/0004-6361/201832619.

W. B. Rossow, A. D. Del Genio, and T. Eichler. Cloud-tracked winds from pioneer venus ocpp images. *Journal of Atmospheric Sciences*, 47(17):2053–2084, 1990.

E. E. Russell, F. G. Brown, R. A. Chandos, W. C. Fincher, L. F. Kubel, A. A. Lacis, and L. D. Travis. Galileo Photopolarimeter/Radiometer experiment. Space Sci. Rev., 60(1-4): 531–563, May 1992. doi: 10.1007/BF00216867.

A. Sánchez-Lavega, S. Lebonnois, T. Imamura, P. Read, and D. Luz. The atmospheric dynamics of venus. *Space Science Reviews*, 212(3-4):1541–1616, 2017.

M. Sato, L. Travis, and K. Kawabata. Photopolarimetry Analysis of the Venus Atmosphere in Polar Regions. *Icarus*, 124:569–585, dec 1996. doi: 10.1006/icar.1996.0231.

M. Sato, L. D. Travis, and K. Kawabata. Photopolarimetry analysis of the venus atmosphere in polar regions. *Icarus*, 124(2):569–585, 1996.

T. Sato, T. Satoh, H. Sagawa, N. Manago, Y. J. Lee, S.-y. Murakami, K. Ogohara, G. Hashimoto, Y. Kasaba, A. Yamazaki, et al. Dayside cloud top structure of venus retrieved from akatsuki ir2 observations. *Icarus*, page 113682, 2020.

T. Satoh, S. Ohtsuki, N. Iwagami, M. Ueno, K. Uemizu, M. Suzuki, G. L. Hashimoto, T. Sakanoi, Y. Kasaba, R. Nakamura, et al. Venus' clouds as inferred from the phase curves acquired by ir1 and ir2 on board akatsuki. *Icarus*, 248:213–220, 2015.

T. Satoh, T. M. Sato, M. Nakamura, Y. Kasaba, M. Ueno, M. Suzuki, G. L. Hashimoto, T. Horinouchi, T. Imamura, A. Yamazaki, T. Enomoto, Y. Sakurai, K. Takami, K. Sawai, T. Nakakushi, T. Abe, N. Ishii, C. Hirose, N. Hirata, M. Yamada, S.-y. Murakami, Y. Yamamoto, T. Fukuhara, K. Ogohara, H. Ando, K.-i. Sugiyama, H. Kashimura, and S. Ohtsuki. Performance of Akatsuki/IR2 in Venus orbit: the first year. *Earth, Planets, and Space*, 69:154, 2017. doi: 10.1186/s40623-017-0736-x.

G. Schubert, C. Covey, A. D. Genio, L. Elson, G. Keating, A. Seiff, R. Young, J. Apt, C. Counselman III, A. Kliore, et al. Structure and circulation of the venus atmosphere. *Journal of Geophysical Research: Space Physics*, 85(A13):8007–8025, 1980.

G. Schubert, S. Bougher, C. Covey, A. Del Genio, A. Grossman, J. Hollingsworth, S. Limaye, and R. Young. Venus atmosphere dynamics: A continuing enigma. *Washington DC American Geophysical Union Geophysical Monograph Series*, 176:101–120, 2007.

S. Seager, B. A. Whitney, and D. D. Sasselov. Photometric Light Curves and Polarization of Close-in Extrasolar Giant Planets. ApJ, 540(1):504–520, Sept. 2000. doi: 10.1086/309292.

A. Seiff, D. B. Kirk, R. E. Young, R. C. Blanchard, J. T. Findlay, G. Kelly, and S. Sommer. Measurements of thermal structure and thermal contrasts in the atmosphere of venus and related dynamical observations: Results from the four pioneer venus probes. *Journal of Geophysical Research: Space Physics*, 85(A13):7903–7933, 1980.

A. Seiff, J. Schofield, A. Kliore, F. Taylor, S. Limaye, H. Revercomb, L. Sromovsky, V. Kerzhanovich, V. Moroz, and M. Y. Marov. Models of the structure of the atmosphere of venus from the surface to 100 kilometers altitude. *Advances in Space Research*, 5 (11):3–58, 1985.

W. C. Skamarock and J. B. Klemp. A time-split nonhydrostatic atmospheric model for weather research and forecasting applications. *Journal of Computational Physics*, 227: 3465–3485, 2008.

S. Smrekar, S. Hensley, R. Nybakken, M. S. Wallace, D. Perkovic-Martin, T.-H. You, D. Nunes, J. Brophy, T. Ely, E. Burt, et al. Veritas (venus emissivity, radio science, insar, topography, and spectroscopy): a discovery mission. In *2022 IEEE aerospace conference (AERO)*, pages 1–20. IEEE, 2022.

M. Sneep and W. Ubachs. Direct measurement of the Rayleigh scattering cross section in various gases. *J. Quant. Spectrosc. Radiative Transfer*, 92:293–310, May 2005. doi: 10.1016/j.jqsrt.2004.07.025.

M. Sneep and W. Ubachs. Direct measurement of the rayleigh scattering cross section in various gases. *Journal of quantitative spectroscopy and radiative transfer*, 92(3):293–310, 2005.

F. Snik, O. Kochukhov, N. Piskunov, M. Rodenhuis, S. Jeffers, C. Keller, A. Dolgopolov, E. Stempels, V. Makaganiuk, J. Valenti, and C. Johns-Krull. The harps polarimeter, 2010. URL `https://arxiv.org/pdf/1010.0397.pdf`.

D. Stam. Spectropolarimetric signatures of earth-like extrasolar planets. *Astronomy & Astrophysics*, 482(3):989–1007, 2008.

D. Stam and J. Hovenier. Errors in calculated planetary phase functions and albedos due to neglecting polarization. *Astronomy & Astrophysics*, 444(1):275–286, 2005.

D. Stam, J. De Haan, J. Hovenier, and P. Stammes. Degree of linear polarization of light emerging from the cloudless atmosphere in the oxygen a band. *Journal of Geophysical Research: Atmospheres*, 104(D14):16843–16858, 1999.

D. Stam, J. De Haan, J. Hovenier, and P. Stammes. A fast method for simulating observations of polarized light emerging from the atmosphere applied to the oxygen-a band. *Journal of Quantitative Spectroscopy and Radiative Transfer*, 64(2):131–149, 2000.

D. Stam, J. Hovenier, and L. Waters. Using polarimetry to detect and characterize jupiter-like extrasolar planets. *Astronomy & Astrophysics*, 428(2):663–672, 2004.

R. G. Strom, G. G. Schaber, and D. D. Dawson. The global resurfacing of venus. *Journal of Geophysical Research: Planets*, 99(E5):10899–10926, 1994.

H. Svedhem, D. Titov, D. McCoy, J.-P. Lebreton, S. Barabash, J.-L. Bertaux, P. Drossart, V. Formisano, B. Häusler, O. Korablev, et al. Venus express—the first european mission to venus. *Planetary and Space Science*, 55(12):1636–1652, 2007.

H. Svedhem, D. Titov, F. Taylor, and O. Witasse. Venus express mission. *Journal of Geophysical Research: Planets*, 114(E5), 2009.

L. Team et al. The luvoir mission concept study final report. *arXiv preprint arXiv:1912.06219*, 2019.

S. Tellmann, B. Häusler, D. Hinson, G. Tyler, T. Andert, M. Bird, T. Imamura, M. Pätzold, and S. Remus. Small-scale temperature fluctuations seen by the vera radio science experiment on venus express. *Icarus*, 221(2):471–480, 2012.

D. Titov, H. Svedhem, D. Koschny, R. Hoofs, S. Barabash, J.-L. Bertaux, P. Drossart, V. Formisano, B. Häusler, O. Korablev, et al. Venus express science planning. *Planetary and Space Science*, 54(13-14):1279–1297, 2006.

D. V. Titov, N. I. Ignatiev, K. McGouldrick, V. Wilquet, and C. F. Wilson. Clouds and hazes of venus. *Space Science Reviews*, 214:1–61, 2018.

L. Travis, D. Coffeen, J. Hansen, K. Kawabata, A. Lacis, W. Lane, S. Limaye, and P. Stone. Orbiter cloud photopolarimeter investigation. *Science*, 203(4382):781–785, 1979.

L. D. Travis. Imaging and polarimetry with the Pioneer Venus Orbiter Cloud Photopolarimeter. In C. L. Wyman, editor, *Space optics*, volume 183 of *Proceedings SPIE*, pages 299–304, Jan. 1979. doi: 10.1117/12.957426.

L. D. Travis. Imaging and polarimetry with the pioneer venus orbiter cloud photopolarimeter, 1979. URL https://doi.org/10.1117/12.957426.

V. J. Trees and D. M. Stam. Ocean signatures in the total flux and polarization spectra of earth-like exoplanets. *Astronomy & Astrophysics*, 664:A172, 2022.

V. J. H. Trees and D. M. Stam. Ocean signatures in the total flux and polarization spectra of Earth-like exoplanets. A&A, 664:A172, Aug. 2022. doi: 10.1051/0004-6361/202243591.

C. Tsang, P. Irwin, F. Taylor, and C. Wilson. A correlated-k model of radiative transfer in the near-infrared windows of venus. *Journal of Quantitative Spectroscopy and Radiative Transfer*, 109(6):1118–1135, 2008.

G. Tselioudis. ISCCP Definition of Cloud Types, 2001. URL https://isccp.giss.nasa.gov/cloudtypes.html.

M. Turbet, E. Bolmont, G. Chaverot, D. Ehrenreich, J. Leconte, and E. Marcq. Day–night cloud asymmetry prevents early oceans on venus but not on earth. *Nature*, 598(7880): 276–280, 2021.

R. van Holstein. *High-contrast imaging polarimetry of exoplanets and circumstellar disks*. PhD thesis, Leiden University, 2021.

A. C. Vandaele, O. Korablev, D. Belyaev, S. Chamberlain, D. Evdokimova, T. Encrenaz, L. Esposito, K. L. Jessup, F. Lefèvre, S. Limaye, et al. Sulfur dioxide in the venus atmosphere: Ii. spatial and temporal variability. *Icarus*, 295:1–15, 2017.

S. R. Vaughan, T. D. Gebhard, K. Bott, S. L. Casewell, N. B. Cowan, D. S. Doelman, M. Kenworthy, J. Mazoyer, M. A. Millar-Blanchaer, V. J. Trees, et al. Chasing rainbows and ocean glints: Inner working angle constraints for the habitable worlds observatory. *Monthly Notices of the Royal Astronomical Society*, 524(4):5477–5485, 2023.

J. Veverka. A polarimetric search for a venus halo during the 1969 inferior conjunction. *Icarus*, 14(2):282–283, 1971.

M. J. Way and A. D. Del Genio. Venusian habitable climate scenarios: Modeling venus through time and applications to slowly rotating venus-like exoplanets. *Journal of Geophysical Research: Planets*, 125(5):e2019JE006276, 2020.

V. Wilquet, A. Fedorova, F. Montmessin, R. Drummond, A. Mahieux, A. C. Vandaele, E. Villard, O. Korablev, and J.-L. Bertaux. Preliminary characterization of the upper haze by spicav/soir solar occultation in uv to mid-ir onboard venus express. *Journal of Geophysical Research: Planets*, 114(E9), 2009.

C. F. Wilson, T. Widemann, and R. Ghail. Venus: Key to understanding the evolution of terrestrial planets. *Experimental Astronomy*, 54(2-3):575–595, 2022.

Y. L. Yung and W. DeMore. Photochemistry of the stratosphere of venus: Implications for atmospheric evolution. *Icarus*, 51(2):199–247, 1982.

S. Zhang, S. Bougher, and M. Alexander. The impact of gravity waves on the venus thermosphere and o2 ir nightglow. *Journal of Geophysical Research: Planets*, 101(E10): 23195–23205, 1996.

CURRICULUM VITÆ

Gourav MAHAPATRA

22-8-1990	Born in Rourkela, India.
1993–2008	Delhi Public School, Rourkela, India
2009–2013	Bachelors of Technology in Aeronautical Engineering Manipal Institute of Technology, Manipal, India
2014–2016	Masters of Science in Aerospace Engineering Technische Universiteit Delft, The Netherlands
2016–2025	PhD. Candidate - Planetary Exploration (PE) Technische Universiteit Delft, The Netherlands
2020–2023	Scientist - Earth Group SRON Netherlands Institute for Space Research, The Netherlands
2023–2024	Data Scientist satsearch, The Netherlands
2024–present	Senior Data Specialist leads.io, The Netherlands

List of Publications

- **Mahapatra, G.**, Abiad, F., Rossi, L., & Stam, D. M. (2023). From exo-Earths to exo-Venuses: Flux and polarization signatures of reflected light. *Astronomy & Astrophysics*, 671, A165.
- Schuit, B.J., Maasakkers, J.D., Bijl, P., **Mahapatra, G.**, Van den Berg, A.W., Pandey, S., Lorente, A., Borsdorff, T., Houweling, S., Varon, D.J. & McKeever, J. (2023). Automated detection and monitoring of methane super-emitters using satellite data. *Atmospheric Chemistry and Physics Discussions*, 2023, 1-47.
- Maasakkers, J.D., Varon, D.J., Elfarsdóttir, A., McKeever, J., Jervis, D., **Mahapatra, G.**, Pandey, S., Lorente, A., Borsdorff, T., Foorthuis, L.R. & Schuit, B.J. (2022). Using satellites to uncover large methane emissions from landfills. *Science Advances*, 8(31), eabn9683.
- Jaiswal, B., **Mahapatra, G.**, Nandi, A., Sudhakar, M., Sankarasubramanian, K., & Sheel, V. (2021). Polarization signatures of Mars dust and clouds: Prospects for future spacecraft observations. *Planetary and Space Science*, 201, 105193.
- **Mahapatra, G.**, Lefèvre, M., Rossi, L., Spiga, A., & Stam, D. M. (2021). Polarimetry as a tool for observing orographic gravity waves on venus. *The Planetary Science Journal*, 2(3), 96.
- **Mahapatra, G.**, Helling, C., & Miguel, Y. (2017). Cloud formation in metal-rich atmospheres of hot super-Earths like 55 Cnc e and CoRoT7b. *Monthly Notices of the Royal Astronomical Society*, 472(1), 447-464.